Ph.D Thesis Defense

Analysis of the Kinetics of Filler Segregation in Granular Block copolymer Microstructure

Bongjoon Lee

Department of Materials Science and Engineering
Carnegie Mellon University

12:30 PM, Wednesday, October 26th, 2016
WEAN HALL 2327 (Mehl Room)

Advisor
Professor Michael R. Bockstaller, MSE, CMU

Committee Members
Professor Lynn M. Walker, ChemE, CMU
Professor Marc De Graef, MSE, CMU
Professor Elizabeth A. Holm, MSE, CMU

Acknowledgement

I want to thank Prof. Bockstaller for all of my achievements. With his guidance, I have had great time exploring the fundamental aspect of material science research. I feel very lucky that I have met a great advisor that I fully respect in both academically and also his character as a true educator. I thank him for the great opportunities he has suggested me including numerous collaborative researches.

I appreciate my thesis committee, Prof. Walker, Prof. Holm and Prof. Degraef for giving me great comments and suggestions on my research. Discussion with them has given me a chance to look at my research in different perspective. Their comments have made me not overlook any details and it led me closer to the final results. I also need to show my appreciation to the financial support from National Science Foundation (DMR-1410845).

I would like to thank Markus Bleuel (NCNR) who has introduced me to the neutron scattering world. Visiting NCNR for neutron scattering was one of the best moments in grad school. Scientific discussions and conversations with NCNR people were also very memorable and I felt very happy that I chose science as my major. I also thank Dr. Hakem who helped me get accurate calculation on neutron scattering data. And she always cheered me up while I was going through the proposal and defense, I hope her all the best as well.

I want to thank Tom Nuhfer, Jason Wolf, Adam Wise, William Pingitore, Betsy Clark, David Crockett and Brett Riale for giving me good technical support such as TEM, SAXS and DSC. They have spent lots of time to train me with the equipment and supported that I could use the equipment in best condition. Also I want to acknowledge

Kelly Rockenstein, Suzanne Smith, Jeanna Pekarcik, Roxann Eckman, Neetha Kahn, Angela Pusateri, Anthony Talotta and Marygrace Antkowski for your support including all document works, reserving facilities, ordering chemicals and being very nice to all of my inquiries.

I want to thank the current and former member of the Bockstaller research group: Hyungju Ryu, Sudarshan Narayanan, Michael Schmitt, Clare Mahoney, Rachel Ferebee, Lauren Finkenauer, Alei Dang, Zongyu Wang, Zhao Lu (Congrats on your upcoming wedding!), Jianan Zhang, Xin Ning, Guangyuan Yang, Lu Dai, Beibei Chen, Jeeyoung Lee, Soohyun Park, Shuo Li, Yi Shi, Danli Luo, Qingyun Lu, Tong mo. Because of them I enjoyed the time in the lab very much. It was such a good vibe and I will miss the time we hung out together including eating at Alibaba, camping in the park and trip to the Cedar Point, Chicago. I also thank my undergraduate students, David Ott and Adrian Zhao, for helping extensively with the cryomicrotoming and TEM image stitching. Cryomicrotoming is very labor intensive and they have always done great job. I was lucky to work with them and hope they have gained a lot of experience.

I had great time with my office mates in WEAN 2313, Aditya Balasubramanian (AB), Rachel Ferebee, Proud Pitirat, Lauren Finkenauer, Zhao Lu. I will miss the time when we were talking about our every day lives, playing sports together, sharing snacks and also going to Razzy fresh. Thanks for being such a great officemates!

I also thank all the CMU MSE friends. We all supported each other through the ups and downs of the graduate school life. I have had such a good memories with them like MSE happy hours, MSE softball team, Pedal Pittsburgh, Halloween party, hiking trip and etc. I hope I can visit CMU MSE events to see them soon!

I thank the Korean community here in CMU and with them I could overcome any homesick that happens from time to time. I had lots of fun playing sports and cook Korean food together. And I still look at the pictures we took during our great adventures such as trip to Machu Pichu, San Diego very often. Also I want to thank everyone in Korean Catholic church. Thanks for providing great atmosphere where we can recharge from many difficulties. And I thank all of my friends in Korea who always welcome me whenever I go back to Korea and I can't wait to celebrate this achievement with them.

And specially, I want to thank my girl friend, Shari Cheng, for her love, care and support in every way. I won't forget all the weekend adventures and precious memories that we have made together. I couldn't do this without you and I am very happy that you are by my side. I also thank CMU group x class for giving me chance to meet this wonderful lady.

I thank all of my relatives for their support in me but at the same time I feel sorry that I have missed lots of family events while I was studying in CMU. Both of my grandmothers have passed away while I was here. I wish I could tell them this great news but I am sure they are pride of me in a good place. I miss them so much.

Lastly and most importantly, I want to thank my family, my dad, mom and brother, who I love so much, back in Korea. I dedicate this thesis to my parents. Thanks for always being on my side and praying for me. Your presence gives me strength more than anything. I miss them so much and I can't wait to see them soon.

Abstract

Block copolymers have attracted interests for potential application ranging from dynamic photonic sensors to solid-state ion conductors. However, due to nucleation and growth mechanism, block copolymer inherently forms granular microstructure with defects such as grain boundaries. Understanding the microstructure of block copolymer is thus crucial in many applications because the microstructure determines the transport property of functional fillers such as ions in block copolymer template. Previous research has shown that *athermal* filler segregated to grain boundary of lamellae block copolymer and retards the grain coarsening. However, the kinetics of this grain boundary segregation during thermal annealing has not been revealed. Polystyrene-b-polyisoprene blended with deuterated polystyrene is used for neutron scattering study on studying the kinetics of grain boundary segregation. Deuterated polystyrene will segregate to grain boundaries, therefore, decorate grain boundary. The filler segregation behavior will be studied by comparing neutron scattering of polystyrene-b-polyisoprene/deuterated polystyrene with different annealing times (at T=130 deg C, duration of 0hr, 3hr, 1day, 3day and 7day, respectively). Invariant (Q) analysis along with grain mapping is conducted to quantitatively analyze the kinetics of grain boundary segregation. This kinetic was in good agreement with the McLean's kinetic model for grain boundary segregation in metals. By applying Langmuir-Mclean's segregation isotherm equation, we have predicted the equilibrium concentration of filler in grain boundary by calculating the strain energy stored in grain boundary.

Table of Contents

LIST OF FIGURES

LIST OF TABLES

GLOSSARY OF TERMS

α_2 : Enrichment ratio, $C(gb,\infty)/C(1)$

b : scattering length

λ: wavelength of neutron

f: Volume fraction

$C(gb,t)$: Grain boundary concentration after time t

$C(gb,0)$: Initial grain boundary concentration.

$C(gb,\infty)$: Equilibrium grain boundary concentration attained after infinite time

$C(1)$: Grain interior concentration, assumed constant

D : diffusion coefficient

$A = \frac{4D}{\alpha_2 d}$ is the fitting parameter for McLean's kinetic equation

θ: misorientation of symmetric tilt grain boundary

θ_s: scattering angle of X-ray or neutron

h_{cv} : graft chain length on convex side of the interface

h_{cc} : graft chain length on concave side of the interface

$\mathbf{k_i}$: wave vector of incident neutron or X-ray

$\mathbf{k_f}$: wave vector of scattered neutron or X-ray

δ: path different between two rays scattered at different particles

ϕ: phase difference between two rays scattered at different particles

$d\sigma/_{d\Omega}$: differential cross-section of material in neutron scattering

$\Sigma_s(\mathbf{q})$: differential scattering cross-section per volume

$S(\mathbf{q})$: Structure factor

I_m: scattering intensity from individual particle

N_m: number of particles in the system

A_{sd}: Sample to detector distance in neutron scattering

$\langle c_m \rangle$: mean density of the particles

$\rho\ (= SLD)$: scattering length density

SLD_{GB}: scattering length density of grain boundary

SLD_m: scattering length density of grain (=matrix)

$\Delta(SLD)$: scattering length density contrast between grain boundary and grain

ρ_0: average scattering length density per particle

v: particle volume

R_g: radius of gyration

Q: invariant

η: deviation of scattering length density ρ from its mean

S_p: total area of the boundary of the two phases determined from Porod law

$M(r)$: mass within a sphere with diameter r

$\tilde{\rho}(r)$: density

d_s: surface fractal dimension

d_m: mass fractal dimension

$A_n(q)$: Amplitude of scattered neutron

$\Gamma_1(x)$: 1-dimensional correlation function of scattering length density

$I_1(q)$: Lorentz corrected scattering intensity

T_{Rock} : Transmission measured by measuring peak intensity

T_{Wide} : Transmission measured at wide angle

T_{sam} : Transmission of the sample

T_{emp}: Transmission of the empty cell

I_{COR}: corrected scattered neutron intensity

I_{SAM} : sample scattering intensity

I_{EMP} : empty scattering intensity

I_{BGD}: background scattering intensity

d_{sam}: sample thickness

ΔΩ: solid angle accepted by analyzer in neutron scattering

$\tilde{I}(q)$: scattered intensity measured along vertical axis after slit smearing

$W(u)$: normalized intensity distribution along the slit horizontal direction

$u = (2\pi/\lambda)(x_1/Z)$: scattering vector corresponding to the position x_1

$\phi_f =$ flux on the sample

$A_s =$ Sample Area

$\varepsilon =$ detector efficiency

t_s= effective counting time, which was renormalized to give 10_8 monitor counts (MON)

$I_s(0) =$ measured intensity of the standard sample at $Q = 0$

$Debye(l)$=Debye function

$l = (qR_g)^2$

b_k : Kuhn length

I_t : thermal concentration fluctuation scattering

w is the weight fraction of component in blend for Fox-equation

T_g is the glass transition temperature

q^* : Primary lamellar peak in SANS

A: grain area

σ: scale parameter in lognormal probability density function

μ: shape scale parameter in lognormal probability density function

$\nu_{p,GB}$: gold nanoparticle aggregate density within HAGB

W : grain boundary width

L : lamellar spacing

R: radius of curvature within grain boundary

S_V: grain boundary surface area per volume

L_V: length of linear elements per area

P_L : grain boundary number of point intersection per unit length of line

$V_V (=\phi)$: volume fraction of grain boundary

γ_{rel} : relative grain boundary energy

γ_1 : autocorrelation function of the scattering length density

f: total volume fraction of d-PS in blend

x : relative volume fraction of d-PS segregated to grain boundary

$C(GB, t)$: volume fraction of filler in grain boundary

$C_{PS-PI}(GB, t)$: volume fraction of PS-PI in grain boundary

$C(Grain, t)$: volume fraction of filler in grain

$C_{PS-PI}(Grain, t)$: volume fraction of PS-PI in grain

A_M: fitting parameter in McLean's kinetics model

α_2 is the ratio $C(gb, \infty)/C(1)$

$C(1)$ is the grain interior concentration, assumed constant

p : number of solutes distributed among grain boundary sites

P : number of solutes

j : number of lattice sites in grain boundary

J : number of lattice sites in grain

X_b^0 : fraction of the grain boundary monolayer available filler at saturation

X_b : actual fraction covered with segregant

X_c : bulk solute molar fraction

G: total free energy of the system

T : temperature

R : gas constant

$\Sigma(z)$: area of two dimensional slice at a height z above the interface of PS-PI

H : mean curvature of the interface

K : Gaussian curvature of the interface

c_1,c_2 : principal curvatures of the interface

h^*: graft chain length at flat interface

Σ^* : interfacial area per chain at flat interface

N_A : Avogadro's number

R_f : length of the chain after deformation

t: thermal annealing time (hrs)

q: scattering vector

W: Width of the grain boundary

1. Introduction

1.1 Block copolymer and defect

Block copolymers are composed of more than two different polymeric species covalently bonded together. In the majority of cases, if two different polymeric species are mixed, they tend to phase separate. However, the chemical links between the polymeric species in block copolymer inhibit such macrophase separates. They still segregate to their separate domains but the domains have only mesoscopic dimensions that correspond to the size of the single block. [1] Various review papers on block copolymer system can be found.[2–4] We will focus on linear amorphous diblock copolymer system in this study.

Figure 1- 1 Illustration of linear diblock and triblock copolymer. Different color means chemically different polymeric species. Black dots symbolize covalent bonds.

Block copolymers form periodically ordered micro-domains resulting from the microphase separation.[5] As shown in **Figure 1- 2**, block copolymers form various structures including lamellae, sphere, cylinders and gyroid structures which have the potential to be used in modern technologies such as solar cell, solid state electrolyte and dynamic photonic sensors[4,6–18]. Compared to conventional techniques where fabrication of nanoscopic features less than 30nm is difficult due to the wavelength of light, block copolymer have attracted interest as viable alternatives for nanofabrication. By tuning

molecular structure, temperature, volume fraction of each block, external field and polydispersity, the shape of the microstructure (lamellae, cylinder, sphere, gyroid) and its size can be controlled.[19,20] However, block copolymers have structural defects such as grain boundaries that limit their application in emerging technologies. For example, an ionic current of solid-state ion conductor, one of the key interest areas for BCP, with block copolymer template will be disrupted by grain boundary because it will block ion pathway.

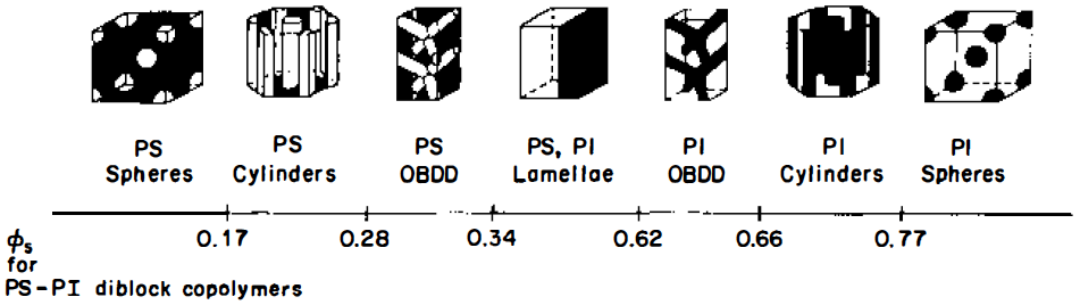

Figure 1- 2 Strong segregation limit (SSL) equilibrium morphologies for $(A\text{-}B)_n$ type block copolymers. $\boldsymbol{\phi_s}$ corresponds to the volume fraction of PS domain of PS-PI block copolymer [5]

The formation of granular microstructure is fundamentally due to nucleation and growth process of block copolymer during disorder-order transition, it inherently forms grain boundaries between adjacent grains. The ordering kinetics and morphology evolution of block copolymer has been studied over the past decades and one of the main focuses was on the grain nucleation and shape. Lodge et al. used Polarized optical microscopy (POM) and Avrami analysis to characterize grain shape, individual grain growth front velocity, bulk kinetics and determine nucleation and growth mechanism.[21,22] Balsara et al. used depolarized light scattering (DPLS) technique to identify two stages of grain growth (1) at the expense of disordered state (2) occurs by

defect annihilation.[23] Cohen et al. have used Ultra small angle X-ray scattering (USAXS) to simultaneous determine lamellar morphological length scale and the grain size of styrene-butadiene copolymer during thermal annealing.[24]

The grain boundary structure of lamellar block copolymer was first established by Hashimoto and Thomas.[25–30] The different types of grain boundaries (symmetric tilt, asymmetric tilt and twist grain boundary) under thermal annealing were observed by TEM. The grain boundary morphology was determined by the IMDS that form between micro-phases in the region of impingement. In tilt grain boundaries, grain orientations are tilted with respect to the axis which is parallel to the interfacial surface. Misorientation of tilt grain boundary, θ, is the angle between two lamellar normal direction. In twist boundaries, grain orientations are twisted around the axis which is normal to the interfacial surface. Figure 1- 3 compares the possible grain boundary structure of polycrystal and block copolymer. For polycrystal, it has been know that the grain structure governs the overall properties of the materials more than on the chemistry of a material. And also, the properties of GBs are important factor determining the grain growth and recrystallization. [31,32]

There have been theoretical studies regarding the grain boundary shape. Grain boundary regions have high energy because of packing frustration and entropy loss caused by extension of polymer chains. Frederickson et al. used numerical simulations to study on nucleation and growth of spherical grains of a lamellar block copolymer phase.[33] These studies revealed small nucleation barrier energy and critically slowed growth kinetics.

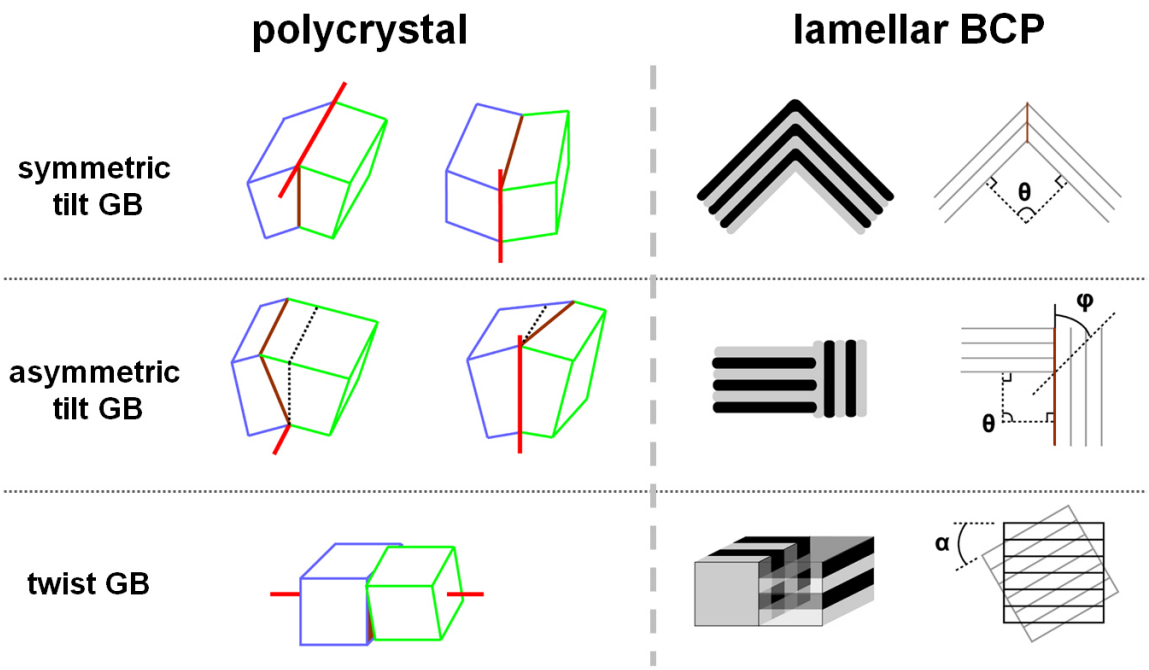

Figure 1- 3 Illustration of possible grain boundary structures of (a) polycrystals and (b) lamellar BCPs [25]

Schick and co-workers as well as Matsen et al. were the first to evaluate the surface energy of the three major grain boundary types in lamellar morphologies using self-consistent field theory and Ginzburg-Landau theory.[34,35]

Matsen used SCFT to reproduce the experimental results of grain boundary changing morphology from Chevron to Omega as tilt angle increases.[36] Figure 1- 4 shows the dependence of grain boundary energy on tilt angle. The transformation in domain shape was explained in terms of (1) A/B interfacial bending energy (2) A/B interfacial tension and (3) packing frustration. [37]

Schick et al have also reproduced the Chevron, Omega, and T-junction GBs in a symmetric di-BCPs using a Ginzburg-Landau free energy functional. Schick obtained the relation between the grain boundary energy and the tilt angle, $\gamma_{GB} \sim \theta^3$, however, this is

limited only to weak segregation limit because of the nature of a Ginzburg-Landau functional.[38–40]

Bockstaller and coworkers were the first to experimentally measure grain boundary energies in block copolymer materials by analyzing dihedral angles at triple junction points using Herring's equation and it was found that grain boundary energy increases as the tilt angle increases.[41,42] The experimentally determined dependence of energy on tilt angle was in qualitative agreement with theoretical studies done by Matsen. This result also revealed that the distribution of grain boundary misorientation broadly follows a Maxwell Boltzmann type dependence on grain boundary energy.

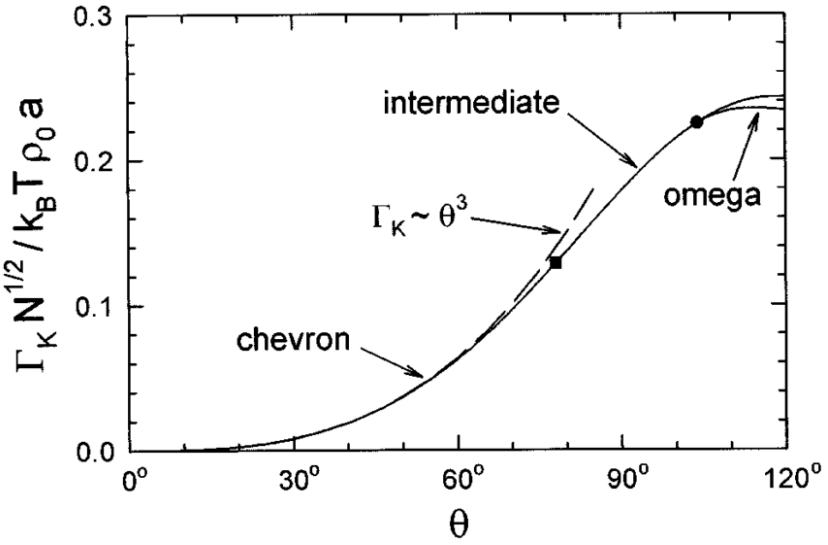

Figure 1- 4 Grain boundary energy change with respect to misorientation angle for $\chi N=20$, f=0.5. The transition from chevron to omega is denoted as a black dot. [35]

1.2 Block copolymer/homo-polymer blends

Studying the effect of homo-polymer addition on the morphology of block copolymer is technologically important because homo-polymer is a most relevant impurity in block copolymer. In a typical procedure of synthesizing block copolymer, the first block (PS) is

polymerized and then there is a transition step to polymerize the second block (PI). However, some of the PS are left unreacted and remains as a free homo-polymer.

The morphology of block copolymer/homo-polymer blended system is more complex than the pure block copolymer system because there is an interplay of two kinds of phase transitions: (i) Microphase separation resulted from the segregation between block A (polystyrene) and block B (polyisoprene) and (ii) Macrophase separation resulted from phase separation between block copolymer (PS-PI) and homopolymer (PS). [43]

Hashimoto et al have studied the effect molecular weight of homopolymer on the ordered structure of block copolymer/homopolymer mixture using Small Angle X-ray Scattering (SAXS). In this research, the author observed different spatial segmental distributions of the block copolymer (PS-PI) and homopolystyrene in a microdomain space for different molecular weights of homopolystyrene. As the molecular weight of the homo-polystyrene increases, the solubility of the homo-polystyrene in block-polystyrene decreases, therefore, localized solubilization of homo-polystyrene in the center of the PS micro-domain takes place. However, as the molecular weight of the homo-polystyrene decreases, homo-polystyrene solubilize in PS micro-domain uniformly. This transition was rationalized as a consequence of the configurational entropy loss associated with the penetration of high molecular chains into the copolymer brush.

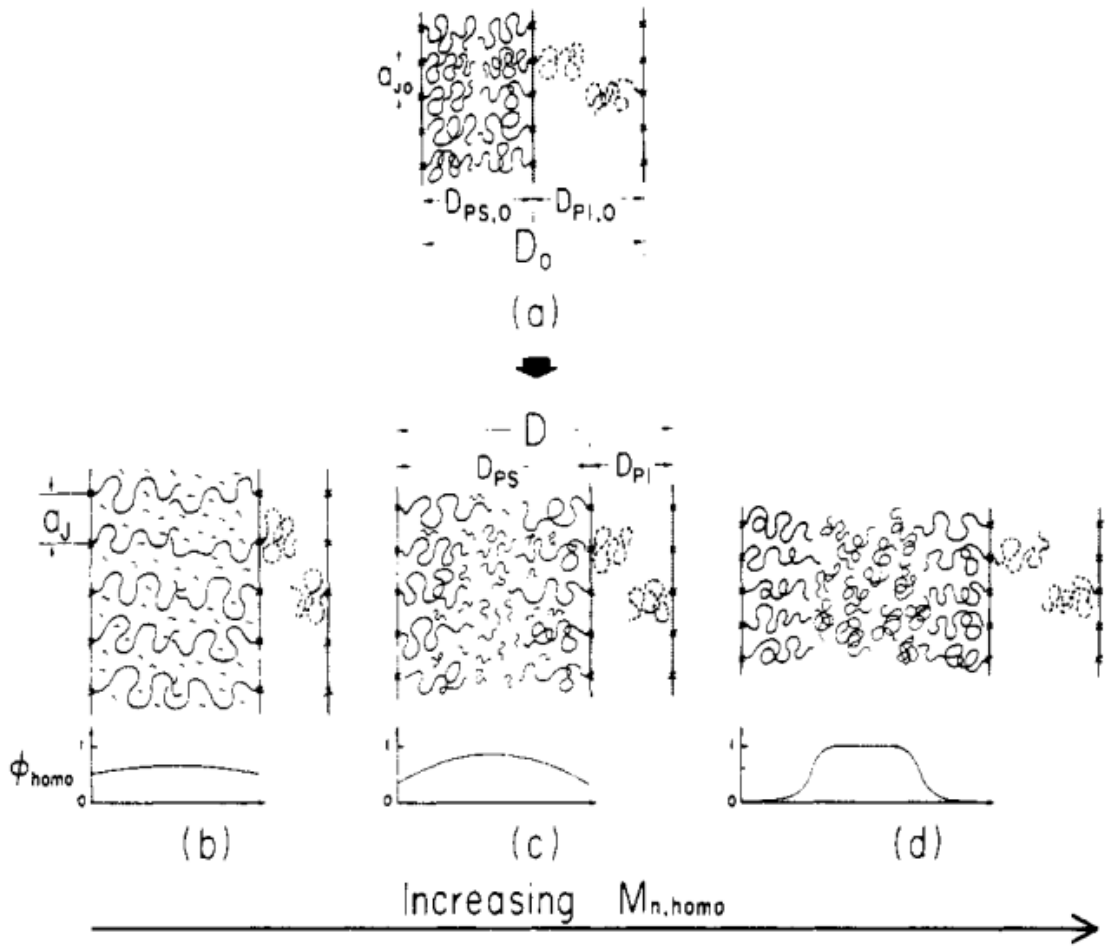

Figure 1- 5 Schematic representation of the spatial segmental distributions of the block copolymer and homopolystyrene chains in a microdomain space for different states of solubilization and corresponding spatial segmental density profile of HS across the PS microdomain space: (a) pure block copolymer; (b) uniform solubilization of homopolystyrene (HS) in the PS microdomain; (c) intermediate state between b and d; (d) localized solubilization of HS in the center of the PS microdomain [43]

This non-uniform hPS (homopolymer polystyrene) concentration profile in the PS layer was confirmed by Winey et al in their extensive investigation concerning the incorporation of homopolymers into diblock copolymers. [44]

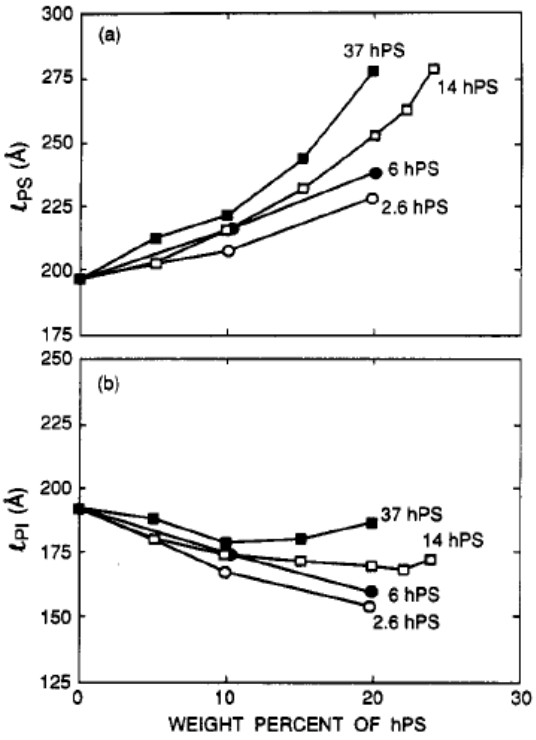

Figure 1- 6 Polystyrene layer thickness (a) and polyisoprene layer thickness (b) versus homopolymer concentration in blends of SI 27/22 and various molecular weight homopolystyrenes [44]

The distinct distribution states of homopolymer fillers were shown to give rise to different dependences of the lamellar spacing on the amount of added homopolymers. Specifically lamellar spacing of blends both larger and smaller than the pure block copolymer was observed. The overall thickness is combination of the axial expansion of PS layer and axial contraction of PI layer. The homo-polystyrene swells the PS block both axially and laterally, and as the PS block expands laterally the PI block also has to expand laterally due to the connectivity between PS and PI block. And in order to maintain the constant density within a block, the thickness of PI decreases. The symmetry of swelling in PS domain is defined by the ratio of the axial and lateral expansion of PS domain. The symmetry of the PS swelling becomes drastically asymmetric with the

increase in the molecular weight and/or concentration of hPS. This asymmetry of swelling agrees with the proposed spatial segmental distribution of block copolymer and homo-polymer.

Winey et al have also applied quantitative mean-field treatments to obtain homopolymer distributions in lamellar copolymer/homopolymer blends. Numerical solutions to the mean field equations are provided for experimentally studied block copolymer/homopolymer blends. The simulation also shows that the distribution of homopolymer in a block copolymer microdomain is non-uniform, with the maximum in the center of the compatible block domain. And the tendency of localization is dependent on the molecular weight and concentration of the homo-polymer. [45]

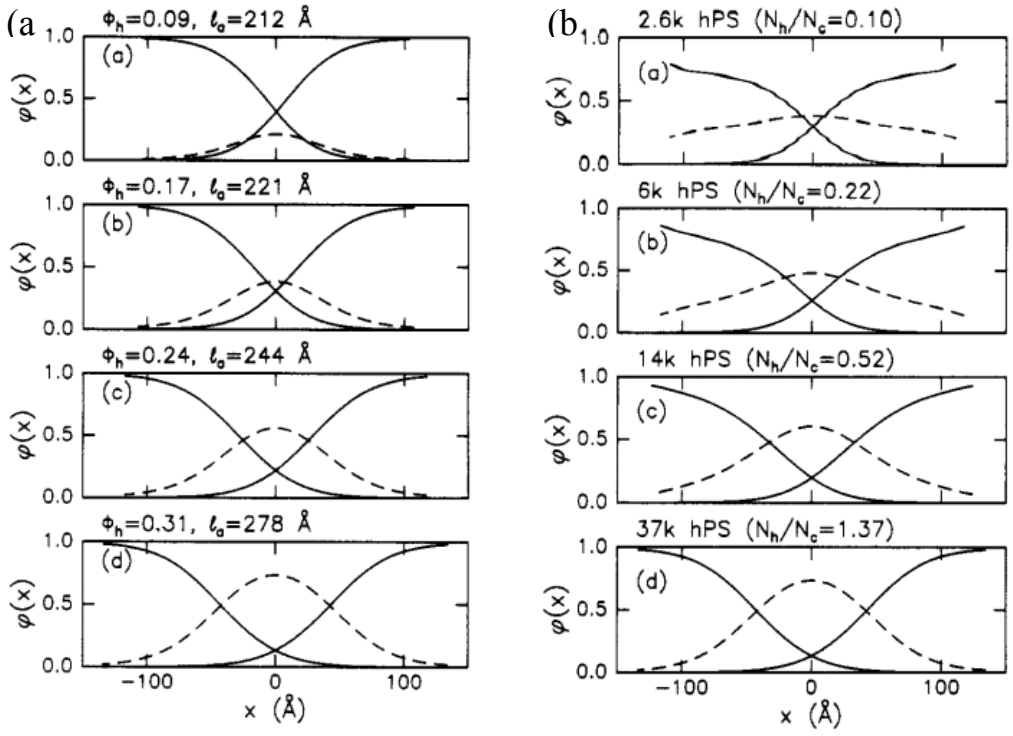

Figure 1- 7 (a) Calculated copolymer (solid) and homo-polymer (dash) profiles (a) for four blends with N_h/N_c=1.37 and varying Φ_h (b) for four blends with Φ_h =0.31 and varying N_h/N_c. [45]

1.3 Application of block copolymer

The various nanoscale structures of block copolymer and the tunable characteristics of block copolymer by engineering the component and volume fraction of the domains makes it interesting for potential applications. Several examples of the applications of block copolymer will be introduced in this section.

Block copolymer can be used as polymer electrolyte for rechargeable batteries. The electrolyte for rechargeable batteries not only requires high ion conductivity but also high mechanical stability. Both the requirements can be satisfied if one domain is conductive and the other domain mechanically stable. Poly(styrene-block-ethylene oxide) copolymer (SEO) can dissolve salt in PEO domain while PS domain is mechanically stable. There is a correlation between the distribution of Li in PEO domain and the conductivity.[8]

And also, block copolymer can be applied to bulk heterojunction polymer solar cell. For typical bulk hetero-junction polymer solar cell, in order to increase the interface area between donor and acceptor, kinetically trapped partially phase separated donor/acceptor structure is used. Therefore, the control of the donor/acceptor interface is almost impossible. The P3HT-b-PFTBT can form alternating donor-acceptor lamellar structure with face-on orientation in the crystalline P3HT. This results in controlled efficient donor and acceptor domains that are the pathways for electrons and holes, respectively.[9]

For one last example, block copolymer materials can to be used for responsive photonic gels. Photonic crystals with tunable light response in visible range are of interest for, for example, sensory devices. Hydrophobic-b-hydrophilic (PS-b-QP2VP) block

copolymer swells with the presence of fluid reservoir in direction normal to the lamellar direction and is able to change light response.[6]

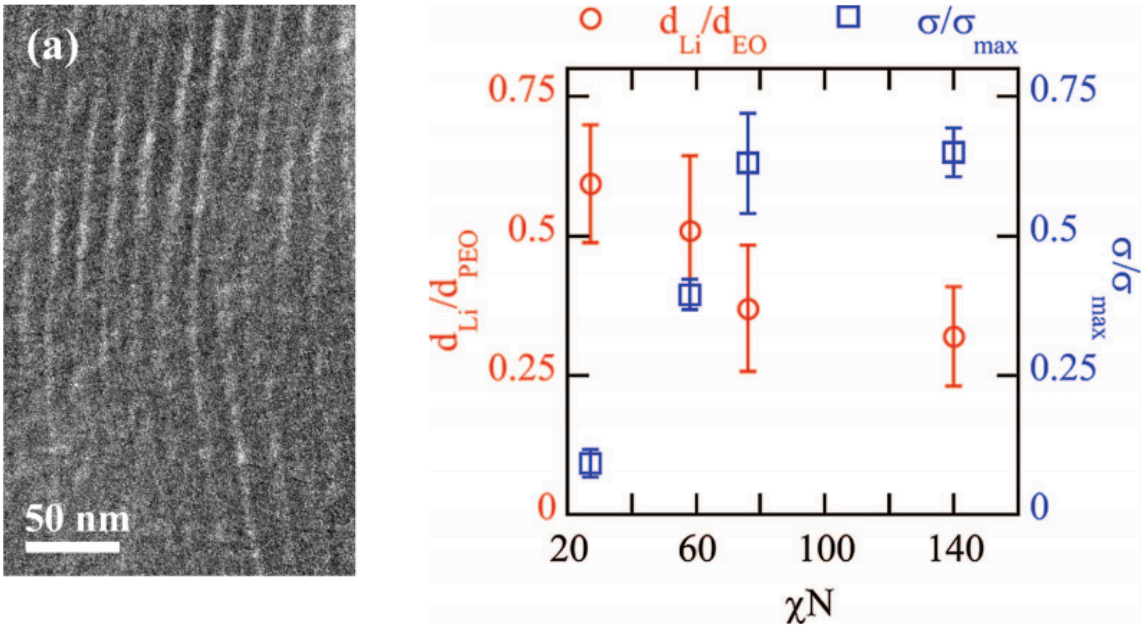

Figure 1- 8 (Left) EFTEM (Energy-filtered transmission electron microscopy) Li maps of unstained SEP copolymers (Right) [8] d_{Li}/d_{PEO} and normalized conductivity, σ/σ_{max}, as a function of molecular weight of the PEO chains, MW_{PEO}.

1.4 The effect of filler on grain structure of BCP

It was seen in previous section that in many applications block copolymer is blended with functional fillers to fulfill various performance, for example, conduct ions through salt-containing domain. However, the addition of fillers to block copolymer not only change the properties of the composite layer but also change the grain structure of the composite layer.

As shown in Figure 1- 9, Gido et al have reported that T-junction grain boundaries were found in abundance when I_2S miktoarm star copolymer was blended

with polyisoprene homopolymer. T-junction grain boundary is observed rarely in pristine block copolymer due to its high energy compared to other types such as chevron and omega of grain boundary. They have calculated the free energy of the case where the fillers swell the T-junction grain boundary and observed that it is lower than the free energy of the T-junction grain boundary in pristine block copolymer. They had free energy calculation that supported their observation of high frequency of T-junction grain boundary, however, the direct evidence of the location of filler was not provided.[46]

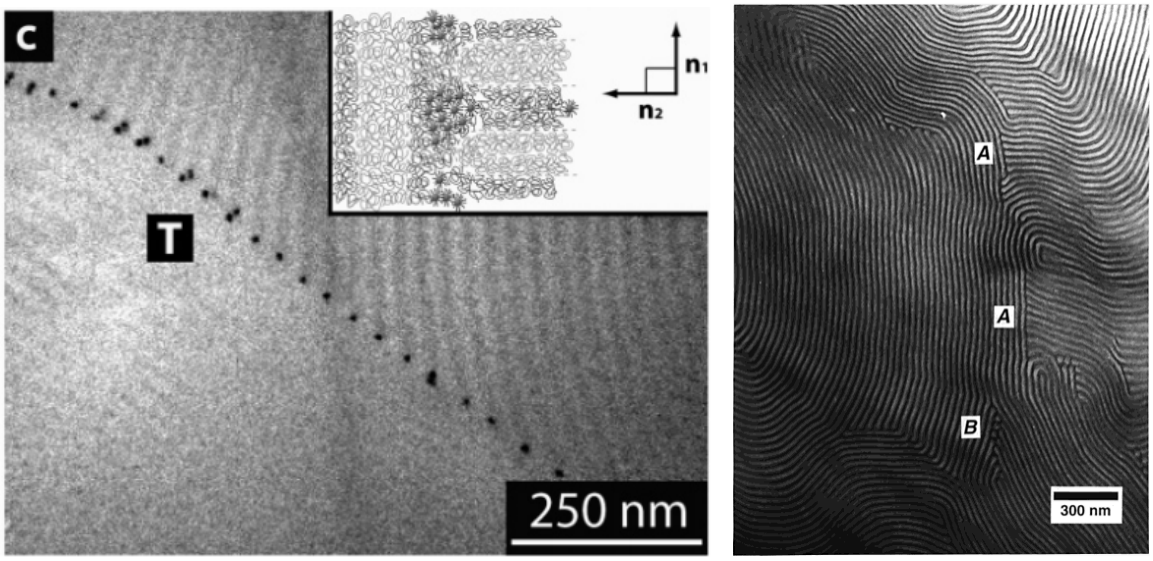

Figure 1- 9 TEM images of (Left) stained PS-PEP/AuSPS depicting a T-junction grain boundary (Right) I2S-hPI blend containing T-junction grain boundaries [46,47]

As shown in Figure 1- 9, Bockstaller and coworkers have directly observed the segregation of filler in high angle grain boundary by using polymer-coated nanoparticle additives. The distribution of nanoparticle filler depends on the level of perturbation of block copolymer morphology from equilibrium structure. For low angle grain boundary, the distribution of fillers was same as for equilibrium morphology, locating at the center

of the domain. However, for Omega and T-junction grain boundary, the fillers swelled grain boundary region that are regarded to have high elastic energy in order to lower the free energy of the system. This is the first experimental evidence of selective swelling the energetically unfavorable grain boundary.[47] It should be noted that Spontak and coworkers have shown that the equilibrium structure of BCP/nanoparticle blend is controlled by identical governing parameters with BCP/homopolymer blend, and this implies that, both the homopolymer and nanoparticle are expected to affect the defect formation in same principle rules. [48]

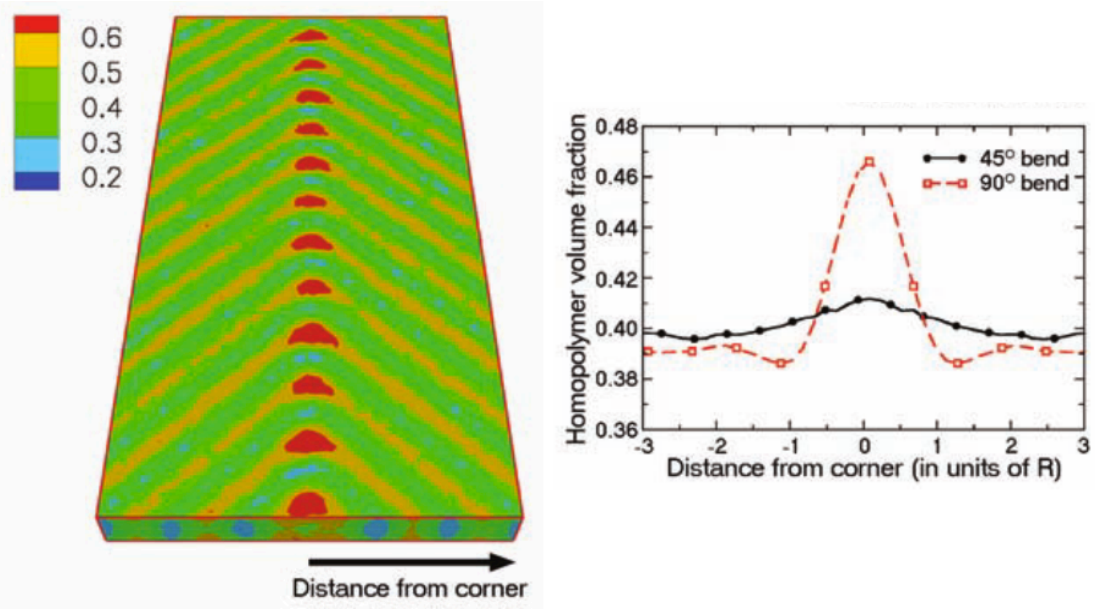

Figure 1- 10 (Left) Schematics of the SCFT calculation results of PS-PMMA/hPS/hPMMA ternary mixtures showing total homopolymer concentration (Right) The average total homopolymer concentration as a function of distance from corner for 45° and 90° bending angle.[49]

Paul Nealey et al have studies the structure formation of ternary blend of 60 wt% symmetric poly(styrene-b-methyl methacrylate) (PS-PMMA), 20wt% polystyrene homopolymer (hPS) and 20wt% poly(methyl methacrylate) homopolymer (hPMMA) for

their potential application in nanoscale manufacturing. They used SCFT calculation and as shown in Figure 1- 10 they observed the homopolymer segregation at corners where lamellar bends. And they also showed that the larger the bending angle the higher the homopolymer concentration at the corner.[49]

1.5 Research objective and hypothesis

The objective of this thesis research is to understand the driving forces and kinetics of filler segregation into grain boundary defects of granular block copolymer microstructure. For this purpose a combined electron imaging and ultra-small angle scattering analysis is performed. Two major hypotheses are to be tested.

The first hypothesis is that fillers will affect the kinetics of grain coarsening and the grain structure of block copolymer. The second hypothesis is that the filler-matrix interaction will affect grain-coarsening behavior of block copolymer.

1.6 Document organization

This thesis is composed of 7 sections. In the next chapter (Chapter 2), background information on (i) grain structure mapping using TEM (ii) Small Angle Neutron scattering (iii) application of small angle scattering to study grain size evolution in block copolymers (iv) Block-copolymers/homo-polymer blend systems will be introduced. In Chapter 3, experimental details will be illustrated with sample systems. And also characterization tools including Transmission Electron Microscope (TEM) and Differential Scanning Calorimetry (DSC) will be explained. In chapter 4, comparative study using Ultra-Small Angle Neutron Scattering and TEM based grain map construction on grain structure of block copolymer/filler system will be presented. The

calculation of the filler concentration in grain boundary using Invariant (Q) equation will be shown. In chapter 5, filler segregation kinetics will be studied by using McLean's approach for filler segregation. And the equilibrium concentration of filler in grain boundary will be calculated by McLean's isotherm. In chapter 6, conclusion of the thesis will be shown and will discuss about future plans.

2. Backgrounds

2.1 Grain mapping

Bockstaller et al. have used grain map technique to elucidate the role of grain boundary defects during grain coarsening of lamellar block copolymers. The grain maps were constructed for pristine PS-PI with thermal annealing for 0, 3, 7 days. The inverse relation between the frequency and energy of the grain boundary implied that the grain boundary energy is the governing parameter for the evolution of grain structures.

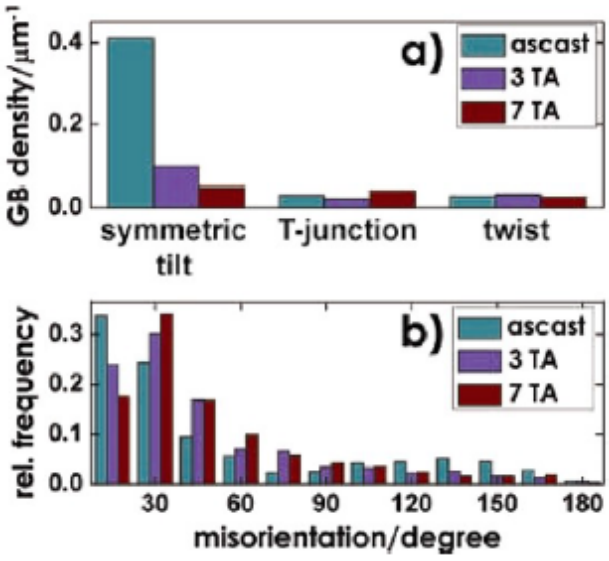

Figure 2- 1 (a) Evolution of grain boundary characteristics of pristine PS-PI during thermal annealing differentiated by grain boundary type (b) and angle of misorientation for the symmetric tilt boundary structure[41]

During the grain coarsening process, the density of symmetric tilt grain boundary decreased rapidly while that of the T-junction and twist grain boundaries remained constant. And especially the low-angle symmetric grain boundary played a major role in the reduced density of symmetric grain boundary. However, “inert” boundaries (such as

asymmetric tilt and twist boundaries) that do not participate in the annealing process were observed. In order to form ideal block copolymer structure with better uniformity, controlling the density of "inert" boundary was found be important. And addition of filler that can selectively interact with grain boundary was suggested as one of the strategies to facilitate grain coarsening. [41]

In the subsequent research, Bockstaller et al. have studied the effect of *athermal* filler addition on grain coarsening behavior of PS-PI block copolymer. They have observed retardation of grain growth for composite system and deviation of log-normal distribution of grain size which was characteristic of pristine PS-PI. The analysis of grain boundary energy suggested that filler lowers the energy of the grain boundary, therefore, the driving force for defect annihilation is reduced. The authors suggested tailoring the interaction between the filler and block copolymer could modulate the effect of filler addition on grain coarsening behavior. [50]

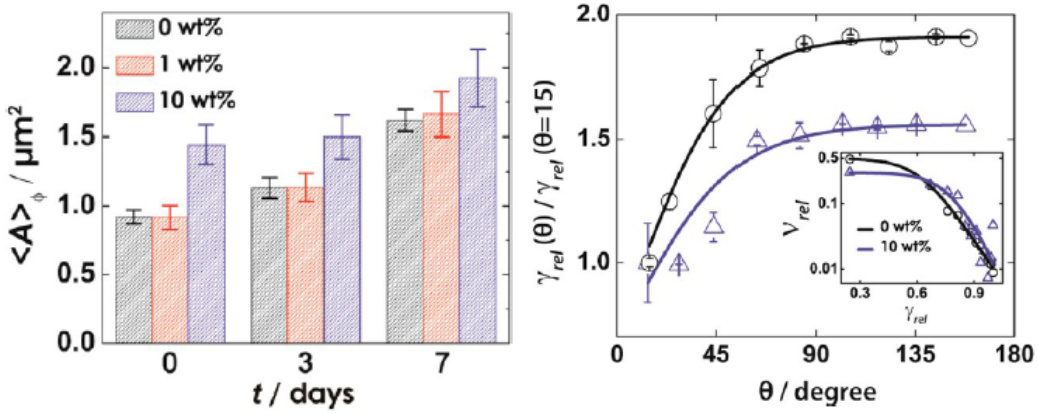

Figure 2- 2 (Left) Evolution of number-averaged grain cross-sectional area for prinstine as well as PS-PI/hPS blend systems with $\boldsymbol{\phi_{hPS} = 0.01}$ and $\boldsymbol{\phi_{hPS} = 0.1}$. (Right) Plot of relative GB tensions as a function of tilt angle after 7 days of thermal annealing in pristine PS-PI as well as PS-PI/h-PS (10wt%). [50]

2.2 Small-Angle Scattering

The diffraction of neutrons and X-ray by matter results from (1) scattering by individual electrons (X-ray) and individual atomic nuclei (neutron) and (2) interference of the scattered X-ray and neutrons from primary events. Because of this interference effect, the fluxes emanating different direction vary with direction. As we measured the flux with direction, we can infer the relative position of the individual electron (X-ray) and individual atomic nuclei (neutron). The term *scattering* involves the primary event (1) and *diffraction* involves the combination of (1) and (2), however, the distinction between them is often blurred. When the angle of interest is at small angle and the scattering pattern is diffuse rather then sharp, the term *scattering* is exclusively used. As the angle of interest in this thesis research is ultra-small to small angle, the word *scattering* will be used.[51] Small angle scattering measures structures of size 1Å or larger from the scattered X-ray or neutrons at small angle, typically $2\theta_s$ less than 2°. This discussion becomes more concrete with Bragg law:

$$\sin\theta_s = \frac{\lambda}{2d} \tag{2.1}$$

Thus, for block copolymer, when the period of microstructure, d, is about 100Å, the wavelength of neutron source is 1Å, then the scattered neutron will have peak at $2\theta_s$=0.6°.

2.2.1 Scattering and interference

In Figure 2- 1, a plane wave traveling in a direction specified by wave vector, $\mathbf{k_i}$, are scattered by two particles located at two points, O and P. A detector is place in direction specified by $\mathbf{k_f}$. If there is no phase change during scattering, coherent scattering,

the phase difference between the wave scattered at O and P depends on the path difference, δ, between two rays.

$$\Delta\phi = \frac{2\pi\delta}{\lambda} = \mathbf{k_i}\cdot\mathbf{r} - \mathbf{k_f}\cdot\mathbf{r} = -(\mathbf{k_f} - \mathbf{k_i})\cdot\mathbf{r} = -\mathbf{q}\cdot\mathbf{r} \qquad (2.2)$$

Here, $\mathbf{k_i}$ and $\mathbf{k_f}$ are wave vectors describing incident and scattered waves with absolute values of $|k_i| = |k_f| = {}^{2\pi}/_{\lambda}$. The $\mathbf{q}$ is referred to as scattering vector and it characterizes the incident and scattered beam direction and the wavelength. And the absolute value of $\mathbf{q}$ is related to scattering angle by

$$|\mathbf{q}| = q = \frac{4\pi}{\lambda}\sin\theta_s \qquad (2.3)$$

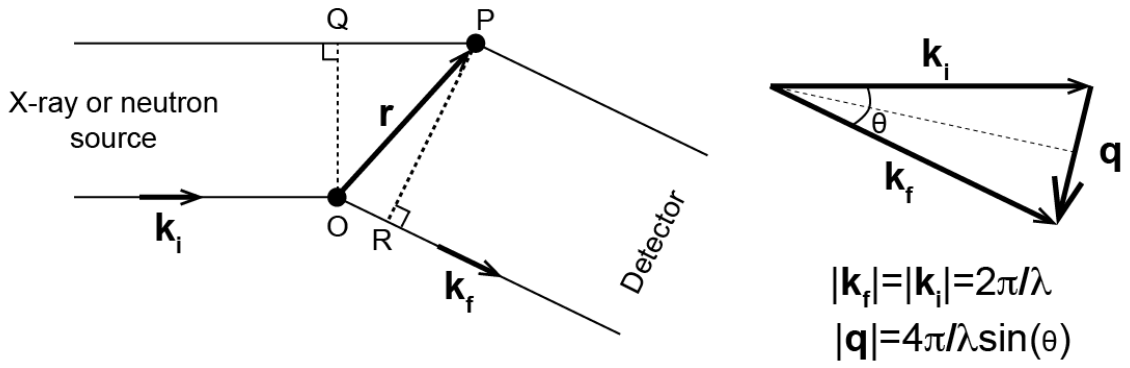

Figure 2- 3 Scattering triangles for an elastic neutron scattering [52]

Generally, two equations are used to represent scattering data in reduced form. One is the differential scattering cross-section per unit volume of the sample, $\Sigma_s(\mathbf{q})$, and the other is the interference function, $S(\mathbf{q})$.

$$\Sigma_s(\mathbf{q}) \coloneqq \frac{1}{V}\frac{d\sigma}{d\Omega} = \frac{1}{V}\frac{I(\mathbf{q}){A_{sd}}^2}{I_0} \qquad (2.4)$$

Here, $d\sigma/_{d\Omega}$ is the differential cross-section and denotes the probability that a neutron impinging on sample will scatter into a unit solid angle in the given direction. A_{sd} is the sample to detector distance. The different scattering cross-section per volume, $\Sigma_s(\mathbf{q})$, is dependent on the scattering power of the particles in the sample. For light, the scattering intensity depends on the refractive indices, for X-ray on the electron density and for neutron on the 'scattering length' densities.

The second equation, interference equation, can be used for scattering data in system consisted of one class of particles.

$$S(\mathbf{q}) \coloneqq \frac{I(\mathbf{q})}{I_m N_m} \tag{2.5}$$

Here N_m represents the number of particles in the system and I_m represents the scattering intensity from individual particles. Therefore, $S(q)$ measures the ratio between the experimentally measured scattering intensity and the total scattering intensity from the particles if they were all measured separately or if they the particles were to scatter incoherently.

The two equations, $\Sigma_s(\mathbf{q})$, $S(q)$, are related by the equation:

$$\Sigma_s(\mathbf{q}) \coloneqq \langle c_m \rangle \left(\frac{d\sigma}{d\Omega}\right)_m S(\mathbf{q}) \tag{2.6}$$

Here, the $\left(\frac{d\sigma}{d\Omega}\right)_m$ denotes the scattering cross-section per particle and $\langle c_m \rangle$ denotes the mean density of the particle, N_m/V.

The efficacy of neutron scattering by nucleus is expressed by the *scattering length* b of the nucleus.

$$\frac{d\sigma}{d\Omega} = b^2 \tag{2.7}$$

The strength of the nucleus-neutron interaction depends on the details of the nuclear structure, which is not related to the atomic number in any simple way. Therefore, the magnitude of the scattering length b can vary greatly between elements neighboring in terms of atomic number or mass, and even between isotopes of the same element.

2.2.2 Coherent and Incoherent Scattering

A neutron is an uncharged elementary particle, possessing a mass m equal to 1.675 x 10^{-24}g and spin 1/2. Neutron is scattered by a single atomic nucleus resulting from their interaction with it through nuclear forces. The incoherent component of neutron scattering results from the random variability of scattering length of individual nuclei. This is because the neutron, with spin of 1/2, interacts with nucleus of spin i and results total spin of i+1/2 or i-1/2 in nucleus-neutron system. The total differential cross section is given as:

$$\frac{d\sigma}{d\Omega} = \langle b \rangle^2 \sum_{j,k} e^{-iq(r_j - r_k)} + N(\langle b^2 \rangle - \langle b \rangle^2) \qquad (2.8)$$

The first term on the right is the total intensity if all the nucleus have identical scattering length density equal to b. The second term on the right is does not depend on $r_j q$ and, therefore, contains no information on the structure of material. The first term and second term is called the coherent and incoherent component of the intensity, respectively.

2.2.3 Deuterium labeling

Neutron scattering is much more powerful for studying polymer research when used in conjunction with deuterium labeling. Deuterium is one of two stable isotope of hydrogen and has essentially identical physical properties. However, the cross section for scattering neutron is greatly changed. The value of b_{coh} ^{1}H is -0.374 x 10^{-12}cm and the

value for ^{2}D is 0.667 x 10^{-12}cm. Therefore, by substituting hydrogens with deuteriums in only some of the molecules, we can make the deuterium molecules visible to neutron beams without changing the thermodynamic properties in any appreciable way.

2.2.4 Ultra-small angle neutron scattering for grain coarsening study

In order to achieve ultra-small q ranges, instead of choosing long wavelength and long flight paths, an entirely different instrument concept is used. Thermal wavelength neutron (peak wavelength of 2.4Å) and perfect single crystals are used in USANS. Very narrow beam collimation is achieved by using Bonse-Hart method. Neutron filters (sapphire filter, graphite filter) are used to filter out higher components of the energy spectrum. Pre-monochromator is used to reduce the radiation level on the monochromoator and other components. The USANS uses triple reflection from the single crystal silicon monochromator and analyzer in order to achieve very narrow $\Delta\lambda/\lambda$ and high collimation.

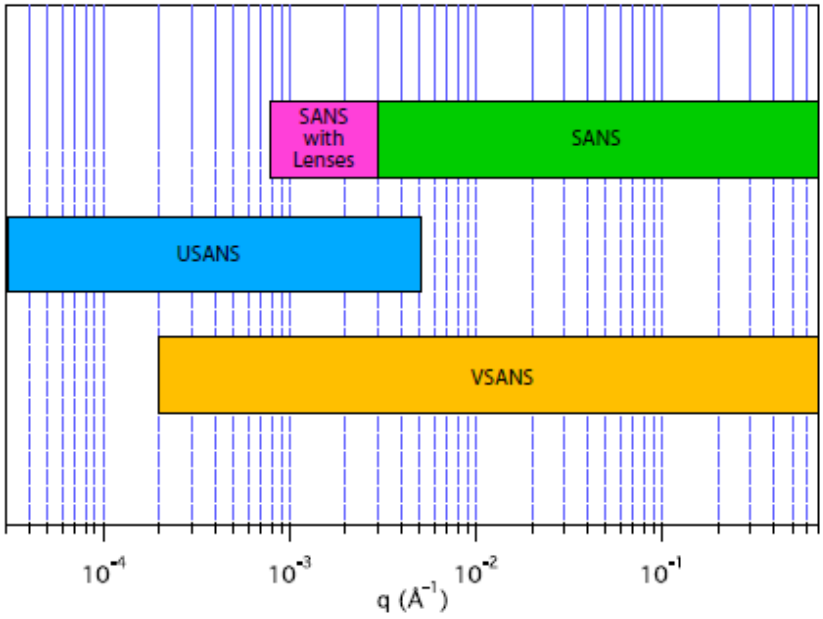

Figure 2- 4 The q-ranges of SANS, USANS and VSANS.

Cohen et al. have used Ultra-Small Angle X-ray Scattering (USAXS) to investigate the grain structure of low-molecular weight styrene-butadiene block copolymer. The USAXS provided a scattering vector, q, from 0.0004 to 0.1Å^{-1}. As shown in Figure 2- 5, they have observed clear peaks in low q that they used to obtain the grain size by using spherical form factor.

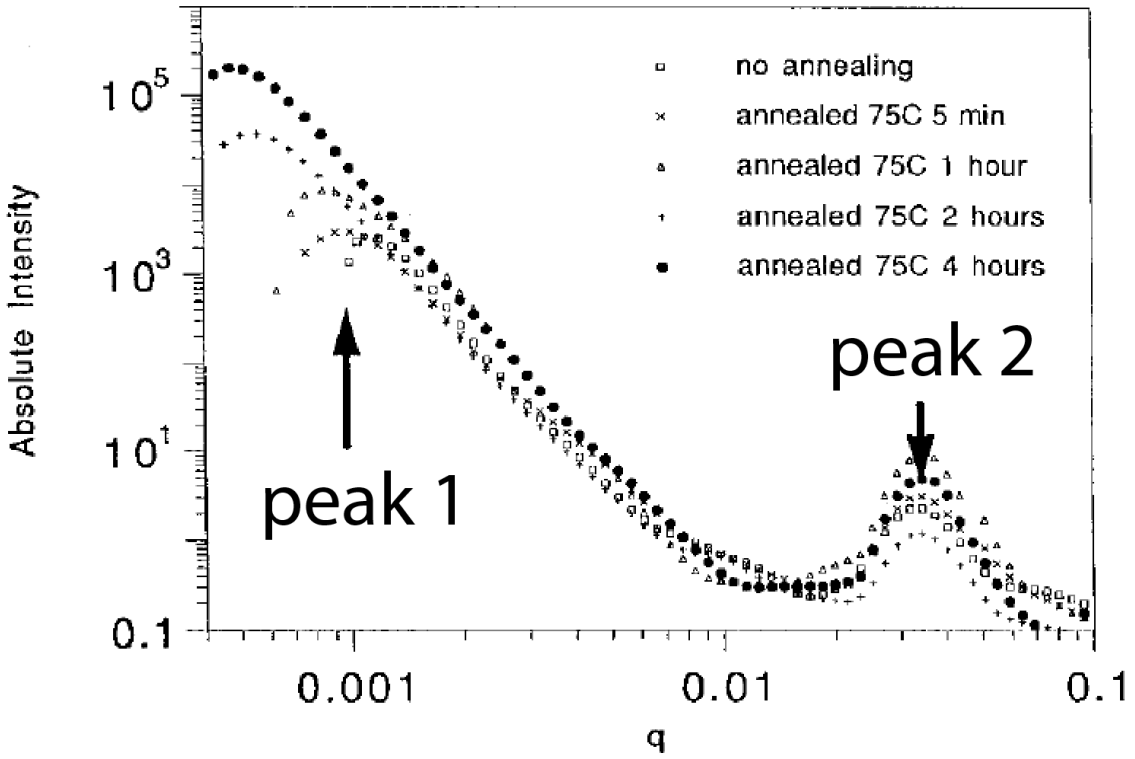

Figure 2- 5 Logarithm of absolute intensity vs log q at various annealing times for the polystyrene-b-polybutadiene block copolymer observed by Ultra-Small Angle X-ray Scattering. [24]

They have proposed scattering mechanism for low q explained by the difference in electron density between the grain boundary and the grain. The Porod's law constant and the value of the scattering invariant were used to verify the proposed scattering

mechanism by comparing the calculated electron density contrast and volume fraction of the grain boundary. Figure 2- 5 shows the logarithm of absolute intensity vs log q for polystyrene-1,2-butadiene block copolymer with different thermal annealing time. The peak denote as "peak 1" corresponds to the grain diameter and "peak 2" corresponds with lamellar spacing. It is observed that the grain size increases with thermal annealing. Figure 2- 6 illustrates the proposed mechanism of scattering from grain structure. The dark line shows the electron density differences between grain and its boundary that corresponds with the peak in ultra-small q. [24]

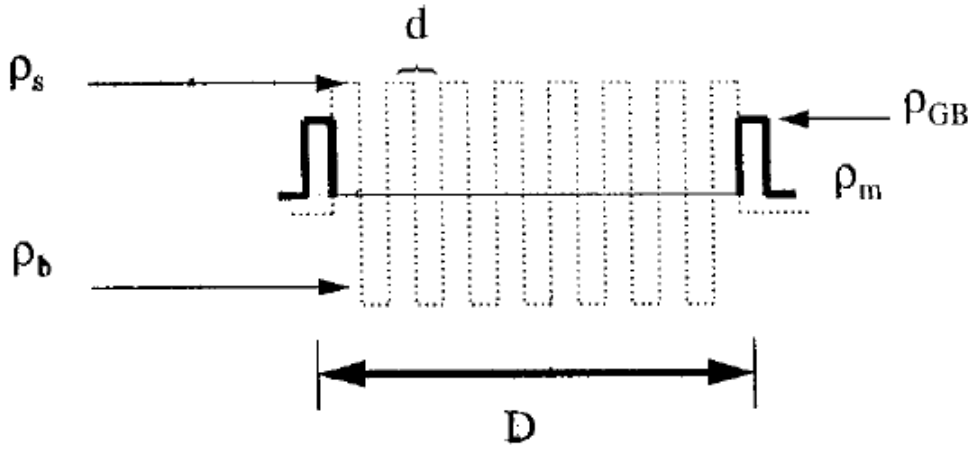

Figure 2- 6 Schematic representation of proposed mechanism of grain boundary scattering for Ultra-Small Angle X-ray Scattering [24]

2.2.5 Invariant

The invariant Q is calculated by integrating the scattered intensity with respect to s throughout the reciprocal space:

$$Q = \frac{1}{(2\pi)^3} \int I(q)\, dq \tag{2.9}$$

For the case of isotropic materials, the invariant can be written as:

$$Q = \frac{1}{2\pi^2}\int_0^\infty q^2 I(q)dq \tag{2.10}$$

The invariant represents the scattering power of the material that takes into account all the possible scattering geometry. The invariant can also be written as:

$$Q = \langle\rho^2\rangle V \tag{2.11}$$

The average scattering length density of an ideal two-phase system is

$$\langle\rho\rangle = \phi_1\rho_1 + \phi_2\rho_2$$

and η_1 and η_2 are given

$$\eta_1 = \rho_1 - \langle\rho\rangle = \Delta\rho\phi_2 \tag{2.12}$$

$$\eta_2 = \rho_2 - \langle\rho\rangle = \Delta\rho\phi_1 \tag{2.13}$$

where

$$\Delta\rho = \rho_1 - \rho_2 = \eta_1 - \eta_2 \tag{2.14}$$

The invariant is then

$$Q = V\langle\eta^2\rangle = V(\eta_1^2\phi_1 + \eta_2^2\phi_2) = V(\Delta\rho)^2\phi_1\phi_2 \tag{2.15}$$

The invariant in this experiment is defined as the area under the curve Iq^2 vs q plot resulted from grain boundary scattering.

$$Q = \frac{1}{2\pi^2}\int_0^\infty i(q)q^2dq = \phi(1-\phi)(\rho_{GB} - \rho_m)^2 \tag{2.16}$$

where ϕ is the volume fraction of grain boundary, ρ_{GB} is the scattering length density of grain boundary and ρ_m is the scattering length density of mean grain density. If the volume fraction of the grain boundary is known, the invariant value C2 can be used to calculate the $(\rho_{GB} - \rho_m)^2$. This information will be useful to us because the filler segregation in grain boundary is suspected in our experiment and this will increase the $(\rho_{GB} - \rho_m)^2$.

2.2.6 Porod's law

In ideal two-phase system, for large q, the $I(q)$ is expected to decay with power exponent of -4 and the proportionality constant is related to the total area S_p of the boundary of the two phases.[51] It can be rewritten as, $q \to \infty$

$$I(q) \to \frac{2\pi(\Delta\rho)^2 S_p}{q^4} \tag{2.17}$$

As shown in Figure 2- 7, Porod region corresponds to a probed range, $2\pi/q$, that is smaller than the scattering object. In this Porod region, the scattering is resulting from the local surface structure. If the interface is smooth, the Porod law yields scattering intensity that decays with exponent -4.

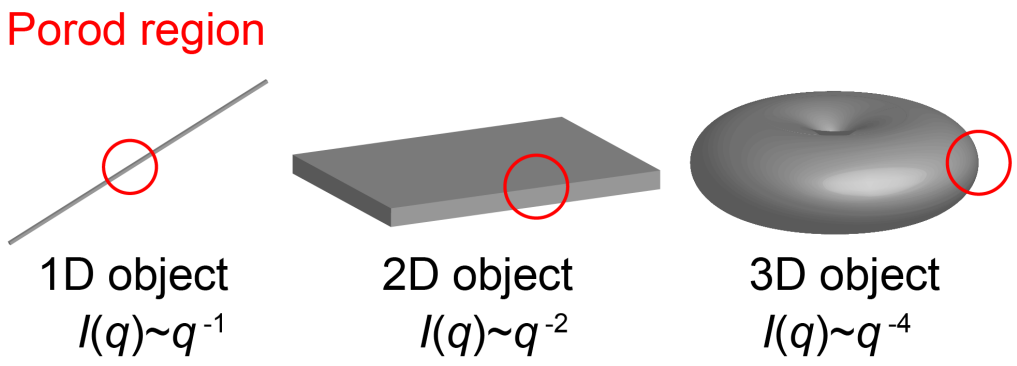

Figure 2- 7 Assortment of Porod law behavior for different shape objects. The red circle shows the probe range that corresponds to Porod region.[53]

2.2.7 Guinier scattering

Even when the shape of the object is random and irregular, it stills follows universal scattering function in the limit of small q. The equation, called Guinier law, is given by

$$I(q) = \rho_0^2 v^2 \exp(-\frac{1}{3} q^2 R_g^2) \quad (2.18)$$

Here, ρ_0 is the average scattering length density per particle, v the particle volume and R_g is the radius of gyration of a particle of unknown shape.

In order for Guinier law to hold, (1) q range should be much smaller than $1/R_g$, (2) the system should be dilute so that there is no interference between scattered rays (3) the system should be isotropic (4) the matrix should not have internal structure in the interested range of q. [51]

2.2.9 Power-law/Fractal scattering

The inverse power-law exponent for 1, 2, 4 are scattering from thin rod, thin disk and sphere, respectively. However, there are many cases where the intensity decays in different or fractional power of q. The inverse power-law exponent that differs from 1, 2, 4 can be explained with the concept of fractal scattering. Fractal is a structure that shows a self-similar shape in different size range. The Koch curve is a good example of fractal structure.

The most important characteristic of fractal structure is fractal dimension. Suppose we draw a sphere of diameter r around a point in a fractal object. If the fractal object is a line, the mass $M(r)$ within a sphere is proportional to r. If it is a sheet, $M(r)$ will be proportional to r^2. If it is a solid three-dimensional object, $M(r)$ will be proportional to r^3. Therefore, there is a general relation between $M(r)$ and r:

$$M(r) \propto r^{d_m} \quad (2.19)$$

where d_m is the mass fractal dimension and can be any value between 1 and 3.

And as the volume of a sphere is proportional to r^3, the density $\tilde{\rho}(r)$ and correlation function, probability of finding a mass point at a distant r, of the object inside the sphere is given by:

$$\tilde{\rho}(r) \sim \gamma(r) \propto r^{d_m - 3} \tag{2.20}$$

This is valid with the range, $R \gg r \gg a$, where R is the overall dimension of the object (R_g), and a is the fundamental building block of the fractal structure, for example, atom or a molecule. As the intensity of scattering $I(q)$ is given by

$$I(\mathbf{q}) = \int \Gamma_\eta(\mathbf{r}) e^{-i\mathbf{qr}} d\mathbf{r} \tag{2.21}$$

$$\propto \frac{1}{q} \int_0^\infty r^{d-2} \sin qr \, dr \propto q^{-d_m} \tag{2.22}$$

Which is valid for $q/R \ll q \ll 1/a$.

The intensity of the scattered beam from mass fractal decays with power exponent between -1 and -3.

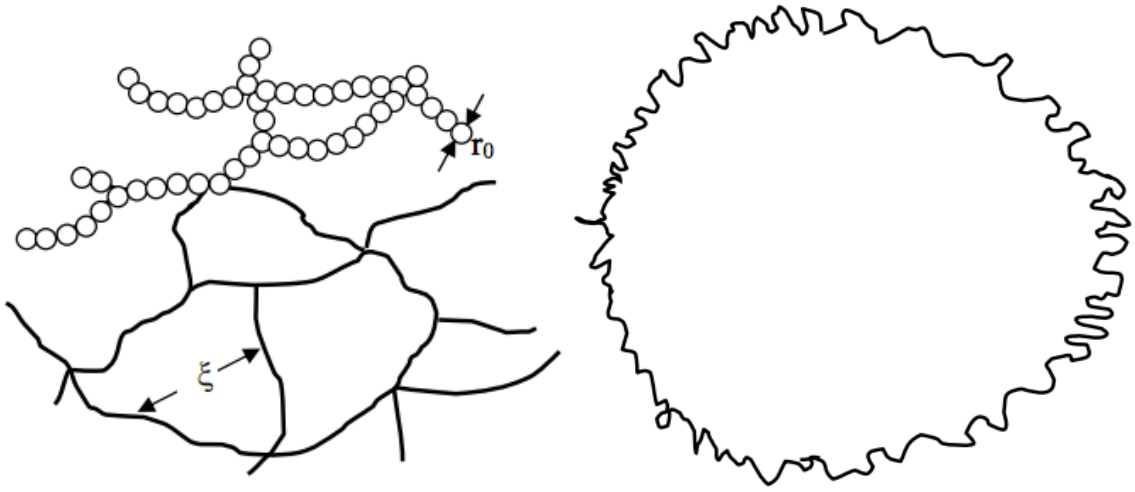

Figure 2- 8 Schematic representation of (left) mass fractal structure containing branching points and crosslinks (right) surface fractal structure of intermediate roughness [51,53]

Surface fractal structure has rough surface or fractal structure on surface. Let's assume a fractal interface that divides phase 1 and phase 2. And we further divide each phase into surface (S) and bulk (B) region. If we draw a sphere of radius r on every point of the interface (A), the envelope of the sphere is the trace (=that divides between the surface and bulk region.

From the similar derivation for Porod scattering, we obtain the scattered intensity:

$$I(q) \propto q^{-(6-d_s)} \tag{2.23}$$

The log-log plot of the scattered beam from three-dimensional surface fractal, d_s, surface fractal dimension, is between 2 (smooth surface) and 3, will decay with power-law exponent between -3 and -4.

2.2.10 Correlation function of lamellar structure

The scattered intensity I(q) is the absolute square of the Fourier transform of scattering length density ρ(r): [51]

$$I(q) = |A_n(q)|^2 = \left| \int_V \rho(r) e^{-iqr} dr \right|^2 \tag{2.24}$$

$A_n(q)$:Amplitude of the scattered neutron

$\rho(r)$: Scattering length density

Equation (1) can be rewritten with new variable $r = u' - u$

$$I(q) = A_n(q) \cdot A_n{}^*(q) = \left[\int_V \rho(u') e^{-iqu'} du' \right] \left[\int_V \rho(u) e^{-iqu} du \right] \tag{2.25}$$

$$= \int \left[\iint \rho(u)\rho(u+r)du \right] e^{-iqr} dr \tag{2.26}$$

$$= \int \Gamma_\rho(r) e^{-iqr} dr \tag{2.27}$$

Here $\Gamma_\rho(r)$ is defined as $\Gamma_\rho(r) = \int \rho(u)\rho(u+r)du$ and is called as autocorrelation function or sometimes just simply as correlation function. The autocorrelation function $\Gamma_\rho(r)$ tells us how the densities $\rho(u)$ and $\rho(u')$ separated by distance(r) are correlated with each other.

From the experimentally observed 1-dimensional intensity $I_1(q)$, the one-dimensional correlation function can be obtained using following equation:

$$\Gamma_1(x) = \frac{1}{2\pi} \int_{-\infty}^{\infty} I_1(q) e^{iqx} dq = \frac{2}{2\pi} \int_0^{\infty} I_1(q) \cos qx \, dq \tag{2.28}$$

Here, $I_1(q)$ is the one-dimensional scattering pattern and if the specimen contains many lamellae stacks in all random directions, the observed scattering pattern $I(q)$ is isotropic and $I_1(q) \propto 4\pi q^2 I(q)$.

And the normalized one-dimensional correlation function $\gamma_1(x)$ can be evaluated by

$$\gamma_1(x) = \frac{\int_0^{\infty} I_1(q) \cos qx \, dq}{\int_0^{\infty} I_1(q) \, dq} \tag{2.29}$$

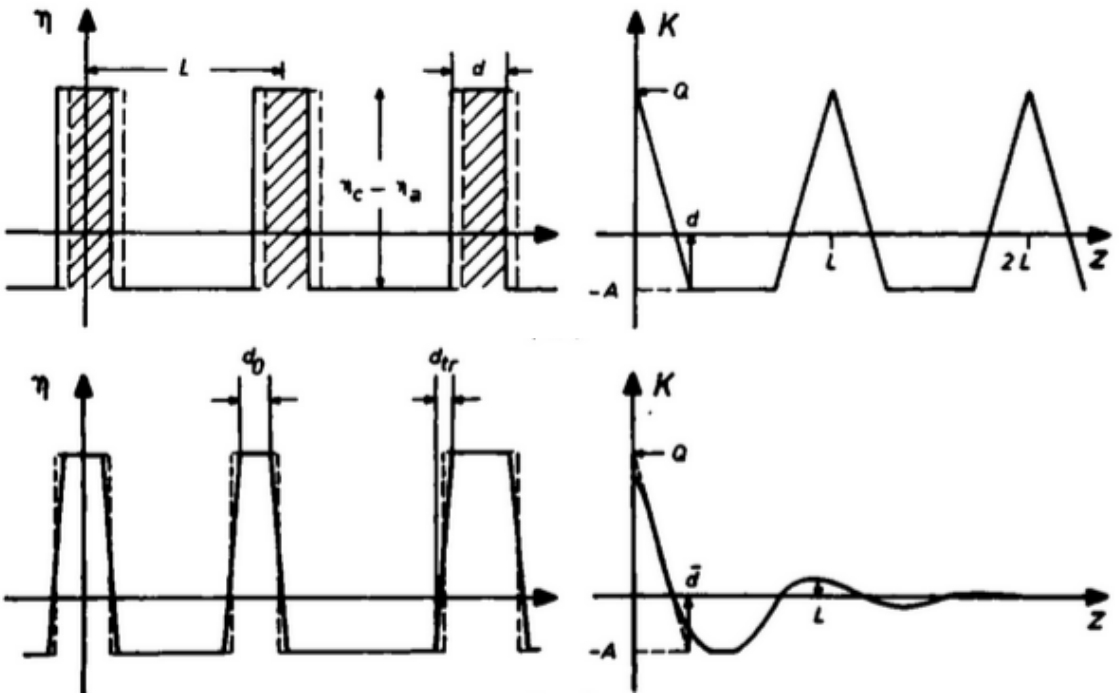

Figure 2- 9 Electron density distribution $\boldsymbol{\eta(z)}$ and related correlation function K(z) for lamellar systems. (Top) Periodic two-phase system (Bottom) Effect of introduction of diffuse phase boundaries.[54]

3. Experimental Methods

3.1 Sample preparation

3.1.1 Materials

Symmetric poly(styrene-isoprene) (PS-PI) block copolymer was purchased from Polymer source. Molecular weight of PS block is 45,000g (M_n) and that of PI block is 46,000g (M_n). The polydispersity of PS-PI is 1.07. Deuterated polystyrene was also purchased from Polymer source. The Molecular weight is 20,000g (Mn) and the polydispersity is 1.08. PS-PI was used as a model system because of several reasons: First, PS-PI derived BCP are important materials as thermoplastic elastomers. Second, PS-PI has been researched extensively, therefore, rich set of reference data regarding phase behavior and thermodynamic parameter is available. Third, both the PS and PI are stable for TEM imaging and can be easily imaged by selectively staining PI using OsO_4.

Material	Scattering cross section (1/cm)		Scattering length density(10^{-6}/Å^2)	
	Real	Incoherent	Real	Incoherent
PS (C_8H_8)	0.026	3.861	1.40	17.194
d-PS (C_8D_8)	0.536	0.099	6.41	2.748
PI (C_5H_8)	0.001	5.222	0.27	20.963

Table 3- 1 Neutron scattering cross-section and scattering length density of materials[53]

The scattering length density of polystyrene, polyisoprene and deuterated polystyrene was calculated from NCNR website and also by myself. The summary of

scattering cross-section and scattering length density of materials are shown in Table 3-1.

3.1.2 Sample preparation

Deuterated polystyrene was added to poly(styrene-isoprene) for 10wt% mixture. Toluene was added to the mixture to make 5wt% polymer solution which gives less than 1mm thickness film after film casting procedure. Toluene is chosen as a solvent because it is non-preferential solvent to either of the blocks. The polymer solution was stirred 24hr at room temperature. The polymer mixture was placed in a vacuum of ~80mbar for 8 hours to evaporate the solvent. The pressure was controlled by Buchi Rotovapor R-200. After that, it was moved to vacuum chamber with vacuum level of (?) to fully dry. For thermal annealing, the films were place in vacuum oven and the temperature was increased to 130°C. Then, each sample was sectioned to 70nm thickness by using LEICA EM FCS cryo-ultramicrotome. To increase the electron density contrast, the samples were stained using osmium tetroxide (OsO_4, obtained from EM Sciences).

3.2 Grain boundary mapping using TEM

The former student of our group has introduced real space analysis of microstructure of block copolymer using combination of serial imaging/image reconstruction and image analysis. I will briefly summarize the technique in order to help understanding the procedure. Figure 3- 2 illustrates the steps of grain boundary mapping procedure.

3.2.1 TEM imaging

Electron imaging of BCP microstructure was performed using a JEOL 2000 FX electron microscope, shown in Figure 3- 1, operated at 200kV. The Imaging was based on the amplitude and phase contrast, the images were recorded by a Gatan Orius SC600 high-resolution camera. The magnification used for images was 5000X. For grain map construction, ~100 images were taken.

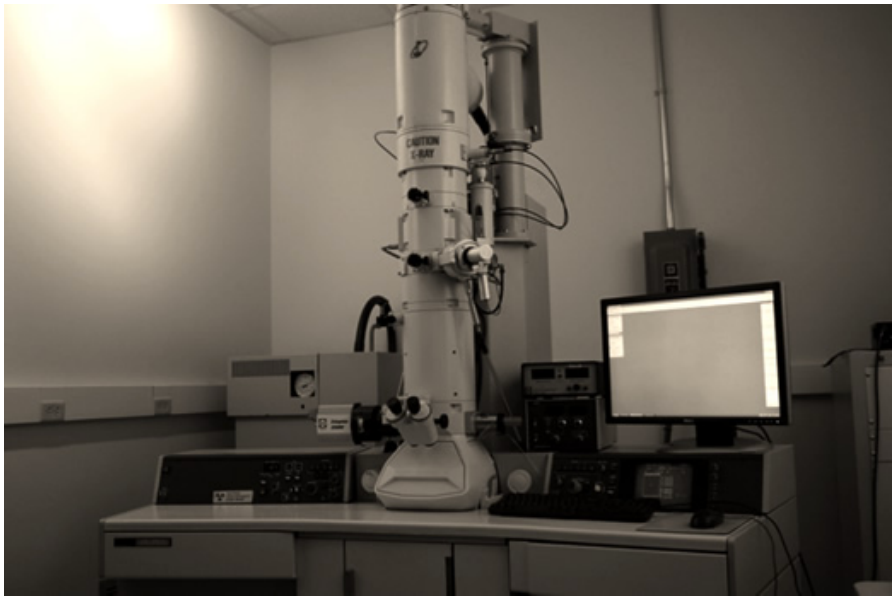

Figure 3- 1 JEOL JEM-2000EX Transmission Electron Microscope

At least 500μm^2 area of block copolymer was imaged in order to provide statistically reliable data. All the images were taken at 5000x magnification. Figure 3- 2 illustrates the experimental procedure for TEM imaging and the reference coordinate system.

3.2.2 Image Processing

In order to facilitate the image analysis using MATLAB, TEM images were skeletonized using ImageJ. The skeletonized TEM images of lamellar block copolymer

are composed of 1-pixel thickness lines that correspond with the lamellar orientation. The first step to skeletonize the TEM image is to make binary image. TEM image is composed of 8-bit gray-scaled pixels with 0 being the brightest and 255 being the darkest. And any value between 0 and 255 is displayed as scaled gray dots. For PS-PI, after the staining the PI domain with OsO_4, PI look darker than PS because of heavy metal bonding. However, there exist additional contrasts resulting from non-uniform sample thickness and knife marks. Therefore, image enhanced should be conducted before binarizing an image in order to improve the contrast between PS and PI and suppress the artifacts. The order of image processing is as follow. First, Fourier bandpass

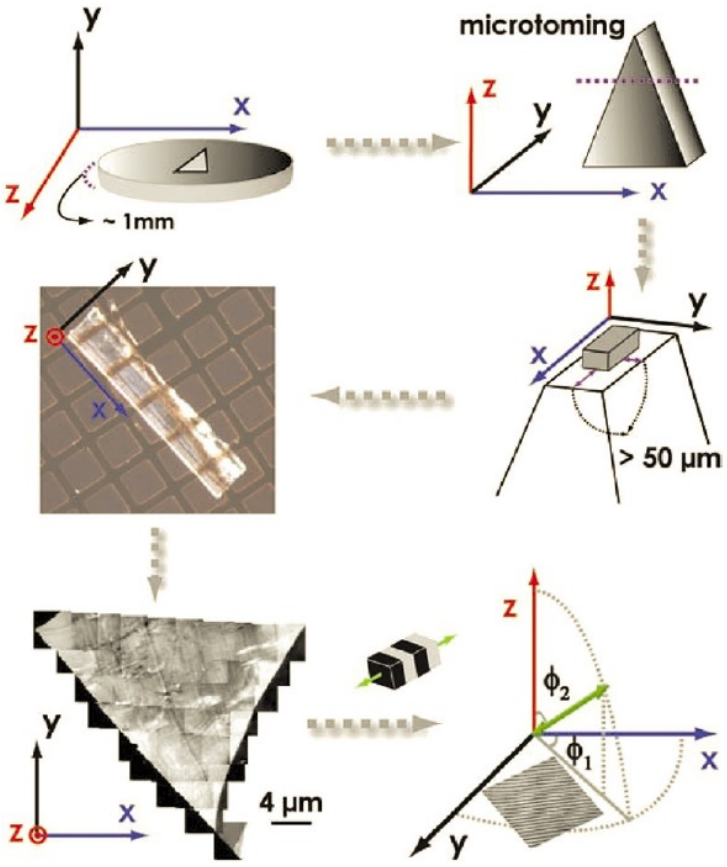

Figure 3- 2 Illustration of experimental approach applied in microstructure analysis of lamellar block copolymer. Film casting geometries define the reference coordinate system. Longitude and latitude are determined for lamellar orientation. [41]

filtering was applied on the electron micrographs. It performs Fourier transform on the image in the frequency spatial domain. By adjusting the low-band pass (smoothing) and high-band pass (losing larger structure), you can get a suitable image without knife marks and shades. Secondly, Convolution filter, neighborhood processing, is applied on Fourier bandpass filter image. The destination pixel is calculated by multiplying each source pixel by its corresponding convolve filter coefficient and adding the results. Here the convolution filer was applied to sharpen the interface between PS and PI as well as to improve the contrast. Then, the mathematical operation, square, is applied in order to increase the difference of gray-scaled intensities between PS and PI. Finally, the binarized image was skeletonized. The skeletonization process converts the binary image into lines without losing structure characteristics, therefore, makes it easier for the subsequent image analysis with MATLAB. Then, the skeletonized images are stitched together by using Photoshop software.

3.2.3 Image Transform

To acquire structural information from skeletonized electron microscopy image, Hough Transform (HT) or discrete Fourier Transform (DFT) was utilized. By either applying HT or DFT on the skeletonized image, we can obtain structural parameters such as lamellar orientation and repeat distance. The image transform done in this study is conducted by MATLAB code written by our previous lab member. The content of the MATLAB code will be explained briefly: (1) One pixel in the reconstructed skeletonized image becomes a center of a small-sized window (30 x 30 pixel). (2) either HT or DFT is applied on the window in order to obtain average lamellar orientation and repeat distance. (3) The next pixel is set as the center of the window and either HT or DFT is applied on

the window (4) While applying this process to entire pixel of the image, two separate matrix with one containing the lamellar orientation and the other containing the lamellar repeat distance are obtained.

3.2.4 Determination of orientation parameter – Longitude and Latitude

In this study, the lamellar normal direction is utilized to characterize the microstructure of BCP. Only two parameters are needed to designate the orientation of lamellar due to the geometrical symmetry of lamellar shape. The longitude is the in-plane angle between the lamellar normal and the x-axis, while the latitude is the out-of-plane angle between the lamellar normal and the y-axis. While the longitude can be directly acquired from image transform matrix, latitude should be calculated by utilizing geometrical relation between the repeat distance of lamellar and latitude. In this study, we assume that the most texture information is contained in longitude only because of ambiguity in determining the latitude and the narrow distribution of latitudes observed in the experiment.

3.2.5 Grain boundary identification

In this study, the grain boundary is identified, from the longitude matrix, by detecting edges, across which the value of longitude changes more than 15 degrees. As the misorientation angle becomes larger than 15 degrees, the energy penalty per chain is significantly larger than the thermal energy. Thus, we choose 15 degrees as meaningful criterion for lower bounds of misorientation. With the identified grain boundaries, the grain map of sample can be obtained and from which we can investigate various structural parameters such as grain size distribution, lamellar orientation distribution, grain boundary orientation distribution, and the type and frequency of grain boundaries.

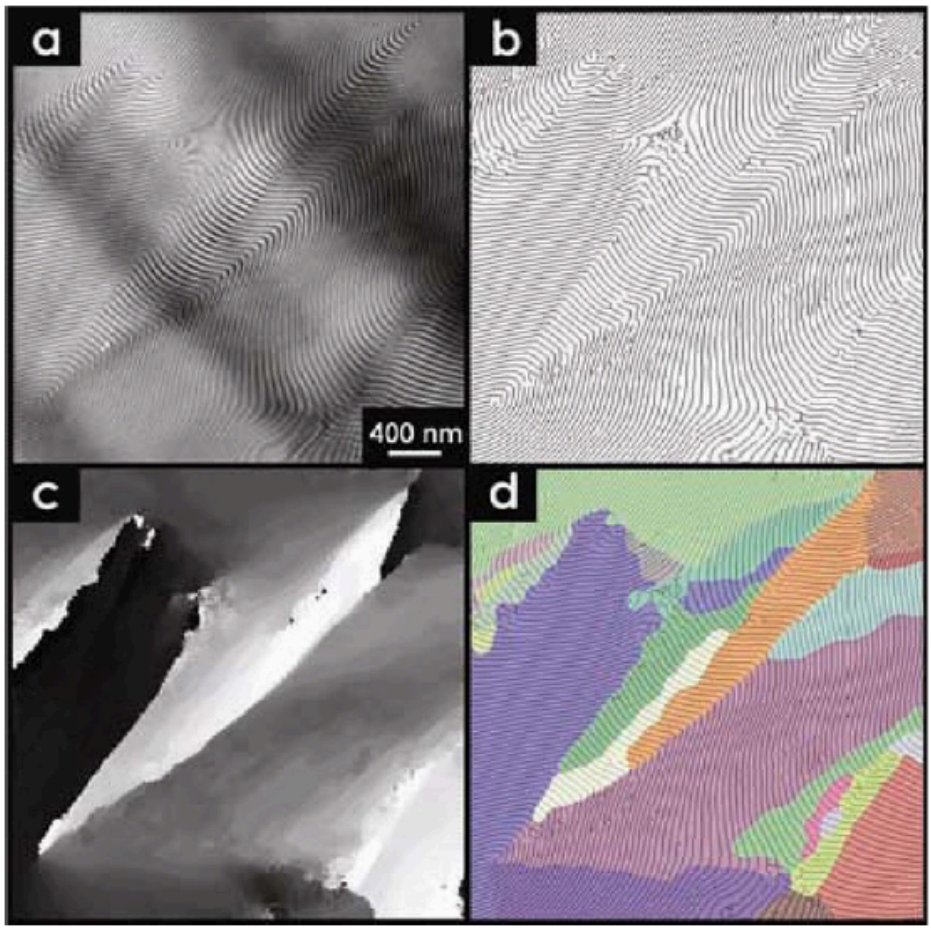

Figure 3- 3 Illustration of image analysis procedure (a) The original TEM image (b) skeletonized image (c) gray-scale image corresponding to the orientation of lamellae, black and white corresponds to "zero" and 180 longitude value (d) Based on the longitude and latitude, grain map was constructed [41]

3.3 Neutron scattering

3.3.1 Ultra Small Angle Neutron Scattering

NCNR's BT5 USANS was used to measure scattered neutrons from large-scale structure. The q ranges measured were $3\times10^{-5}\text{Å}^{-1} < q < 3\times10^{-3}\text{Å}^{-1}$ which corresponding to $0.2\mu m < r < 21\mu m$. Pyrolytic Graphite Premonochromator followed

by a Triple-Bounce Si(220) monochromator was used. The wavelength of the neutron beam is 2.4Å and the wavelength spread is 6% $\frac{\Delta\lambda}{\lambda}$. The sample was ~1cm in diameter and ~250μm in thickness. After placing the sample in sample holder, it was covered by aluminum foil. The data reduction was performed using SANS reduction macro made by NCNR.

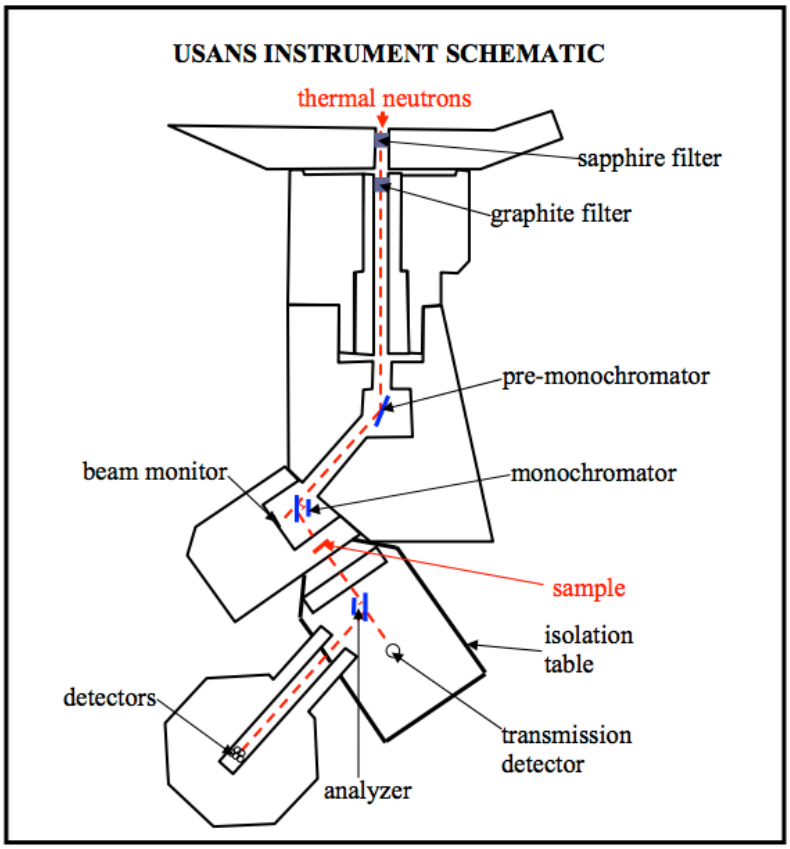

Figure 2- 10 Description of BT5 USANS system

3.3.2 Overview of USANS data reduction

In general, a complete USANS measurement will consist of sample and empty cell scattering measurement and also the correction for background count-rate. The USANS instrument at NIST is of Bonse-Hart type using triple bounce silicon crystals for

the monochromator and analyzer. As a result, data are collected point-by-point in discrete angular steps , making the raw data inherently one-dimensional. Scattering measurements are divided to several files, each covering separate non-overlapping q-ranges. Since the intensity is measured across the central beam, the transmission data of the sample is implicitly included.

Data reduction procedures automatically detect the zero angle peak of the main beam, convert the angle into q (1/Å), and normalize to monitor counts and counting time. The transmission measured by analyzer is determined by measuring the peak intensity with and without the sample: $T_{Rock} = I(\text{peak})_{\text{sample}}/I(\text{peak})_{\text{empty}}$. The transmission is calculated again with the position of the analyzer detuned (angles greater than 2°) by measuring the ratio of counts with and without the sample. Also, wide angles are used because the transmission detector countrate is attenuated at analyzer angles close to the main peak and shown as $T_{Wide}=TRANS_{sample}/TRANS_{empty.}$

The data correction is conducted using the following equation:

$$I_{COR}(q) = I_{SAM}(q) - T_{rock}I_{EMP}(q) - \big(1 - T_{rock}\big)I_{BGD} \qquad (3.1)$$

Here, I_{SAM} is the sample scattering, I_{EMP} the empty scattering and I_{BGD} the background scattering.

Corrected data is converted to absolute scale using the following scaling factor:

$$K = \frac{1}{I_{peak}T_{wide}d_{sam}\Delta\Omega} \qquad (3.2)$$

where d_{sam} is the sample thickness in cm, and $\Delta\Omega = 7.1\times10^{-7}\ ster$ is the solid angle accepted by the analyzer. [53]

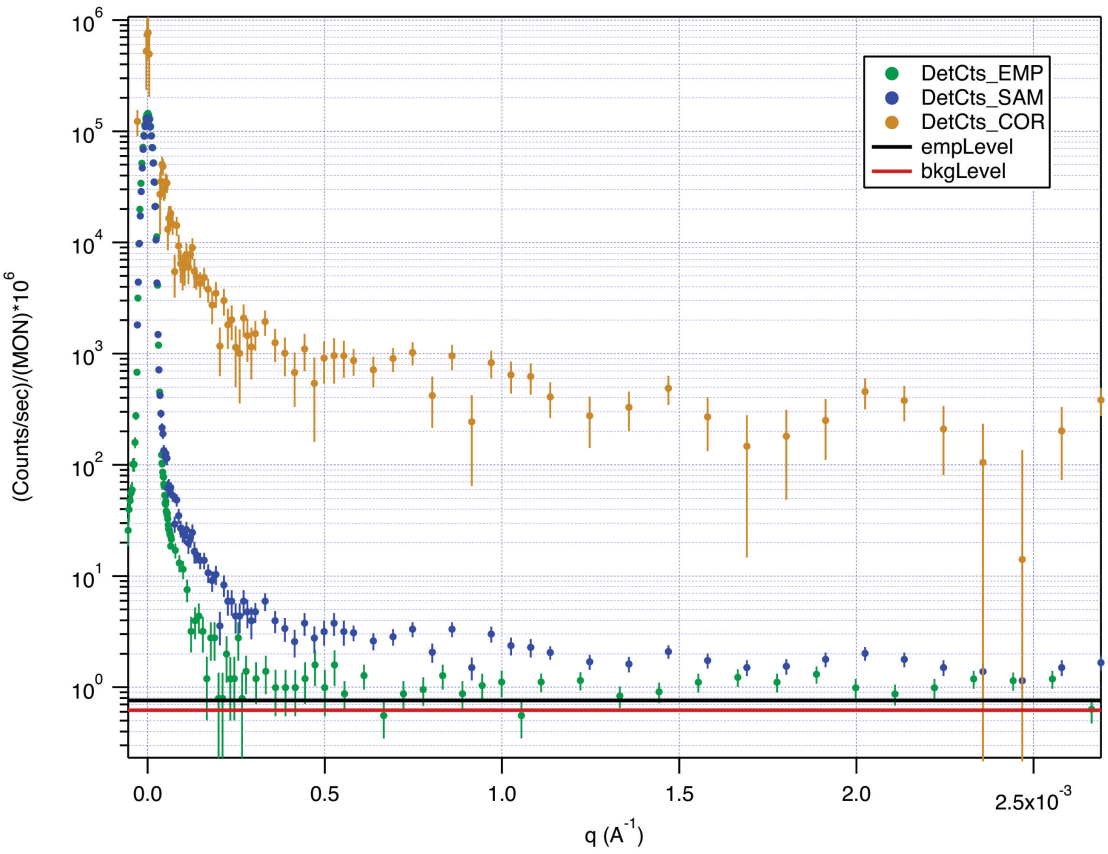

Figure 3- 4 Schematic of data correction of USANS data using IGOR MACRO written by NCNR

3.3.3 Slit smearing and de-smearing

For small-angle scattering, there is a need for extremely collimated primary beam. In order to measure extremely small angle scattering, $\theta_{s,min}$, the divergence of the beam must be smaller than $\theta_{s,min}$. Therefore, a pinhole slit is to be used, the diameter of the pinhole should be extremely small. And as a result, the flux of the scattered beam is accordingly very weak. To alleviate this problem, slit geometry has been used to collimate the beam in small angle scattering.

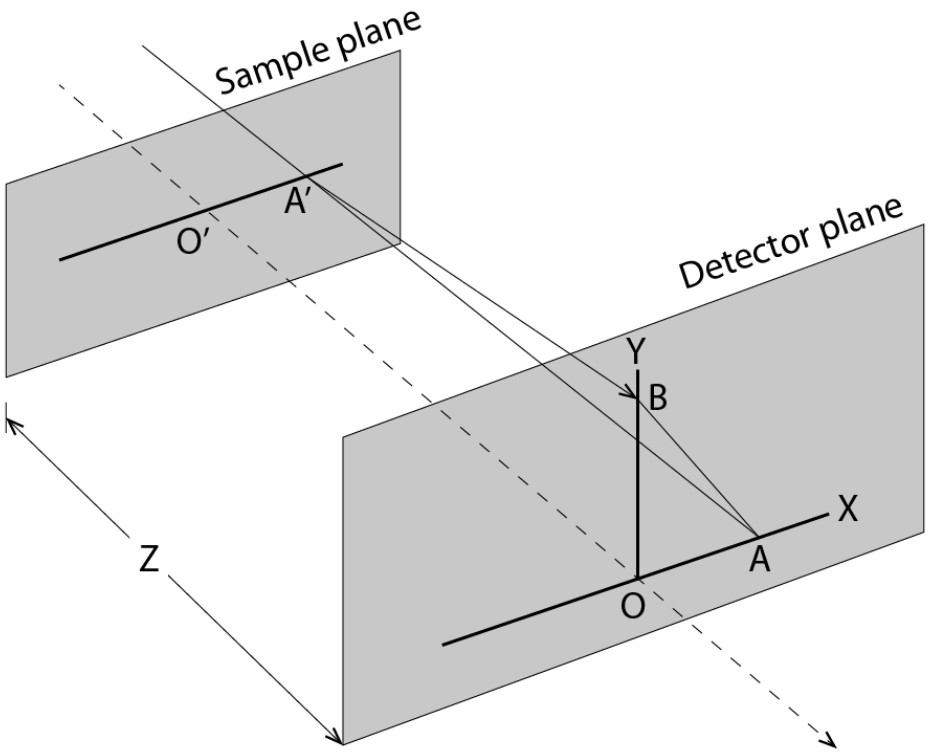

Figure 3- 5 Geometry to illustrate the slit smearing effect

However, the main drawback of using slit geometry is the introduction of slit smearing of the data. Figure 3- 5 illustrates the smearing effect due to slit geometry. The primary beam is collimated with horizontal slit whose vertical thickness is assumed to be negligibly small. Suppose a primary beam strikes sample at point A' on sample plane arrives at point A on detector plane. The direction A'A is assumed to be parallel to the direction O'O. If OA=x_1 and OB=y, then, AB=$\sqrt{x_1{}^2 + y^2}$. The contribution of the intensity measured at B by scattering from A is then

$$\delta\tilde{I}(q) = W(u)I\left(\sqrt{q^2 + u^2}\right)du \tag{3.3}$$

Here, $\tilde{I}(q)$ is the scattering measured at detector along OY axis, $W(u)$ is the normalized intensity distribution along horizontal direction in the primary beam,

$u = (2\pi/\lambda)(x_1/Z)$ is the scattering vector corresponding to the position coordinate x_1 and $q = (2\pi/\lambda)(y/Z)$.

Integrating for the whole range of u, we find

$$\tilde{I}(q) = \int_{-\infty}^{\infty} W(u) I(\sqrt{q^2 + u^2}) du \tag{3.4}$$

The primary beam proceeding towards the detector with angle u, is actually scattered at an angle $\sqrt{q^2 + u^2}$ before it is registered at an angle q. And the smeared intensity, $\tilde{I}(q)$, is the sum of the contributions from all such rays in the primary beam. Figure 3- 6 shows the smeared intensity by both the slit geometry and pinhole geometry. The effect of the slit geometry on the appearance of the measured data is much more significant than pinhole geometry. [51,53,55]

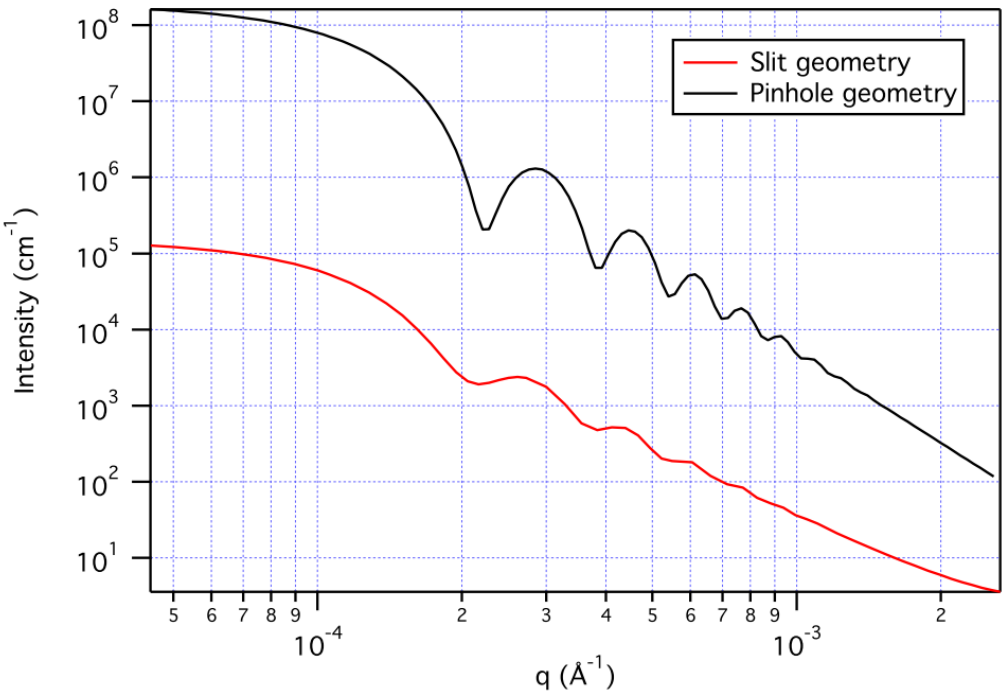

Figure 3- 6 Typical slit smear and pinhole smeared USANS graph. [53]

The scattering data were desmeared to account for the geometry of the beam using Macro software provided by National Institute Standards and Technology (NIST) center for Neutron Research (NCNR). This software implemented Lake's method for desmearing slit-smeared data and this is a direct conversion of FORTRAN code supplied by John Barker. Among the existing methods of desmearing Small Angle Scattering (SAS) data, the Lake's method is the simplest that uses iterative procedure. Further detail about Lake's method is can be found in the reference. [56]

3.3.4 Overview of SANS data reduction

For our experiment, SANS at NCNR (NIST Center for Neutron Research) was used. Incident neutron wavelength of 5Å, a sample to detector distance of 1, 4, 13m, 640mm x 640mm $_3$He 2D position sensitive detector and focusing refractive lenses provides q-ranges of the instrument from 0.008nm^{-1} to 7.0nm^{-1}. The corresponding size regime of probed structural features ranges from 1nm to 500nm. [53]

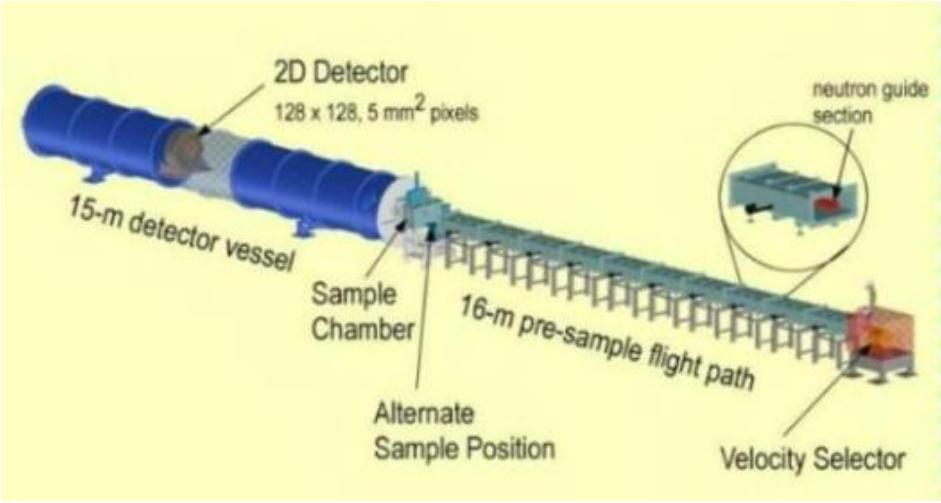

Figure 3- 7 The description of SANS, 30m long instrument on neutron guide NG7 at NCNR [53]

Figure 3- 8 illustrates the general procedure for data reduction. For initial correction, sample data should be corrected according to the following algorithm to subtract background and empty cell scattering contribution:

$$COR = (SAM - BGD) - \left[\frac{Tsam}{Temp}\right](EMP - BGD) \quad (3.5)$$

SAM: Sample data

EMP: Empty cell data

BGD: Background data

COR: Sample data after corrected for BGD and EMP

T_{sam}: Transmission of the sample

T_{emp}: Transmission of the empty cell

The next step is to correct for the non-uniformity of the detector response. The non-uniformity of the detector is measured by the scattering from a isotropic scatterer, for example, plexiglass, and it is saved as PLEX.DIV file. Subsequently, the corrected data, COR, is divided by the DIV file by pixel-by-pixel and saved to CAL folder.

As we have isotropic samples, circular averaging is applied in all the data sets used in this study. This performs averaging the intensity of the pixels on the ring with constant q value around the beam center.

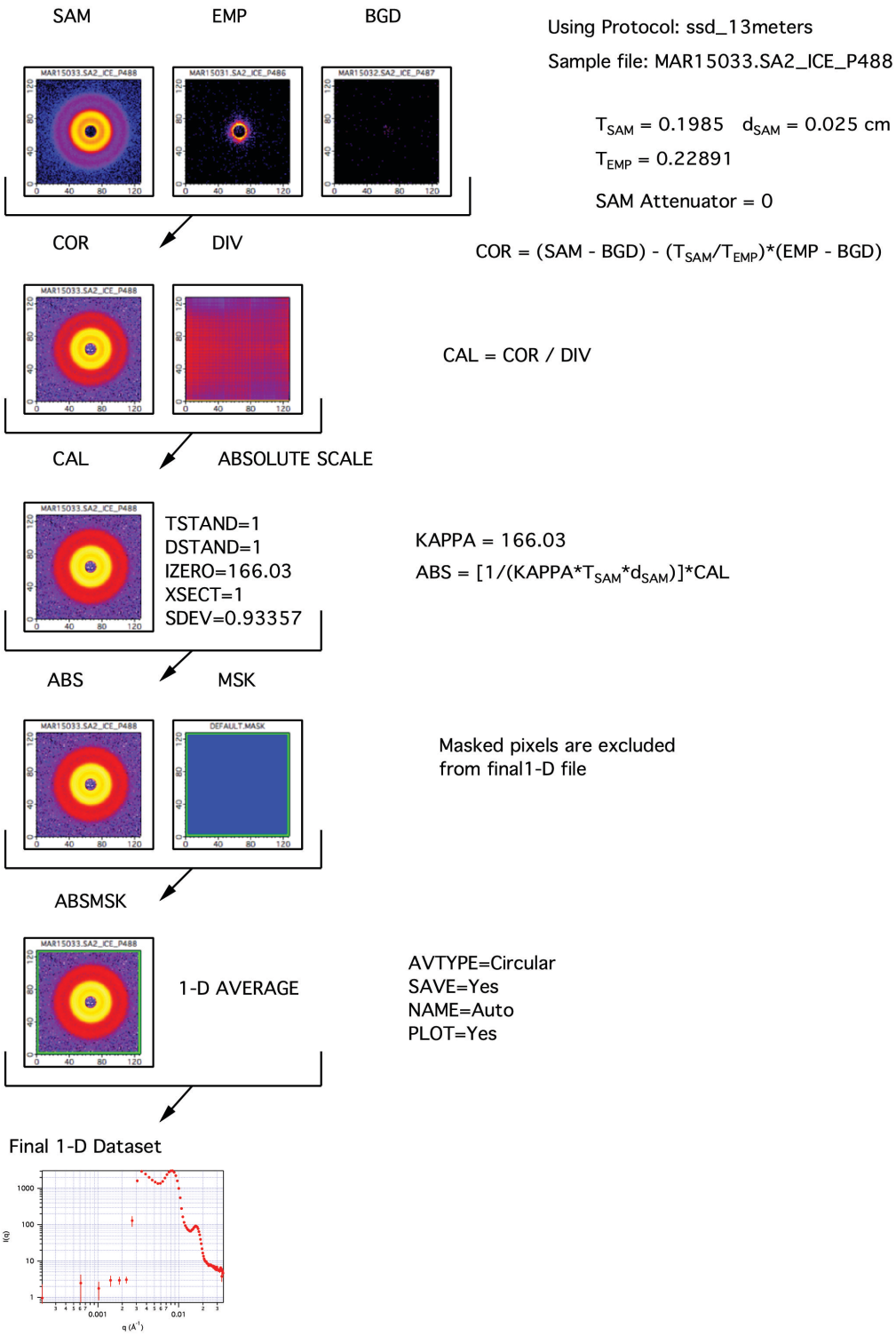

Figure 3- 8 Schematic of data reduction procedure. Data used to show the procedure is PS-PI/d-PS 10wt% annealed at 130C for 3days

The scattered intensity I(Q) produced by the averaging operation is related to the absolute cross-section $d\Sigma(Q)/d\Omega$ by the expression:

$$I(Q) = \phi_f \cdot A_s \cdot d_{sam} \cdot T_{sam} \cdot \left(\frac{d\Sigma(Q)}{d\Omega}\right) \cdot \Delta\Omega \cdot \epsilon \cdot t_s \qquad (3.6)$$

ϕ_f = flux on the sample

A_s = Sample Area

d_{sam} = Sample thickness

T_{sam} = measured sample transmission

$\Delta\Omega$ = solid angle subtended by one pixel of the detector

ε = detector efficiency, and

t_s

= effective counting time, which was renormalized to give 10^8 monitor counts (MON).

By dividing this expression for the data by a similar expression for the standard sample, ABS calculates the absolute cross-section for the data from:

$$\frac{d\Sigma(Q)}{\Delta Q} = [I(Q)MONs\ dsam\ Ts]/[Is(0)MON\ d\ T]\left[\frac{d\Sigma s(0)}{\Delta\Omega}\right] \qquad (3.7)$$

$I_s(0)$ = measured intensity of the standard sample at $Q = 0$,

d_{sam} = thickness of the standard sample and

T_{sam} = measured transmission of the standard sample

MON = monitor counts

3.3.5 Thermal concentration fluctuation

In one component system, it is the density inhomogeneity that gives rise to scattering. The density inhomogeneity in local scale is termed as radial distribution function while in larger scale is termed as thermal density fluctuation. In case of two-component system, not only the thermal density fluctuation but also the thermal concentration fluctuation gives rise to scattering. The scattering intensity due to the latter is much stronger.

For a miscible polymer blends, using "random phase approximation", deGennes derived equation giving $I(q)$.

$$\frac{V(\Delta\rho)^2}{I_t(q)} = \frac{1}{v_1\phi_1 Debye(q^2R_{g1}^2)} + \frac{1}{v_2\phi_2 Debye(q^2R_{g2}^2)} - \frac{2\chi}{v_u} \tag{3.8}$$

$$Debye(l) = \frac{2(e^{-l} + l - 1)}{l^2} \tag{3.9}$$

$$l = \left(qR_g\right)^2 \tag{3.10}$$

where R_{g1} and R_{g2} are the radii of gyration of polymer 1 and 2. Debye is the Debye function that reflects the shape of polymer molecules as Gaussian shape with modified R_g compared to unperturbed state. χ is the Flory-Huggins parameter between polymer 1 and 2 but for PS and d-PS, it is negligible. v_1, v_2 and v_u are the volume of polymer 1, 2 segment and both polymers.

In our system, the filler, d-PS, is selectively dispersed in PS domain of the matrix, and it penetrates into the brush formed by PS domain, therefore, creates thermal concentration fluctuation. Because the scattering length density contrast between d-PS and PS is high, it causes $I_t(q)$, that originates from thermal concentration fluctuation and

it dominates the scattering at $q>q_c$ where q_c is a critical value of q that is in the mid q-range.[57]

The radius of gyration, R_g, which is calculated from molecular weights of either PS domain or d-PS, was used to fit $I_t(q)$ to scattering curves for $q>q_c$. The radius of gyration is calculated from equation 3.11.

$$R_g = \sqrt{\frac{{b_k}^2 N}{6}} \tag{3.11}$$

	PS domain	d-PS filler
M_w	45,000g/mol	20,000g/mol
M_w of Kuhn monomer	720g/mol	728g/mol
Number of Kuhn monomer per polymer (N)	62.5	27.5
Kuhn Length (b_k)[58]	18Å	18Å
Radius of gyration (R_g)	~58Å	~38Å

Table 4- 1 Radius of gyration of PS and d-PS and relevant parameter for calculation[58]

The radius of gyrations of the d-PS homo-polymer and PS graft in the micro-domain structure is not identical to those in their own environment. Therefore, the radius of gyration is regarded as an adjustable parameter. For my experimental data, R_g of 38Å, which is the radius of gyration of d-PS fits the scattering curve quite well. The importance aspect of this Debye fitting has to do with the calculation of Invariant (Q). In order to apply Invariant (Q) equation for two-phase systems, there are assumptions such as a constant scattering length density within each phase. Therefore, $I_t(q)$, the scattering

from the thermal concentration fluctuation within the PS domain/d-PS should be subtracted from $I(q)$. In Appendix, they show the $I_t(q)$, Debye scattering fit to USANS/SANS scattering curves of as-cast and annealed samples. Also, the graphs also contain corrected $I(q)$ which are subtracted by $I_t(q)$ and the slope of the baseline becomes very close to -4 at high q range. The slope equal to exponent of -4 is relevant to the scattering from the surface of HAGB segregated by d-PS and the grain. There is, also surface scattering from PS-PI domain interface, however, the scattering length density contrast is lower than that of interface between d-PS decorated HAGB and grain. Also, the intensity of this Porod region is decreasing rapidly, therefore, does not contribute much to the Invariant calculation.

3.3.6 Invariant measurement

The invariant, $Q = \frac{1}{2\pi^2}\int_0^\infty q^2 I(q)dq$, is measured by integrating corrected scattered neutron intensity for whole q-rang by using SasView software. SasView is a Small Angle Scattering Analysis Software Package developed as part of the NSF DANSE project. The USANS/SANS measurement covers broad q-range, however, q does not cover the require range from 0 to ∞. Therefore, extrapolation of the data toward q=0 and q=∞ is often needed. The extrapolation toward q=0 is conducted by Guinier, power-law fit and the extrapolation towards q=∞ is conducted by power-law fit. The contribution of the extrapolation to the invariant (Q), was below 2% because of narrow q range in $q<q_{min}$ and of low intensity at high $q>q_c$.

3.4 Differential scanning calorimetry

The PerkinElmer DSC was used to measure the heat transition of the samples. In this research, as all the materials used are amorphous polymer, glass transition temperatures are measured. DSC measures the relative heat flow to the sample with a pan to that of the pan alone to keep the same temperature between them simultaneously as the equipment ramps up the temperature. Heat capacity of the polymer increases after the sample undergoes glass transition, therefore, there exists a shift in heat flow curve.

8mg of samples were put inside the Tzero Aluminum pan (TA instrument) and lid, then, press sealed by using Tzero Press. Nitrogen gas was purged during the measurement into the chamber. Each sample was measured four times to take the average value for the glass transition temperature. The heating and cooling rates were either 3°C/min or 10°C/min. The scan range of the temperature was from -80°C to 150°C to cover the glass transition temperature of all components. The procedure for the standard measurement started with lowering the temperature down to -80°C. Then the temperature was maintained for 10 minutes to achieve thermal equilibrium across the sample. Then the sample was heat to 150°C at a ramping rate of 10°C/min and 3°C/min. Then the sample was cooled back to room temperature. This procedure was repeated for 4 times to see the reproducibility. Except for the 1^{st} run of each sample, all the measurement was reproducible. 1^{st} run showed slightly distorted curve and it could rise from the solvent residue within the sample. Measurement during 2^{nd}-4^{th} run are considered in this research.

4. Comparative study of the grain structure evolution in PS-PI/d-PS blends by neutron scattering and electron microscopy

4.1 Introduction

Block copolymer (BCP)-based materials have been proposed as a platform for innovative material technologies in areas ranging from dynamic photonic sensors to solid-state ion conductors, or bulk heterojunction materials for polymer photovoltaics.[9] A common thread among many of these proposed applications is that the copolymer presents a template for 'functional fillers' and that the material performance depends on the diffusion of the filler within the copolymer host. Examples encompass the use of BCPs as solid state ion conductors where electrolytes are being added to facilitate ion transport, or the application of BCPs as tunable photonic crystals in which reversible solvent swelling enables the dynamic modulation of domain thickness and associated optical properties. Applications such as these generally benefit from the ability to fabricate large-grained microstructures with reduced defect density. If the constraints that are defined by the application prevent from the application of 'aligning fields' to drive the material in a preferred orientation then the grain size and defect density in the material will depend on the mechanism and kinetics of the coarsening process during (e.g. thermal) annealing of the microstructure. Understanding of the mechanism of grain growth and the evolution of defect structures during thermal annealing of microstructures is therefore a subject that is of fundamental relevance to both the science and engineering

of BCP materials.

The occurrence of granular microstructures and grain boundary (GB) defects is inherent in quiescent organized BCPs and can be related to the nucleation and growth of ordered grains during the structure evolution process, the superposition of stress-fields around disclinations and mechanically induced kinking, initiated e.g. by stresses during the film formation process. Early interest in GB structures stimulated the first groundbreaking studies concerning the formation of GBs in BCPs about twenty years ago [6]. However, while these studies provided intriguing insight into the organization of individual defects in BCP materials, the emphasis on ideal model systems (i.e. free of additives or impurities) presents a limitation to our current understanding of microstructure evolution in BCP-blend materials. This is because filler species can interact with defect structures and alter both the energetics and kinetics of structure evolution. In particular, prior research by our group has provided evidence of filler-GB interactions in BCP-based blend materials giving rise to segregation of fillers within grain boundary regions of the copolymer – a process that bears analogy to the aggregation of alloy atoms within defect regions in metal alloys. For example, Figure 1 illustrates the segregation of gold nanoparticle fillers into (high angle) grain boundary structures, thus giving rise to the formation of large extended aggregates that can be identified on the micrographs.

The segregation of particle fillers into grain boundary regions has motivated an ongoing research effort in our group (continuously funded by the NSF via grants DMR-0706265, 1006473, and 1410845) to understand the effect of filler addition on the grain coarsening and defect annealing in BCP microstructures. A methodology based on serial

electron imaging and image reconstruction has been developed to evaluate the evolution of microstructures across >500 μm^2 cross-sectional areas. An example of a grain map constructed from the serial imaging and reconstruction process is shown in Figure 4- 3. However, while the TEM based process has shown to be able to reveal subtle microstructural details of the microstructure two major challenges exist that limit the methodology to understand grain coarsening in BCP materials. First, the limitation of sample volume constrains the size of grains that can be evaluated. At present maximum grain size that can reliably (i.e. with adequate statistics) be analyzed is 10 μm^2. A second challenge is the required electron density contrast to image filler additives in block copolymer structures. At present this constraint limits the analysis of filler-defect interactions to inorganic particle fillers dispersed in BCP materials (such as the results shown in Figure 1). However, due to thermal degradation of particle-ligand bonds, inorganic particle fillers are not amenable to long-time annealing experiments that are required to elucidate the kinetics of filler segregation and its effect on grain size evolution. A further challenge is the extensive time needed to perform a serial imaging and reconstruction experiments that significantly limits the resolution of time-dependent studies. Small- and ultra-small angle neutron scattering (i.e. SANS and USANS) provide unique opportunities to resolve both challenges and to contribute new insights into the physics of microstructure evolution in BCP-based materials. This is because the ability to contrast fillers in neutron scattering by virtue of isotopic labeling facilitates the evaluation of small molecular (e.g. homopolymer) additives that exhibit both greater diffusivity and thermal stability. Second, the larger range of grain size dimensions in conjunction with the macroscopic size of sample volumes that is accessible via USANS

(largest dimensions that can be evaluated are in the range of 10 μm^2) enables the testing and validation of predictions made based on electron imaging analysis.

The primary purpose of the research described in this chapter is to elucidate the kinetics of filler segregation in block copolymer/homopolymer blends. To enable the in-situ analysis of grain growth during thermal annealing via neutron scattering a deuterated homopolymer is being used. It will be demonstrated that by taking advantage of the pronounced difference in the scattering length of deuterated and hydrogenated polymers it is possible to follow the formation of aggregate structures that form in grain boundary structures during thermal annealing. Small- and ultra-small angle neutron scattering in conjunction with electron imaging and grain mapping is then used to quantitatively measure the total amount of 'aggregate phase' as a function of thermal annealing conditions. A secondary objective of the research described in this chapter is to evaluate the extent to which neutron scattering provides information about the 'shape' of aggregate structures (rather than only the respective volume filling fraction). This is accomplished by a more detailed analysis of the *q*-dependence of the scattering intensity. The results are then compared to the results of the imaging-based analysis approach in order to validate the grain mapping process with independently derived information about the microstructure of the block copolymer/blend materials.

The material system in our study consists of a poly(styrene-*b*-isoprene) (PS-PI) copolymer with a weight averaged molecular weight M_w (PS block) = 45,000g/mol, M_w (PI block) = 46,000g/mol and molecular weight dispersity *PDI* = 1.07 as well as deuterated polystyrene (d-PS) filler with M_w = 20,000g/mol and molecular weight dispersity *PDI* = 1.08. This material system was chosen for several reasons: First, PS-PI

has been a widely used model system in the study of microphase separation. The Flory-Huggins interaction parameter is c = 0.00785 + 17.6/*T* and thus for the present copolymer the degree of segregation is determined as $N\chi = 57$, the copolymer is thus is the intermediate-to-strong segregation regime (*i.e.* interfaces between distinct domains can be considered to be sharp)[59]. PS-PI has been widely shown to be stable during prolonged thermal annealing (although some degree of crosslinking can occur in the presence of oxygen). PS is amorphous with a glass transition temperature of $T_{g,\,PS}$ ~ 110°C. Thus the material microstructure can readily be quenched for structural characterization by cooling to room temperature without competing effects from secondary structure formation processes (such as crystallization). In contrast, PI is rubbery at room temperature due to its low glass transition temperature ($T_{g,\,PI}$ ~ -70°C). The high mobility of PI chains at annealing temperatures above $T_{g,\,PS}$ results in rather fast structure evolution, which is beneficial to the present project since the reorganization of mesoscopic structures (such as grain boundary defects) generally occurs on longer timescales. For the reasons stated above Ryu *et al.* established the grain mapping process for the particular example of PS-PI. The results of this previous study can hence also be used as a reference to gauge the general reproducibility of the applied methodologies. Similarly, deuterated PS was chosen as filler because of its miscibility with the PS host domain (besides its high scattering length contrast to PS-PI). The interaction of hydrogenated/deuterated polymer blend systems was extensively studied by Russell and coworkers[60,61] who demonstrated that h-PS/d-PS are approximately athermal. This is also consistent with expectation since the interactions between chains in PS are dominated by dispersion interactions that are not (significantly) influenced by isotopic replacement. Note that the molecular weight of

the d-PS was chosen to be somewhat smaller than the respective molecular weight of the block copolymer host. In the absence of interactions, Winey and coworkers demonstrated that the miscibility of homopolymer fillers in block copolymer matrices strongly depends on the respective molecular weights of copolymer and homopolymer chains. According to these previous studies, miscibility is expected if the molecular weight of the added homopolymer is less than or equal to the molecular weight of the host domain ($M_{\text{d-PS}} < M_{\text{PS}}$).

The structure of this chapter is as follows: first, the miscibility of the PS-PI/d-PS blend across the relevant compositional range will be confirmed by differential scanning calorimetry, and the lamellar microstructure of blend samples during thermal annealing will be confirmed by small angle neutron scattering (section 4.2). Subsequently, the evolution of grain microstructures during thermal annealing as well as the evolution of relevant grain boundary characteristics during thermal annealing will be presented (section 4.3). The microstructural features obtained from electron imaging will be compared to small- and ultra-small angle scattering in section 4.4 where a process will be introduced that enables the quantitative determination of the concentration of filler in grain boundary regions. The development of this methodology is seen as a major accomplishment of this research project.

4.2 Microphase Separation in PS-PI/d-PS Blend Systems

In order to characterize the dissolution of the filler in block copolymer, DSC measurement was done on PS-PI (powder), d-PS (powder) and PS-PI/d-PS blend (film) samples. The temperature range was between -80°C to ~130°C and the heat flow was

measured during heating. The ramping rate was 10°C/min and the 3rd run was plot in the graph. It is observed that the T_g of PI domain stays same after mixing with d-PS, and this means that d-PS is not blended with PI domain. If the all the d-PS had mixed with PI domain, the T_g of PI domain should have increased to -50°C according to the Fox equation. Fox equation predicts the glass transition temperature of in (miscible) polymer blends:

$$\frac{1}{T_g} = \frac{w_1}{T_{g,1}} + \frac{w_2}{T_{g,2}} \tag{4.1}$$

w_1 is the weight fraction of 1st component

w_2 is the weight fraction of 2nd component

$T_{g,1}$ is the glass transition temperature of the 1st component

$T_{g,2}$ is the glass transition temperature of the 2nd component

T_g is the glass transition temperature of the blend

The T_g of PS domain, on the other hand, decreases from 107.41°C to 104.61°C after mixing. The fox equation predicts the T_g of PS domain to decrease from 107.41°C to 105.12°C and this is only ~0.5°C higher than the experimental value. This good agreement supports that d-PS is blended with PS domain in the matrix.

Therefore, based on the DSC measurement, it is concluded that the d-PS is blended with PS domain of the block copolymer.

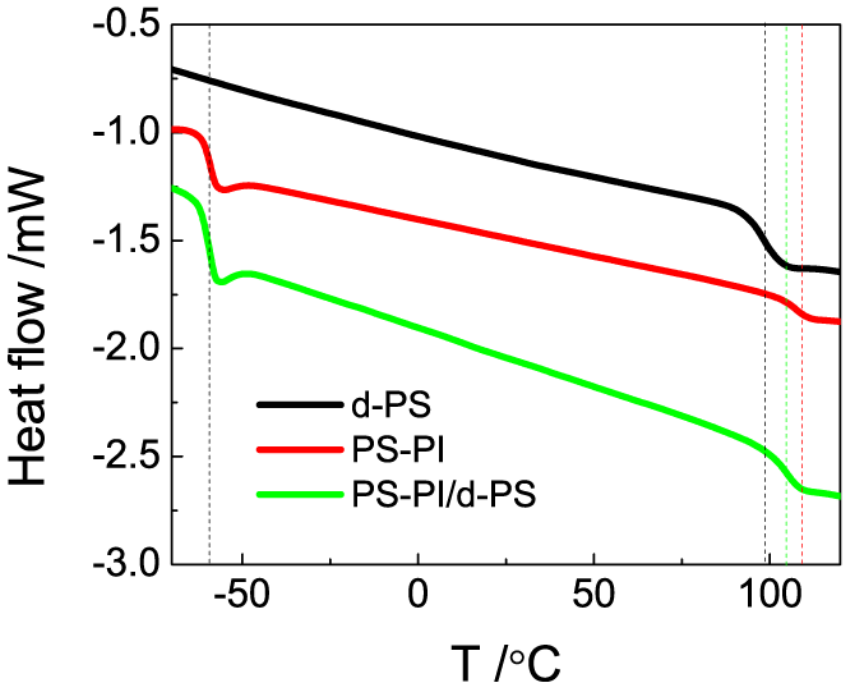

Figure 4- 1 DSC graphs of PS-PI/d-PS 10wt% as-cast film, d-PS powder and PS-PI powder. The ramping rate was 10°C/min (heating).

Sample	T_g of PI domain	T_g of PS domain
d-PS	-	95.27°C
PS-PI	-59.06°C	107.41°C
PS-PI/d-PS 10wt%	-59.10°C	104.61°C

Table 4- 2 Glass transition temperature of PS-PI/d-PS blend, pristine PS-PI and d-PS.

In order to confirm the lamellae microstructure, the ratio of peak positions (*q2*,*q3*,..) to the primary peak, q^*, of the SANS was measured. The d-PS is blended with PS-PI to study the kinetics of filler segregation to grain boundary of lamellae microstructure. Therefore, the addition of d-PS to PS-PI with symmetric composition

should not change the microstructure of the blend. As shown in Figure 4- 2, the peak positions of the SANS were at q values that is q^* multiplied by integer number (q/q^*=1,2,3,…). As-cast sample showed q^* at 0.00995Å^{-1}, and $q2/q^*$=1.93. 3hr-annealed sample showed q^* at 0.0089Å^{-1}, $q2/q^*$=1.97 and $q3/q^*$=3.11. 24hr-annealed sample showed q^* at 0.0088Å^{-1}, $q2/q^*$=1.95 and $q3/q^*$=3.10. 72hr-annealed sample showed q^* at 0.00851Å^{-1} and $q2/q^*$=2.02. 168hr-annealed sample showed q^* at 0.00765Å^{-1} and $q2/q^*$=1.98.

The consistent scaling of higher order peaks as integer multiples of the first reflection conforms the presence of a lamellar microstructure in all systems and confirms the absence of order-order transitions during the thermal annealing process.

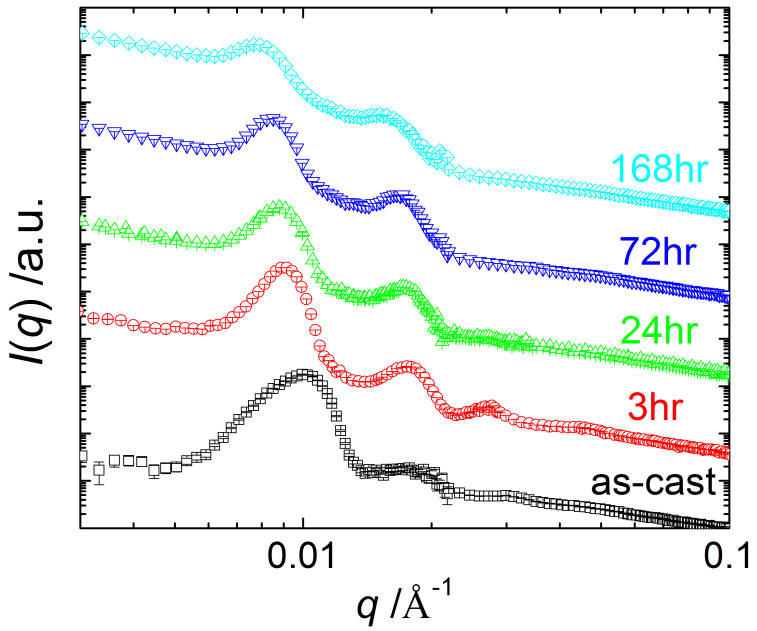

Figure 4- 2 SANS graph of PS-PI/d-PS 10wt% as a function of thermal annealing time

4.3 Grain map analysis

Microstructural information about the as cast and annealed samples were obtained by grain map analysis. The grain mapping enables us to obtain physical parameters such as average grain size, grain size distribution, grain shape, mis-orientation of symmetric tilt grain boundaries, density of grain boundary, volume fraction of high angle grain boundary and relative grain boundary energy as a function of tilt angle. The procedure conducted in grain mapping involves large area electron imaging, reconstruction of the images and image analysis and it is explained in background section.

The grain map of 3 day thermally annealed sample is shown in Figure 4- 3. In the grain map, based on the orientation of the lamellae within the grain, grains are drawn with different colors. The selection of color to fill the grain is randomly chosen. The boundary between the different color grains is the grain boundary. The complete set of grain map is available in Appendix. The grain map is overlaid with high angle grain boundary ($\theta>60°$) map (thick black lines). Ryu et al. have report that fillers preferentially segregate to high angle grain boundary and I have also observed the same in PS-PI/d-PS system.[50] More details about the importance of high angle grain boundary in filled system will be shown in later chapter. The grain map is rotated to fit the page. X-axis is the direction parallel to interfaces to sample/air and sample/substrate. And Y-axis is the direction perpendicular to both interfaces.

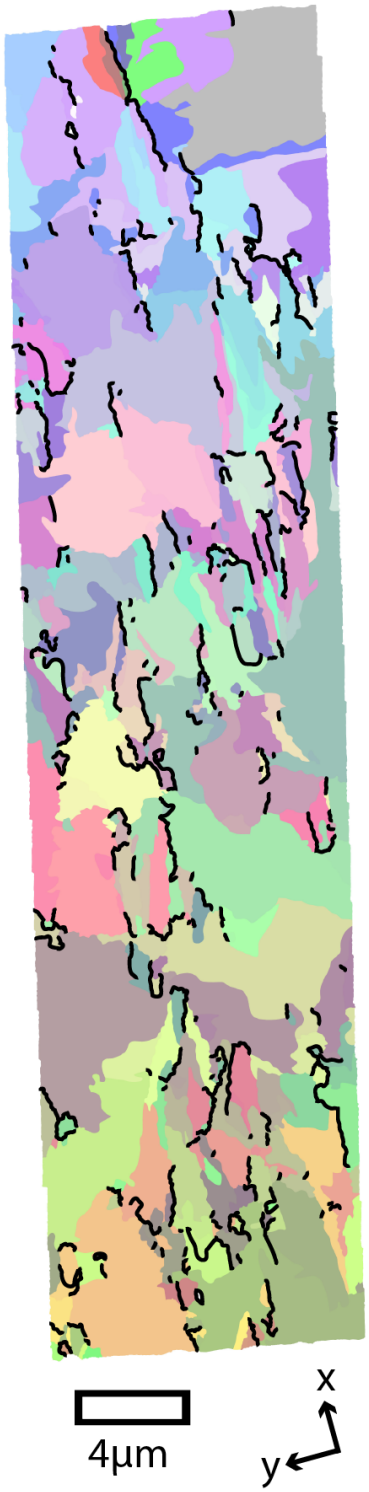

Figure 4- 3 Grain map of PS-PI/d-PS 10wt% thermally annealed at 130°C for 3 days overlaid with high angle grain boundary map. x and y axis denote in-plane and out-of-plane axis

The grain maps show a distinctive alignment of high angle boundaries parallel to the film plan (y, z). This is consistent with previous reports by Ryu et al. who concluded the orientation to be a consequence of the presence of 'aligning fields' that emerge during the late stages of solvent annealing. **Figure 4- 4** shows the evolution of the number weighted grain area as a function of thermal annealing. In agreement with expectation, grain size is seen to increase with a scaling coefficient ($\langle A \rangle \sim t^x$) where $x \sim$. Note that grain size is found to level off at annealing times longer than 3 days. This stagnation of grain growth has also been observed in previous experiments (by Ryu and coworkers) who investigated the grain size evolution of block copolymers in the presence of fillers. It was proposed that grain stagnation is a consequence of pinning effects due to filler segregation. It will be a major goal of this thesis to quantify the time scales of filler segregation and also to determine the equilibrium filler concentration in grain boundary defects.

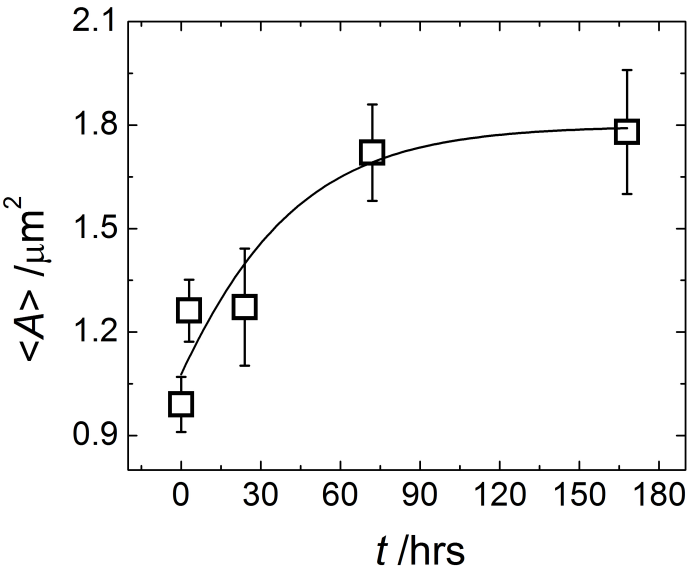

Figure 4- 4 Number average grain area of PS-PI/d-PS 10wt% as a function of thermal annealing time

Thermal Annealing time (hrs)	Number average Grain size (μm^2)	Weighted average Grain size (μm^2)
0	0.99	5.43
3	1.26	3.59
24	1.27	9.81
72	1.72	11.62
168	1.78	9.90

Table 4- 3 The Number average and weighted average grain size

4.3.1 Grain size distribution

The grain size distribution was determined by analysis of constructed grain map. The grain size distributions of as-cast and annealed samples are plotted in Figure 4-9 with respect to lognormal distribution. The lognormal distribution is the probability density plot that the logarithm of the variable follows normal distribution. The lognormal distribution has probability density function as follow:

$$\frac{1}{\sigma A\sqrt{2\pi}}\exp\left(-\frac{(ln(A)-\mu)^2}{2\sigma^2}\right) \tag{4.2}$$

where A is the variable (grain size in our case), μ is the shape scale parameter and σ (> 0) is the scale parameter. In the lognormal probability plot, the experimental data are plotted along with the theoretical expectation shown as red line. In order to remove the artifacts from the image processing, grains smaller than 0.03μm^2 are not considered. And in order to statistically reliable grains larger than 10μm^2 are not considered because of the limited sampling number. The size range of the grain considered is filled with blue color. For

both the as-cast and annealed samples, the experimental grain size distribution follows theoretical lognormal distribution approximately.

The grain size distribution has been used to analyze the mechanism of grain growth in inorganic materials. There are two different mechanism of grain growth. One is normal grain growth where grains are uniformly coarsening so that grain size increases without altering the grain size distribution. The other is abnormal grain growth where a few grains grow larger in expense of smaller grains and becomes abnormally large and as a result, the grain size distribution shows bimodal distribution. The grain size distribution of as-cast and annealed samples show similar lognormal distribution, therefore, we can conclude that normal grain growth is taking place in grain evolution of PS-PI/d-PS system during thermal annealing.

	Shape scale (μ)	Scale (σ)
0TA	-1.15487	1.47147
3hr	-0.59279	1.38295
24hr	-1.02326	1.146849
72hr (3day)	-0.37551	1.36532
168hr (7day)	-0.39963	1.41704

Table 4- 4 Lognormal distribution parameters for PS-PI/d-PS as-cast and thermally annually samples

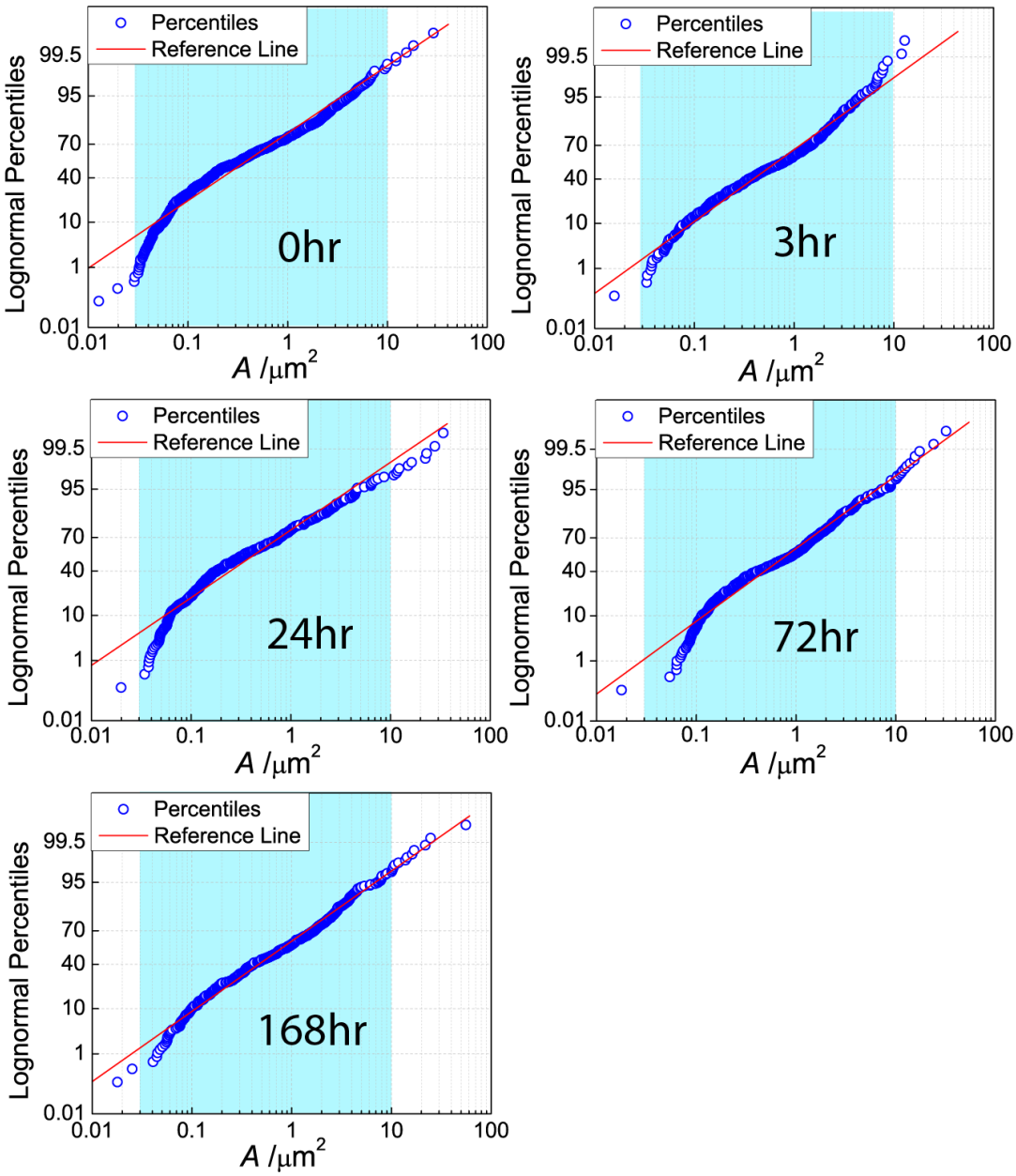

Figure 4- 5 lognormal probability plots of PS-PI/d-PS 10wt% 0hr (as-cast), 3hr, 24hr, 72hr (3day) and 168hr (7day) thermally annealed samples. Reference lines correspond to theoretical lognormal distributions. Highlighted in blue is grain size range that is considered for calculation of average.

4.3.2 Grain shape

The grain shape was characterized by the aspect ratio of the grains determined from the ratio of length of the major and minor axes. **Figure 4- 6** shows that the average aspect ratio of the as-cast and annealed sample. The average aspect ratio is determined from the median aspect ratio of all the grains. The average aspect ratios measured are 2.60 (as-cast), 2.08 (3hr), 2.80 (24hr), 2.31 (72hr) and 2.23 (168hr). There is some deviation in the early annealing period, but in general the average aspect ratio decreases slowly with the thermal annealing. The measured values are in agreement with previous observation of BCP grain growth that supports that grain formation in BCP melt is governed by nucleation and growth mechanism.[62] The anisotropic shape of grain when BCP is cooled below order-disorder transition (ODT) temperature was observed by depolarized light scattering, SAXS, TEM and polarized optical microscopy (POM). [22,62–69] They have reported aspect ratio of grains that are close to our values. The anisotropy shape of grain was attributed to the anisotropy in surface tension. While the lamellae edges have similar surface energy with the surrounding disordered phases, lamellae planes have unfavorable interface tension with the surrounding, therefore, the grains tend to grow in direction parallel to lamellar normal. The observation that similar aspect ratio of grains are observed in solution cast BCP, suggests that PS-PI/d-PS also undergoes nucleation and growth mechanism during initial micro-phase separation and maintains the shape in the solid state. With thermal annealing, the grains are turning into more isotropic shape with slightly reduced average aspect ratio. This is attributed to the driving force of the system that wants to decrease the interfacial area by reducing the surface area of the grains.

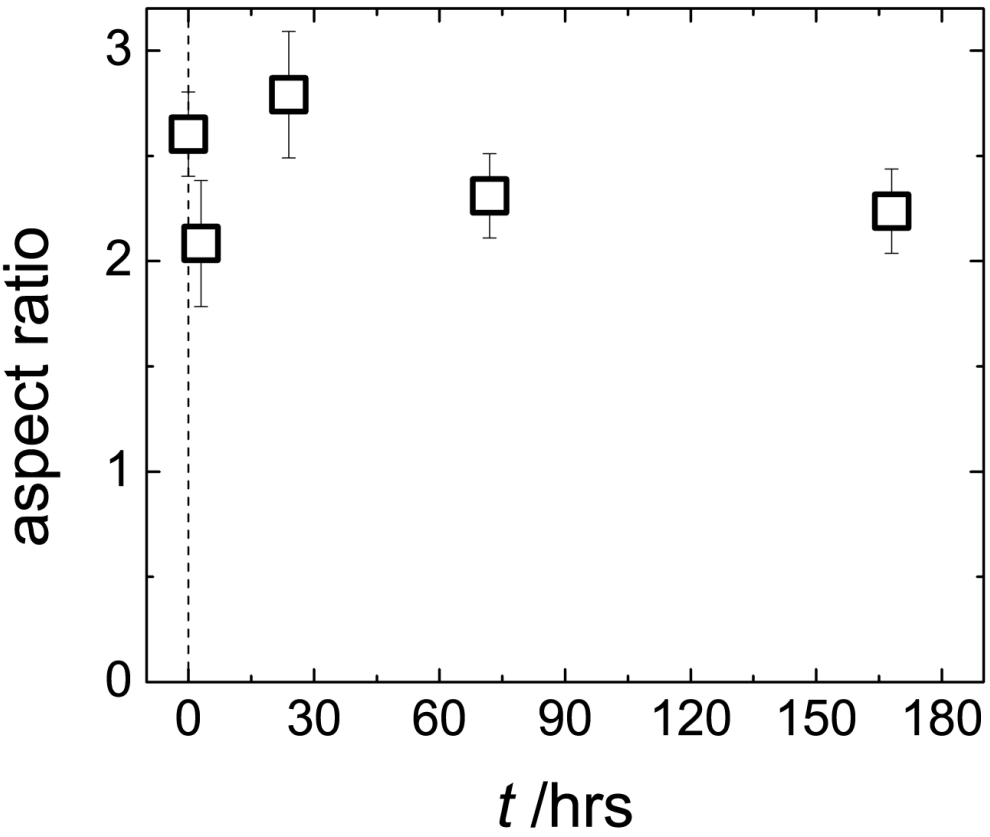

Figure 4- 6 Average aspect ratio of grain shape of PS-PI/d-PS 10wt% as-cast and annealed samples

4.3.3 Misorientation of symmetric tilt grain boundaries

Analysis of the type and frequency of high grain boundary types reveals that the large majority belongs to the group of symmetric tilt boundaries. The asymmetric grain boundary (T-junction) comprise only minor portion of the grain boundary population. Similar observation was reported by Ryu et al.[41] It was concluded that the origin of high angle boundaries is due to stress formation during the late states of solvent evaporation (where stresses are expected to arise in the film plane direction due to the interference of

film pinning and adherence to the substrate). This hypothesis is also supported by the preferred orientation of HAGBs in the substrate direction.

Figure 4- 7 shows the relative frequency of mis-orientation angles of grain boundary of as-cast and annealed samples. The overall trend of the frequency in the plot shows that the population of grain boundaries decrease with tilt angle. However, for as-cast and 3hr thermally annealed samples, there is a frequency peak at high angle grain boundary (θ~140°) even though it is the high-energy grain boundary.[35,39,40] With thermal annealing, the frequency of high angle grain boundary rapidly decreases until 24hr of thermal annealing. Thermal annealing more than 24hrs only slightly changes the frequency of high angle grain boundary.

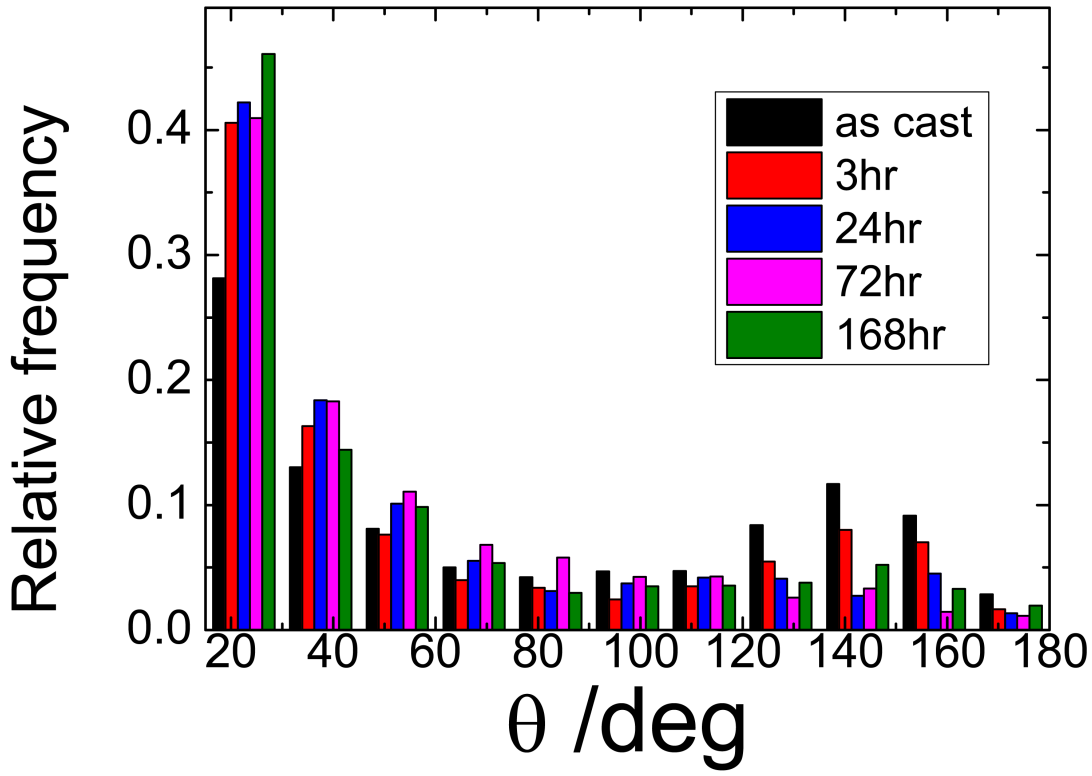

Figure 4- 7 Relative frequency of mis-orientation angle of PS-PI/d-PS 10wt% 0hr, 3hr, 24hr, 72hr (3day) and 168hr (7day) at 130°C

We can conclude that the driving force of grain coarsening is the annealing of high angle grain boundary and the driving force decreases after 24hr of thermal annealing. It is worthwhile to compare the change of relative frequency of high angle grain boundary during thermal annealing with the kinetics of filler segregation which will be shown later in this chapter.

4.3.4 High Angle Grain Boundary (HAGB) structure

The definition of high angle grain boundary (HAGB) in our study is the threshold angle of the symmetric tilt grain boundary above which filler segregates. As the d-PS is not distinguishable from PS-PI matrix, we have alternatively blended PS functionalized gold nanoparticle (AuNP) to PS-PI and observed the nanoparticle aggregate density as a function of tilt angle. Ryu et al. have previously reported that the number of AuNP aggregates as a function of grain boundary's tilt angle has a threshold angle that above which particles starts to segregate to grain boundary. They reported that above the threshold angle, the number of AuNP aggregate as a function of tilt angle was approximately constant if we consider the error bar. [50]

In this study, PS-PI (45k-46k) is blended with 10wt% PS grafted gold nanoparticle. PS-grafted gold nanoparticle is synthesized following procedures from literature.[70,71] The average diameter of the AuPS is ~3nm and the surface is functionalized with polystyrene (M_w=11.5kg/mol). The solution is rapidly casted under rotovapor environment and annealed at 130°C for 3 days. Then, the sample is cryo-microtomed for TEM imaging. Depending on the tilt angle of grain boundary, gold

nanoparticle aggregates were observed. In order to quantify this observation, the aggregate particle density is measured and plotted as a function of tilt angle of the grain boundary in Figure 4- 8. It shows that the particle density has a threshold angle of about 54°, and above which it stays nearly constant. The inset shows grain boundaries (shown with dashed lines) with different tilt angle. Grain boundary with tilt angle of 36° is not segregated by particles while the grain boundary with tilt angle of 120° is segregated by particles.

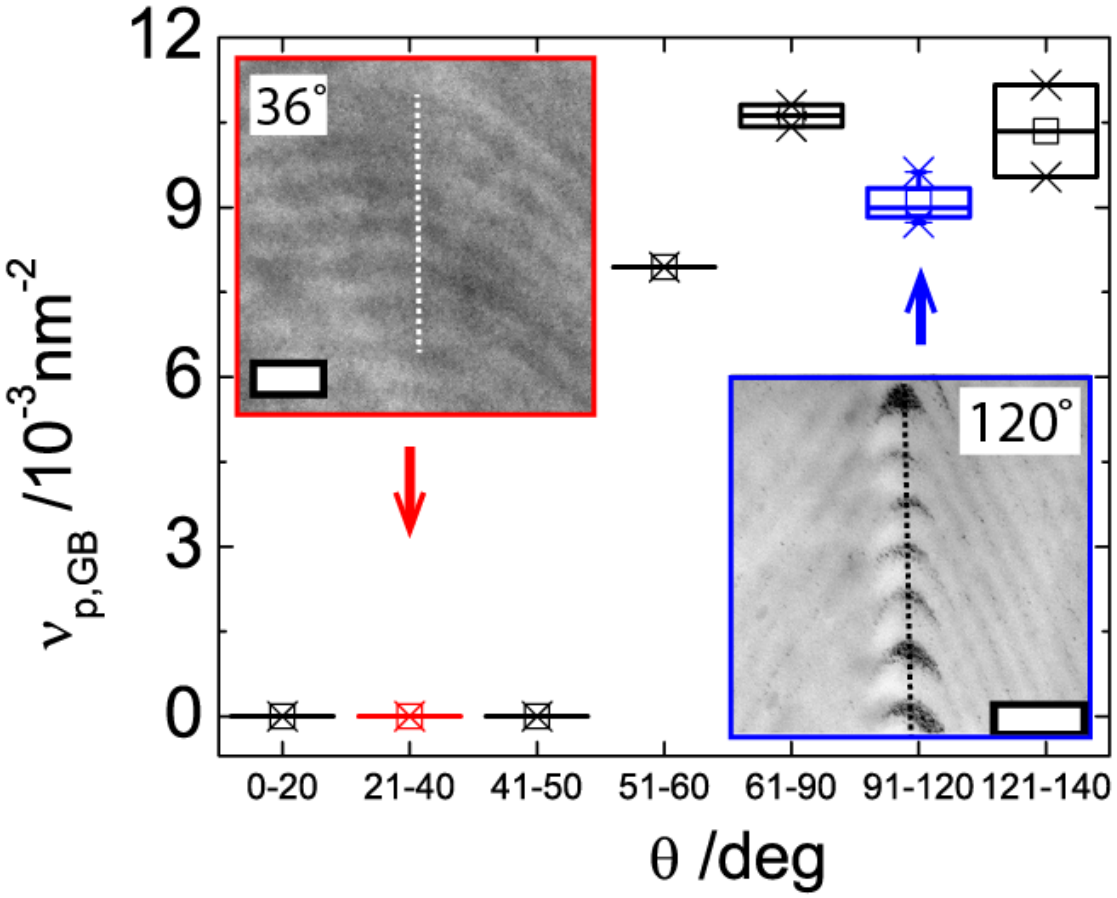

Figure 4- 8 Dependence of the gold nanoparticle aggregate density within HAGB as a function of PS-PI/AuNP blends thermally annealed for 3 days at 130°C. (inset) (red) AuNP are not segregated within low tilt angle grain boundary (36°), however, (blue) AuNP are segregated within high angle tilt grain boundary (120°)

We can conclude that based on PS-PI/AuNP study, grain boundary with tilt angle exceeding ~60° attracts fillers to segregates within and the density of filler in grain boundary stays almost constant above the threshold angle. This supports our assumption in later chapter that the scattering length density (SLD) of HAGB segregated by d-PS is not a function of tilt angle, but stays constant above the threshold angle. Therefore, in ultra-small q region of USANS, our material can be assumed as two-phase system. The detail of information of the two-phase system will be shown in later slides.

4.3.5 Grain boundary width

At the grain boundary, the local distribution is perturbed within a region of width W. The measurement of grain boundary width is important because we need to calculate the volume of high angle grain boundary. The inset of Figure 4- 9 shows the schematic diagram of chevron tilt boundary. θ is the tilt angle of the grain boundary and it is measured by the angle between two lamellae normal. L is the lamellae long period and increases to $L/\cos(\theta/2)$ at the center of the boundary. R is the curvature radius related to the observed boundary width by geometrical formula $R=W/2\ \sin(\theta/2)$. The inset shows the detail of the measurement of W, R, L and θ from TEM image. The measurement was done using ImageJ software.

Figure 4- 9shows that the measured width of grain boundary, W, of pristine PS-PI as cast sample, divided by the length of lamellae repeat unit, L. The plot shows that W/L does not significantly change with respect to the tilt angle but rather is about equal to the lamellar period across all misorientation that were investigated. This is in agreement with the literature[28], and we can assume that the grain boundary width is equal to the length of lamellae repeat unit, L (~72nm).

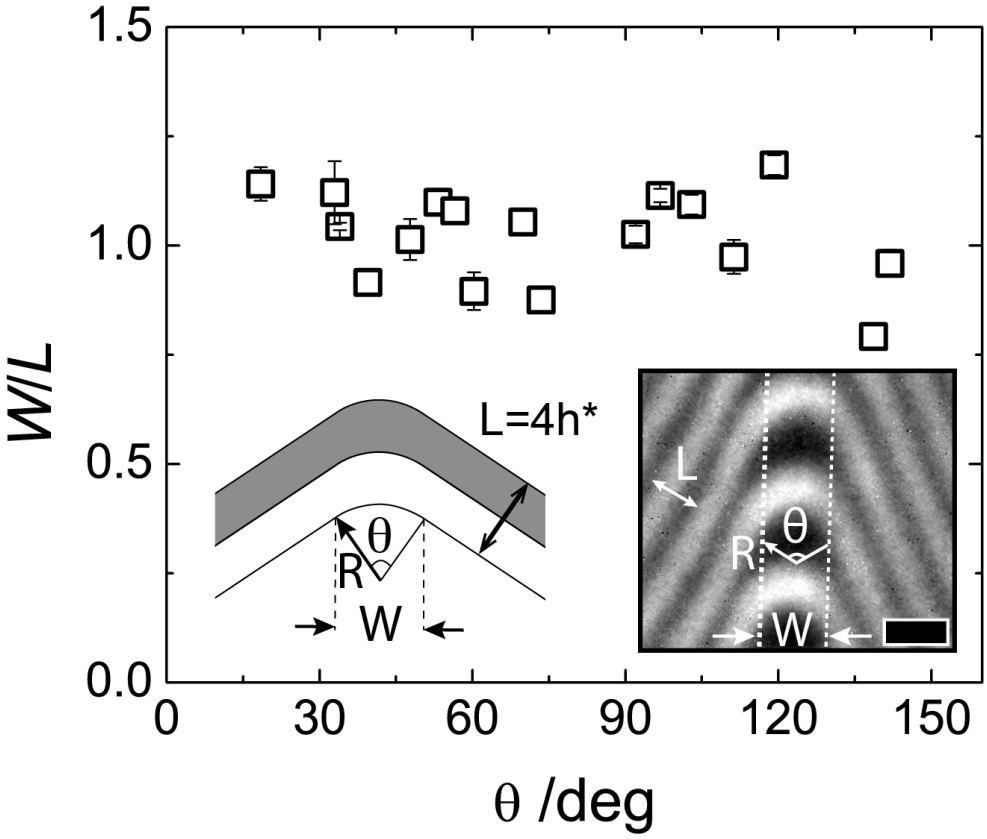

Figure 4- 9 Grain boundary width to lamellar spacing ratio as a function of tilt angle. (inset) Scheme that shows the details illustration of grain boundary width, radius of curvature

4.3.6 Volume fraction of HAGB

From the grain map, the length of the HAGB divided by the whole grain area, L_A, can be acquired. Multiplying L_A by the thickness of grain boundary (~72nm) gives the area fraction of the HAGB, A_A. However, the grain boundary is 3-d structure, therefore, we need to use the quantitative stereology to relate two-dimensional projection to three-dimensional space. The total area of the each sample contains at least ~400 grains, which makes our quantitative stereology more statistically significant. For the internal surfaces such as grain boundaries, interface between particles and matrix, the following equation

relates surface area per volume, S_V, length of linear elements per area, L_V and number of point intersections per unit length of line, P_L.

$$S_V = (4/\pi)L_A = 2P_L \tag{4.3}$$

And as the grain boundary has thickness that is comparable to length of one lamellar repeat unit, L_0, volume fraction of grain boundary, V_V, is obtained by following equation:

$$V_V = S_V \cdot L_0 \tag{4.4}$$

Figure 4- 10 shows the plot of A_A, V_V as a function of thermal annealing time. Both the volume fraction and area fraction of high angle grain boundary decreases rapidly in the early annealing and then saturates after 72 hrs of thermal annealing.

Table 4- 5 shows the number of grains in the grain map, area fraction of HAGB and volume fraction of HAGB of as-cast and annealed PS-PI/d-PS samples.

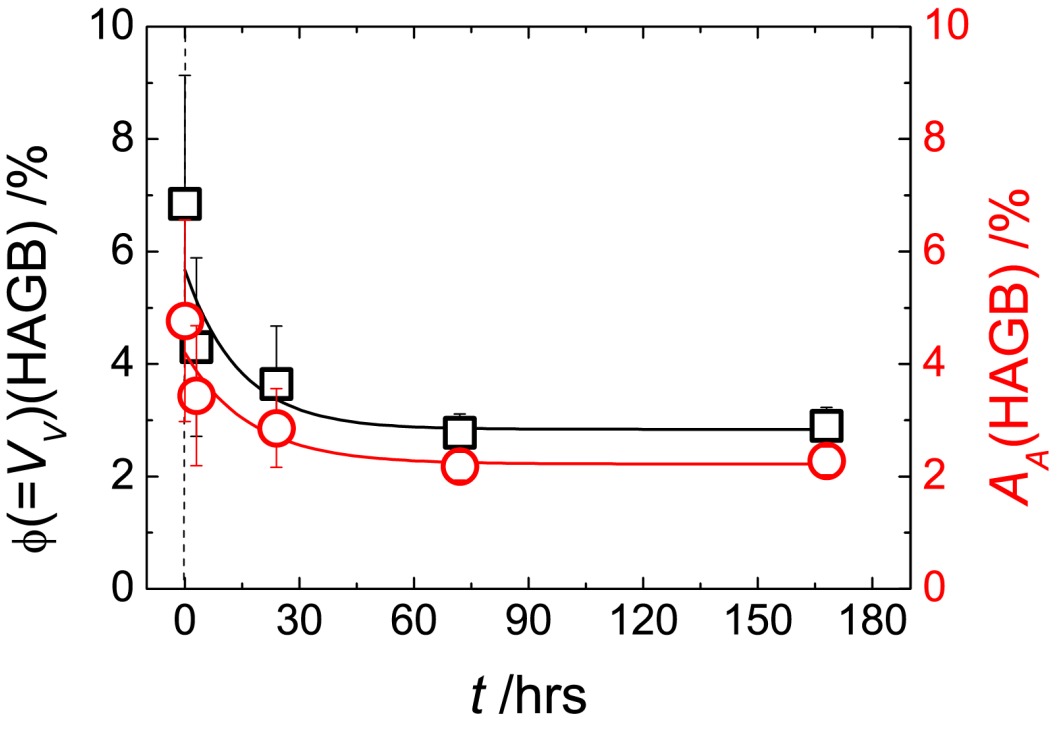

Figure 4- 10 High angle grain boundary volume percent and area percent of PS-PI/d-PS 10wt% as a function of thermal annealing time

	as-cast	3hr	24hr	72hr	168hr
Number of total grains	659	402	394	462	431
A_A (%)	4.7	3.5	2.9	2.2	2.3
V_V (%)	6.8	4.3	3.6	2.8	2.9

Table 4- 5 total number of grains, area /volume percent of high angle grain boundary of PS-PI/d-PS 10wt% as cast and annealed samples

4.3.7 Relative grain boundary energy

In order to explore the effect of thermal annealing of filled block copolymer system on the relative grain boundary energy, relative grain boundary energy as a function of tilt angle was constructed by triple junction analysis mentioned in the background section. The relative energy of the grain boundary depending on the tilt angle for 3 representative samples is plotted in Figure 4- 11. The plot of 24hr, 72hr and 168hr annealed samples almost completely overlaps, therefore, only plotted 168hr annealed sample. θ~40° is used as the critical tilt angle and the grain boundary energy at this angle is set to 1. The grain boundary with smaller tilt angle than the critical angle shows minor undulations and could interfere with accurate measurement of dihedral angle. As the critical angle is below the threshold angle for filler segregation (~60°), both the grain boundary of as-cast and annealed sample are not segregated by fillers. Therefore, the grain boundary energies of the critical tilt angle of as-cast and annealed samples are same and used as calibration. The grain boundary energy is dependent on mis-orientation angle and shows higher energy for higher angle. This is attributed to the chain conformation

energy that increases with tilt angle. When compared to as-cast sample, annealed samples shows early leveling-off angle in the relative energy plot. The early leveling-off of grain

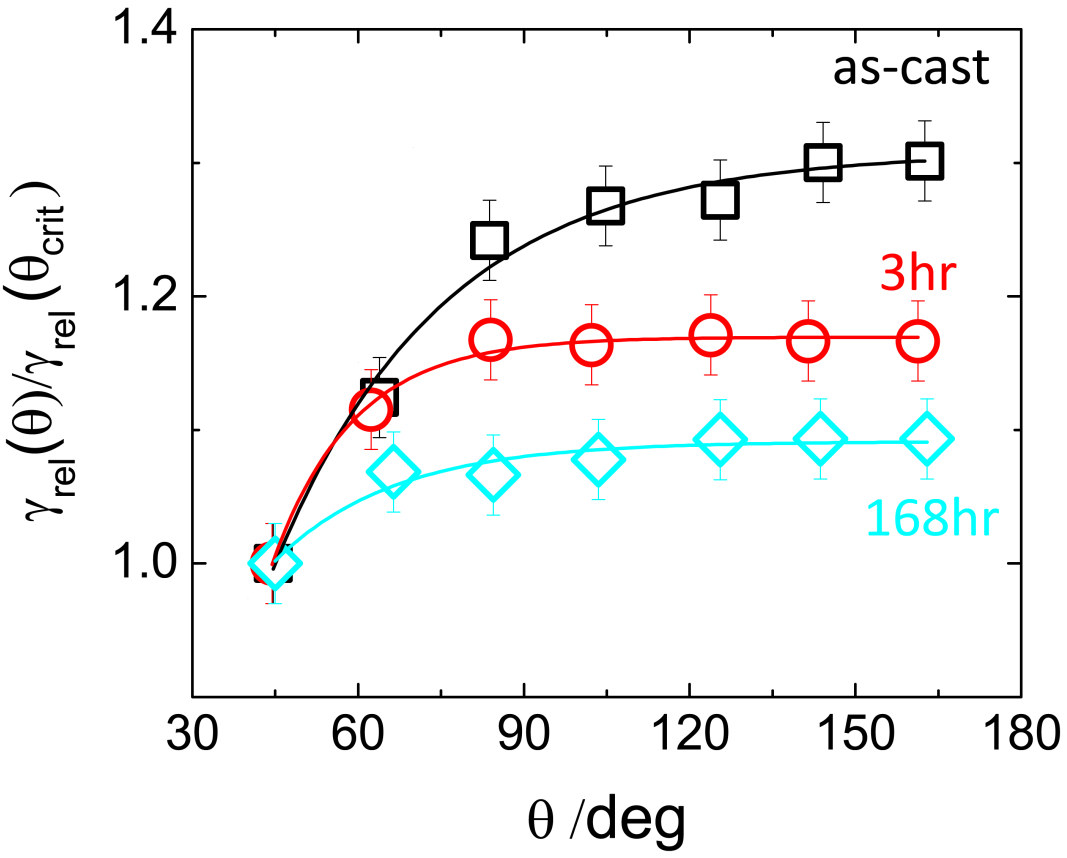

Figure 4- 11 Normalized relative grain boundary energy of PS-PI/d-PS 10wt% as-cast and two annealed samples (3hr, 168hr). Other annealed samples (24hr, 72hr) samples are omitted because those the curves almost completely overlap with 168hr sample.

boundary implies that the filler stabilizes the formation of Omega GBs in lower tilt angles. Also the graph shows that the energy of the HAGB is lower in annealed samples. This result supports our assumption that filler segregates to high angle grain boundary, and as a result, stabilizes the grain boundary energy.

Figure 4- 12 shows relevant triple junction arrangements of before and after filler segregation to grain boundary. The tilt angles of the grain boundaries intersecting at the triple junction are the same in left and right scheme. As θ_1 is bigger than θ_2 and θ_3, the corresponding σ_1, is greater than σ_2 and σ_3. In order to minimize the system energy, the dihedral angles of the corresponding grain boundary satisfies $\xi_1 < \xi_2 = \xi_3$. However, after filler segregation to the grain boundary with tilt angle θ_1, the grain boundary tension σ_1' decreases from σ_1. Therefore, the corresponding ξ_1' becomes bigger than ξ_1, and as a results, reflected in the Young's equation analysis as a lower HAGB energy.

We can conclude that thermal annealing filler block copolymer stabilizes the high angle grain boundary energy. And after 24hr hours of thermal annealing, the relative energy plot becomes saturated.

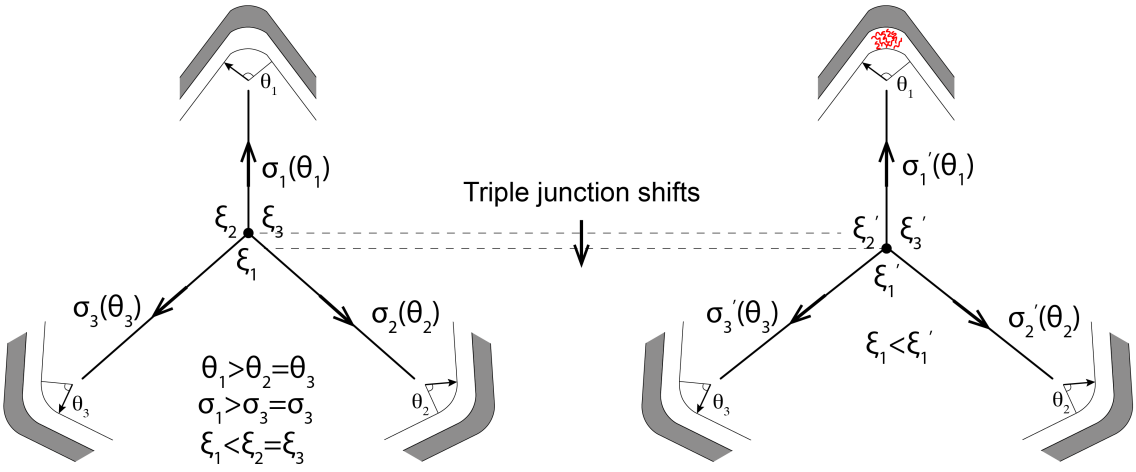

Figure 4- 12 triple junction arrangement (left) before and (right) after filler segregation to grain boundary

4.4 Neutron Scattering

As the filler has much higher scattering length density (*SLD*) than PS-PI matrix, the neutron scattering is greatly affected by the distribution of d-PS in PS-PI matrix. As shown in **Figure 4- 13**, in as-cast sample, d-PS is uniformly mixed within PS domain of the matrix. There is SLD contrast between PS and PI lamellae domain, however, no contrast between grain boundary and the grain. With the thermal annealing above glass transition temperature of both domain, the d-PS diffuses to grain boundary in order to reduce the total free energy. The d-PS shown as red spheres move to grain boundary, and as a result, the grain boundary is decorated by high concentration of d-PS. As d-PS has much higher *SLD* than the PS-PI matrix, the scattering length density has large contrast between the grain boundary and the rest of the grain. With this view, the system can approximately be represented as a two-phase region. One phase is the grain boundary decorated by filler and the other phase is the rest of the grain.

Ultra-small Angle Neutron Scattering and Small Angle Neutron Scattering was performed. The size regime of USANS ranges from 100nm to 20μm and that matches the length scale of grain characteristics. **Figure 4- 14** shows the scheme that illustrates the representative neutron scattering from PS-PI/d-PS 10wt% as cast and annealed sample. The figure illustrates the relevant structures (grain, lamellae) for both USANS and SANS *q* range. There is significant increase in intensity within USANS and this is relevant with the distribution of filler that creates *SLD* contrast in micrometer scale structure. Further detail will be shown later.

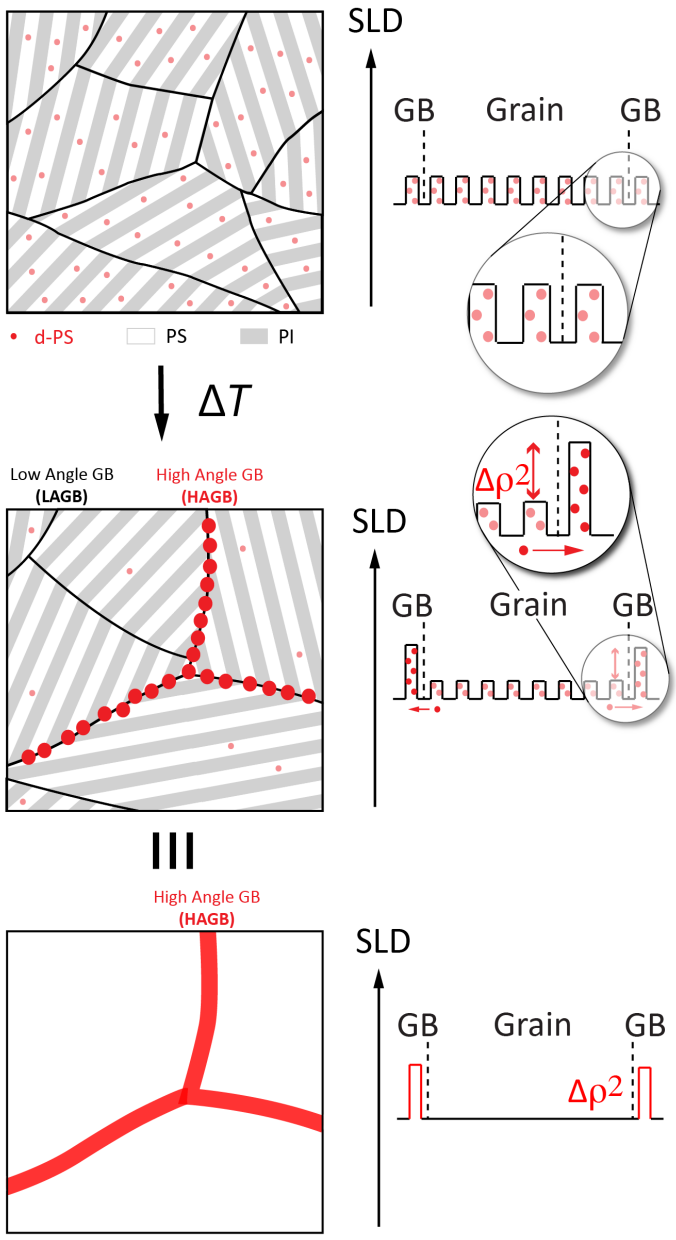

Figure 4- 13 Scheme that illustrates the filler segregation to HAGB and the corresponding scattering length density contrast change

4.4.1 USANS

As seen in the previous background section, the probing distance of scattering experiment is inversely related to the modulus of the scattering vector ($d \sim \frac{2\pi}{q}$, $q = \frac{4\pi}{\lambda}\sin\theta_s$, $2\theta_s$ denoting the scattering angle, and λ the radiation wavelength). Therefore,

in order to obtain micrometer scale structure information from scattering experiment, the scattering angle has to be ultra small. The source beam can be either X-ray or Neutron, however, "deuterium labeling" in neutron scattering technique makes it possible to track the location of the fillers for block copolymer/homo-polymer blend system. In this study, we have blended PS-PI block copolymer with deuterated polystyrene. Deuterated polystyrene has almost identical physical properties with hydrogen except for the neutron scattering length density. We have verified that deuterated polystyrene blended with polystyrene domain of block copolymer and assumed it will segregate to grain boundary region.

Figure 4- 14 shows the all the USANS/SANS graphs of as-cast and annealed PS-PI/d-PS samples. The range of q value is between $4\times10^{-5}\text{Å}^{-1} < q < 2\times10^{-3}\text{Å}^{-1}$. The as-cast sample does not scatter at all at this ultra-low q range. This is consistent with the expectation that the pristine hydrogenated block copolymer exhibits a low scattering contrast in neutron scattering. This remains unchanged after addition of a small amount of deuterated homopolymer if the homopolymer uniformly distributed within the material. After thermal annealing, the scattered intensity increases dramatically in ultra-low q range. The increase of scattered neutron intensity in ultra-low q range tells us that large-scale (>1μm^2) structure with scattering length density contrast appears with thermal annealing.

The 3-D scheme shown in **Figure 4- 14** illustrates the relevant size of features for three different q ranges. In ultrasmall q range (q<0.005Å^{-1}), scattering results from high angle grain boundaries segregated by deuterated polystyrene. The power-law exponent in this q range, -2 to -2.3, corresponds with the Porod scattering from 2D surfaces. As the intensity

in ultrasmall q increases with thermal annealing, this supports that there is scattering length density contrast in micrometer scale after thermal annealing. In small q range ($0.005Å^{-1} < q < 0.02Å^{-1}$), lamellar peaks are shown. The peak to baseline ratio

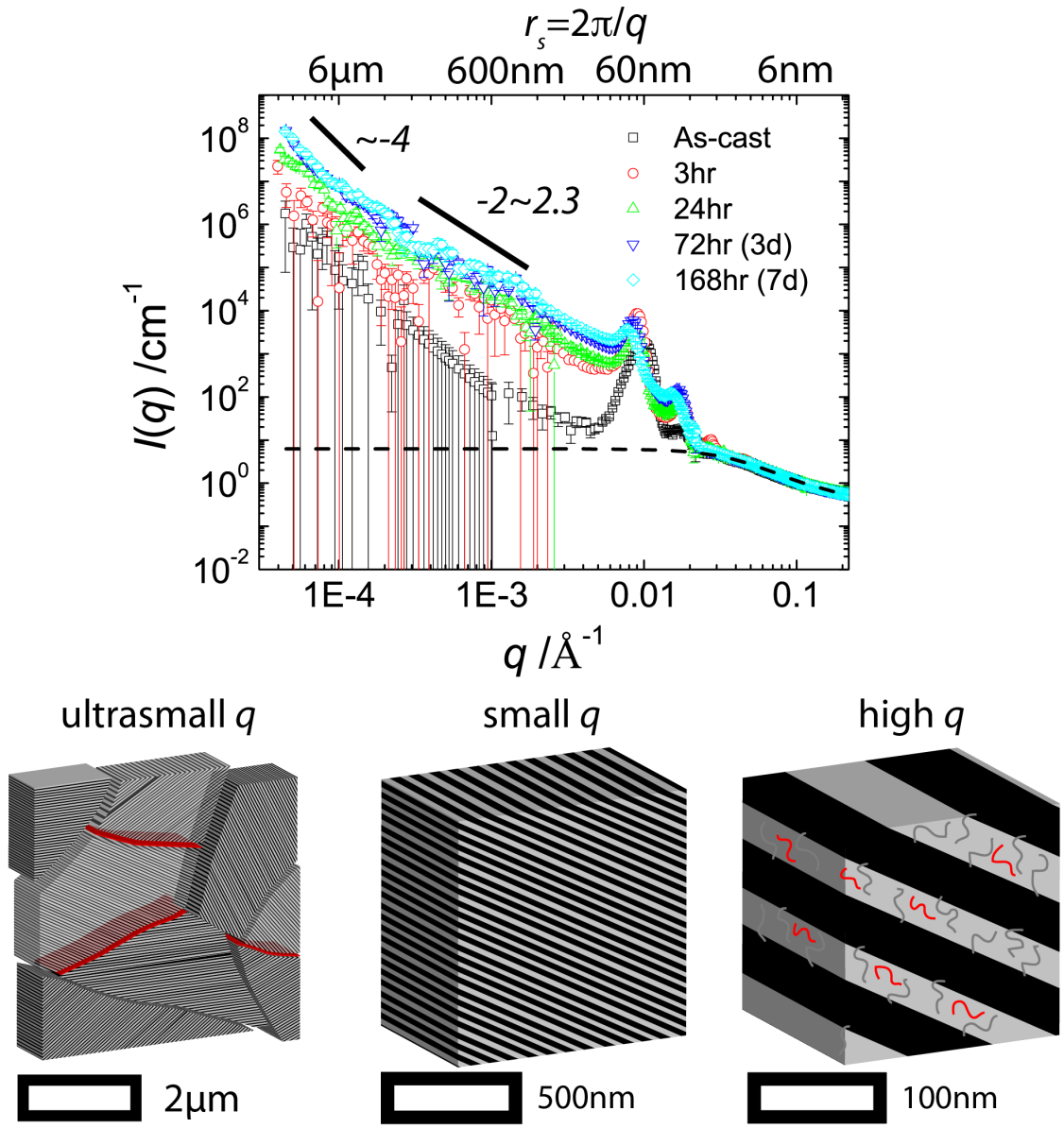

Figure 4- 14 (Top) USANS/SANS of as-cast and annealed samples. The dashed line denotes the Debye fit to the high q ($>0.02Å^{-1}$) resulting from thermal concentration fluctuation. (Bottom) 3-D Scheme that illustrates the size of features relevant for USANS and SANS.

decreases with thermal annealing, and this supports the idea that deuterated polystyrene is diffusing away from the lamellar domain. And high q range ($q > 0.02Å^{-1}$), the scattering is dominated by thermal concentration fluctuation in a lamellar domain. In a lamellar domain, graft polystyrene chains and deuterated polystyrene chains are entangled to each other. This is because they have neutral interaction to each other, and as they have large scattering length density contrast between them, this results in large scattering in high q range. The dashed line in the graph shows the Debye fit which corresponds to the scattering from the thermal concentration fluctuation.

All the raw data of USANS experiments are shown in the Appendix. The data correction procedure is explained in background section.

4.4.2 SANS analysis

To further understand the evolution of lamellae microstructure during thermal annealing, autocorrelation function of the scattering length density was calculated from SANS. The autocorrelation function is calculated by following equation and gives information about the spacing of this lamellae repeat unit. The peak position shown with arrow in Figure 4-15, denotes the length of lamellae repeat unit.

$$\gamma_1(x) = \frac{\int_0^\infty I_1(q)\cos qx dq}{\int_0^\infty I_1(q) dq} \tag{4.5}$$

Here, $I_1(q)$ is the Lorentz corrected intensity and is determined by $I_1(q) = I(q)q^2$.

In Figure 4- 16, the length of lamellae unit was seen to slowly increases with thermal annealing but the rate of growth slows down after short annealing. The mechanism of this slight increase is still in question but we assume that the redistribution

of the d-PS filler in PS-PI lamellae microstructure affects the state of chain conformation of PS-PI matrix.

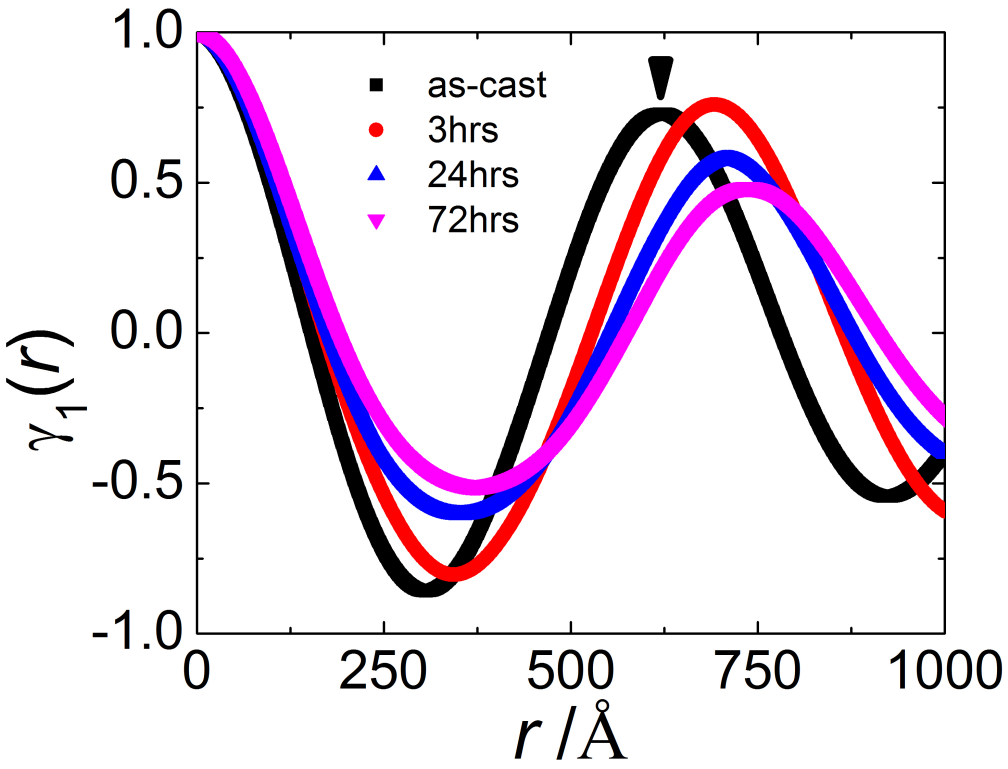

Figure 4- 15 autocorrelation function of the PS-PI/d-PS 10wt% as a function of thermal annealing time

Specifically, previous work by Winey and Thomas has shown that the addition of hP can contract the repeat length in lamellar BCP systems.[44] This is interpreted as a consequence of the effect of hP sequestration on the conformation in the respective blocks. Hence the observed expansion of lamellar spacing might be rationalized as a consequence of the reduction of hP concentration within grains during thermal annealing. Others, however, might also be at work and more research would be necessary to

understand this transition. It is noted that similar observation was made in the literature, however, no interpretation was offered.[24]

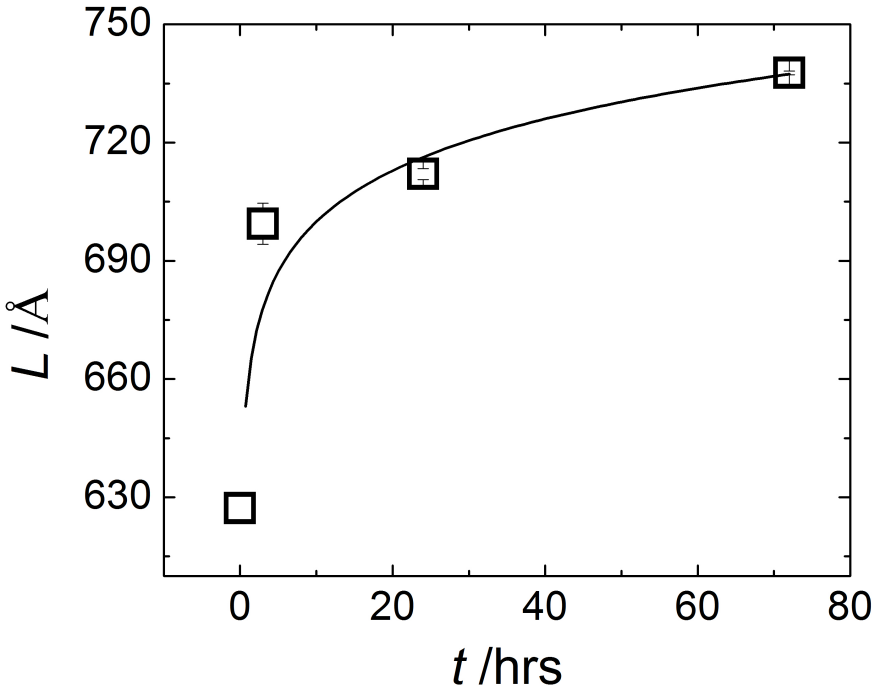

Figure 4- 16 The spacing of the lamellae microstructure of PS-PI/d-PS 10% obtained from autocorrelation function as a function of thermal annealing time

4.4.3 Invariant and scattering length density contrast

We have seen, with thermal annealing, the absolute intensity in ultra-small q range increases. This implies that micrometer-scale structure feature with scattering length density contrast emerges with thermal annealing. In order to quantify the total scattering intensity as a function of thermal annealing, the invariant (Q), was measured from the scattered neutron intensity. The invariant (Q) for ideal two phases is calculated using the following equation mentioned before:

$$Q = \frac{1}{2\pi^2}\int_0^\infty I(q)q^2dq = \phi(1-\phi)(SLD_{GB} - SLD_m)^2 \qquad (4.6)$$

Here, the $I(q)$ is the scattering intensity that is corrected for inhomogeneities that arises within grain phase including lamellae scattering and thermal concentration fluctuation scattering. The invariant equation for two-phase system requires that (1) the system contains only two phases and (2) the boundary between the two phases should be sharp.[51] However, in real materials system, there exist inhomogeneities including thermal density fluctuation and thermal concentration fluctuation. As our material system is in solid state being measured at room temperature, the scattering from thermal density fluctuation is assumed to be small compared to that from thermal concentration fluctuation.[72] As shown in section 4.4.1 and in Figure 4- 14, thermal concentration fluctuation results in strong intensity in high q range. The scattering intensity from these inhomogeneities including thermal concentration fluctuation and lamellae microstructure

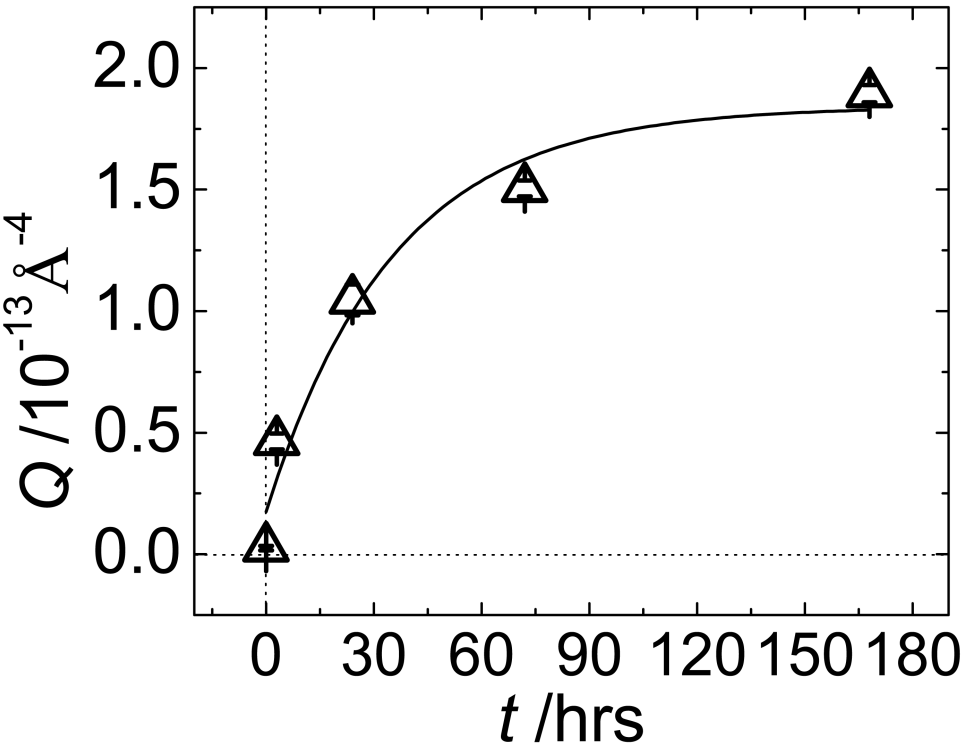

Figure 4- 17 Plot of invariant, Q, as a function of thermal annealing time

in the grain should corrected before applying invariant equation for ideal two phases. The plot of Q as a function of thermal annealing time is shown in

Figure 4- 17. The Q increases rapidly in the early annealing stage and saturates in the late annealing stage.

The scattering length density contrast between grain boundary and grain, ΔSLD ($=SLD_{GB}$-SLD_{m}), is calculated using the invariant equation.

$$(\Delta(SLD))^2 = (SLD_{GB} - SLD_m)^2 = \frac{1}{2\pi^2}\int_0^\infty i(q)q^2dq \cdot \frac{1}{\phi(1-\phi)} \qquad (4.7)$$

where ΔSLD is the SLD contrast between grain and grain boundary

SLD_{GB} is the SLD of grain boundary

SLD_{Grain} is the SLD of grain

ϕ is the volume fraction of grain boundary

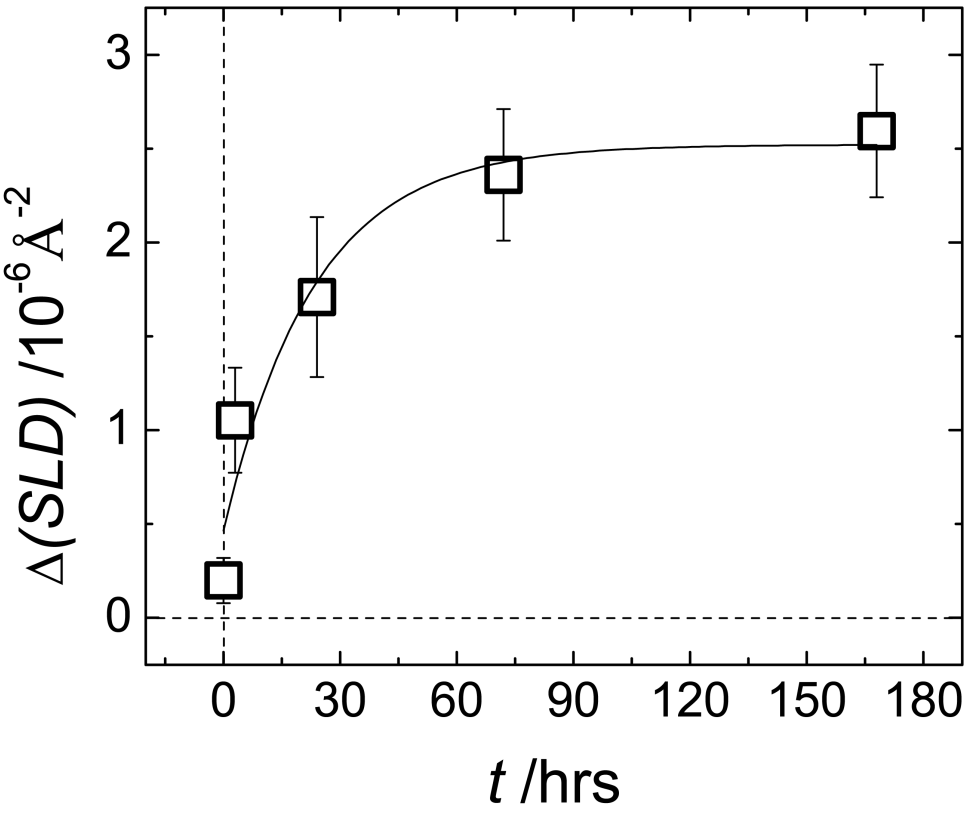

Figure 4- 18 Plot of scattering length density (SLD) contrast between grain boundary and grain as a function of thermal annealing time

The Figure 4- 18 shows the plot of scattering length density (*SLD*) contrast between grain boundary and grain as a function of thermal annealing time. The *SLD* contrast is close to 0 meaning that filler is uniformly distributed between grain boundary and grain in as-cast sample, however, increases rapidly after thermal annealing meaning that filler is non-uniformly distributed. The rate of increase decreases with thermal annealing and after 3 days of thermal annealing, the SLD contrast saturates to ~$2.5 \times 10^{-6}\text{Å}^{-2}$.

4.5 Evolution of Filler Concentration Within Grain Boundaries

From the experimental *SLD* contrast, we can further calculate the relative volume fraction of d-PS segregated to grain boundary (x) using the following relationship between the

scattering length density and the volume fraction of segregated d-PS in grain boundary region.

$$\Delta SLD = SLD_{GB} - SLD_{Grain} \tag{4.8}$$

$$SLD_{GB} = \frac{xf}{\phi} SLD_{d-PS} + \frac{(\phi - xf)}{\phi} SLD_{PS-PI} \tag{4.9}$$

$$SLD_{Grain} = \frac{(1-x)f}{1-\phi} SLD_{d-PS} + \frac{(1-\phi-(1-x)f)}{1-\phi} SLD_{PS-PI} \tag{4.10}$$

Here, the variables are volume fraction of high angle grain boundary (ϕ), total volume fraction of d-PS in the blend (*f*) and *SLD* of d-PS and PS-PI. $\frac{xf}{\phi}$ and $\frac{(\phi-xf)}{\phi}$ are the volume fraction of d-PS and PS-PI in grain boundary. *xf* is the total volume of d-PS segregated to grain boundary and dividing it by the volume of grain boundary, ϕ, gives the volume percent of d-PS in the grain boundary. The volume of PS-PI in grain boundary is determined by subtract the volume of d-PS from that of grain boundary, $(\phi - xf)$ and dividing it by ϕ gives the volume fraction of PS-PI in grain boundary. Therefore, SLD_{GB} is calculated by relative contribution from both d-PS and PS-PI based on their volume fractions. Similarly, the volume fraction of d-PS in grain is determined by dividing the total volume fraction of d-PS in grain, $(1-x)f$, by the total volume fraction of the grain, $1-\phi$. And also, the volume fraction of PS-PI in grain is determined by dividing the total volume fraction of PS-PI in grain, $(1-\phi-(1-x)f)$, by the total volume fraction of the grain, $1-\phi$. Table 4- 6 summarizes the composition of GB and grain.

	PS-PI	d-PS
GB	$\frac{(\phi(t)-x(t)f)}{\phi(t)}$	$\frac{x(t)f}{\phi(t)}$
Grain	$\frac{(1-\phi(t)-(1-x(t))f)}{1-\phi(t)}$	$\frac{(1-x(t))f}{1-\phi(t)}$

Table 4- 6 Volume fraction of PS-PI and d-PS in grain boundary and grain.

From Appendix, SLD_{GB} and SLD_{Grain} are plotted as a function of total volume fraction of d-PS segregated to HAGB (x) for 5 different annealing conditions. Because of the different volume fraction of HAGB (ϕ), SLD_{GB} and SLD_{Grain} are different for the same total amount of segregated d-PS. For as-cast sample, as it has the largest volume fraction of HAGB (ϕ), the *SLD* increases most slowly among 5 samples. In contrast, the SLD increases most rapidly for longest thermally annealed samples. The ΔSLD is calculated by subtracting SLD_{Grain} from SLD_{GB}.

By comparing the $\Delta(SLD)$ measured from invariant equation with the plot of $\Delta(SLD)$ as a function of x, we can find out how much d-PS is segregated to HAGB.

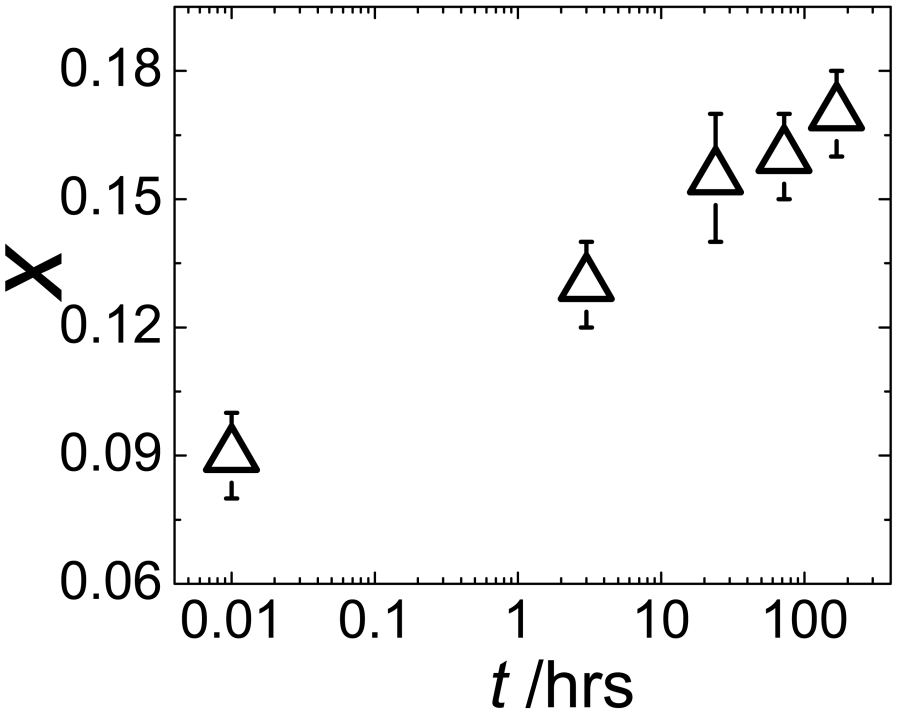

Figure 4- 19 Total volume fraction of segregated d-PS in HAGB of PS-PI (x) as a function of thermal annealing time.

Figure 4- 19 shows the plot of total amount of d-PS segregated to HAGB of PS-PI. It shows that in as-cast sample, 9 Vol% of the total d-PS is segregated within HAGB of PS-PI. The volume fraction of HAGB of as-cast sample is 6.5 Vol%, therefore, we can infer that there is already small amount of d-PS segregation within grain boundary. This can be attributed to the solvent residue, even after rapid evaporation using Rotavapor, because it gives the d-PS mobility to diffuse to grain boundary. The total fraction of segregated d-PS within grain boundary slows down and saturates at 0.18.

The total fraction of d-PS segregation along with the volume fraction of HAGB can be used to calculate the volume fraction of segregated filler per HAGB volume using following equation.

$$C(GB,t) = \frac{x(t)f}{\phi(t)} \tag{4.11}$$

Similarly, the volume fraction of remaining filler per grain volume is calculated by:

$$C(Grain,t) = \frac{\big(1-x(t)\big)f}{1-\phi(t)} \tag{4.12}$$

The normalized kinetics of filler segregation, $\frac{C(GB,t)-C(GB,0)}{C(GB,max)-C(GB,0)}$, is plotted as a function of thermal annealing time in Figure 4- 20.

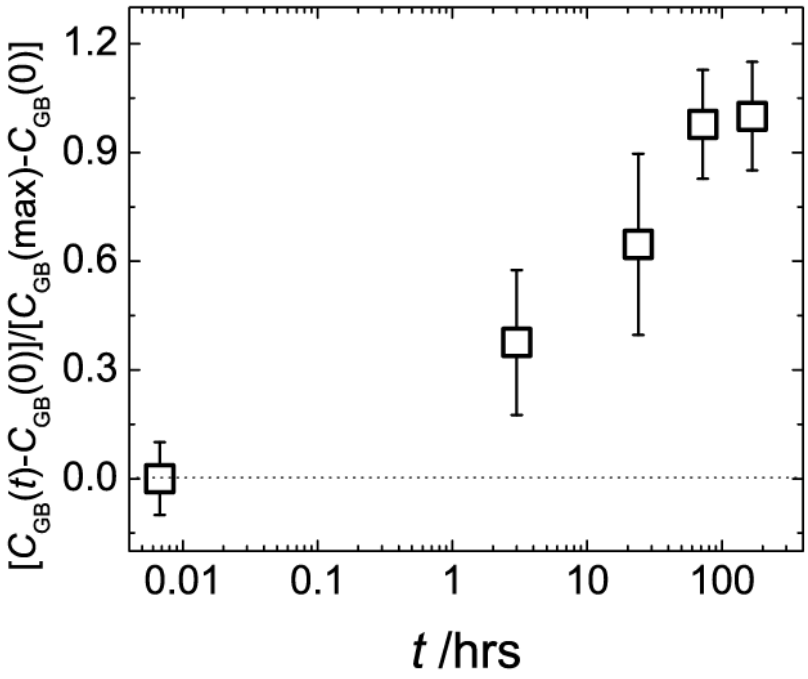

Figure 4- 20 Normalized kinetics of filler concentration within grain boundary is plotted as a function of thermal annealing time

Furthermore, the volume fraction of PS-PI in grain boundary and grain is easily calculated using following equation:

$$C_{PS-PI}(GB,t) = \frac{(\phi(t)-x(t)f)}{\phi(t)} \tag{4.13}$$

$$C_{PS-PI}(Grain, t) = \frac{\left(1 - \phi(t) - \left(1 - x(t)\right)f\right)}{1 - \phi(t)} \tag{4.14}$$

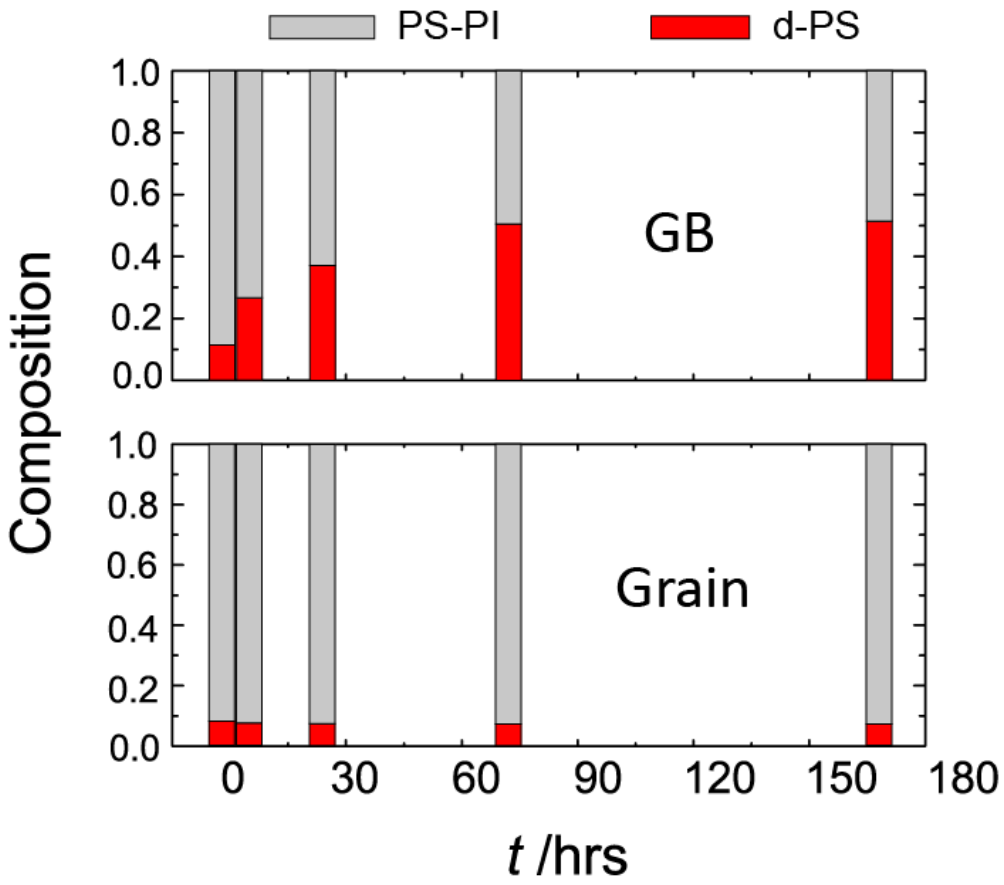

Figure 4- 21 (Top) Composition of GB and (Bottom) grain as a function of thermal annealing time. The fraction of PS-PI is shown as the gray bar while the fraction of d-PS is shown as the red bar. Within HAGB, the fraction of d-PS is increasing while that of the grain is very slowly decreasing

The composition of grain boundary and grain is shown in Figure 4- 21. The upper graph shows the composition of grain boundary as function of time. The volume fraction of d-PS (red bar) in GB increases and saturates at ~0.5. The lower graph shows the composition of grain as a function of time. The volume fraction of d-PS in grain

decreases very slowly because the volume of d-PS diffused out from lamellae is very small compared to the volume of the whole grain.

4.6 Kinetics of grain boundary segregation

The grain boundary segregation describes the localized segregation of solute species at grain boundary in solids. Grain boundary segregation in metals and alloys was widely studied because it is detrimental to many important mechanical properties. It is known to cause problems such as fracture in temper brittleness, creep embrittlement, stress relief cracking of weldments or grain boundary corrosion. For metals and alloys, solute species in solids suffers from elastic strain energy that increases the overall free energy. The lattice disorder at grain boundary gives rise to solute segregation within grain boundary in order to minimize the overall free energy. Grain boundary segregation occurs by unequal distribution of solute species between grain boundary and the grain in accordance with the statistics of thermodynamics. [73]

Building on the research from grain boundary segregation in metals and alloys, mostly from McLean, in this chapter, I will further illustrate the kinetics of filler segregation behavior in block copolymer. Also, the methods of calculating the equilibrium concentration of filler will be illustrated and the value will be compared with that we obtained from experiment.

During the thermal annealing process, the solute in the material containing grain boundary redistributes itself in order to minimize the total free energy of the system. This redistribution is time dependent and represents the kinetics of filler segregation to its equilibrium state. The segregation of solute within grain boundaries can be simplified to

Fick's law diffusion of solute to a thin plate between two semi-infinite solid. The chief assumption made is, grain diameter >> grain boundary thickness which is applicable for BCP/hP systems. And another assumption is that the solute concentration in grain does

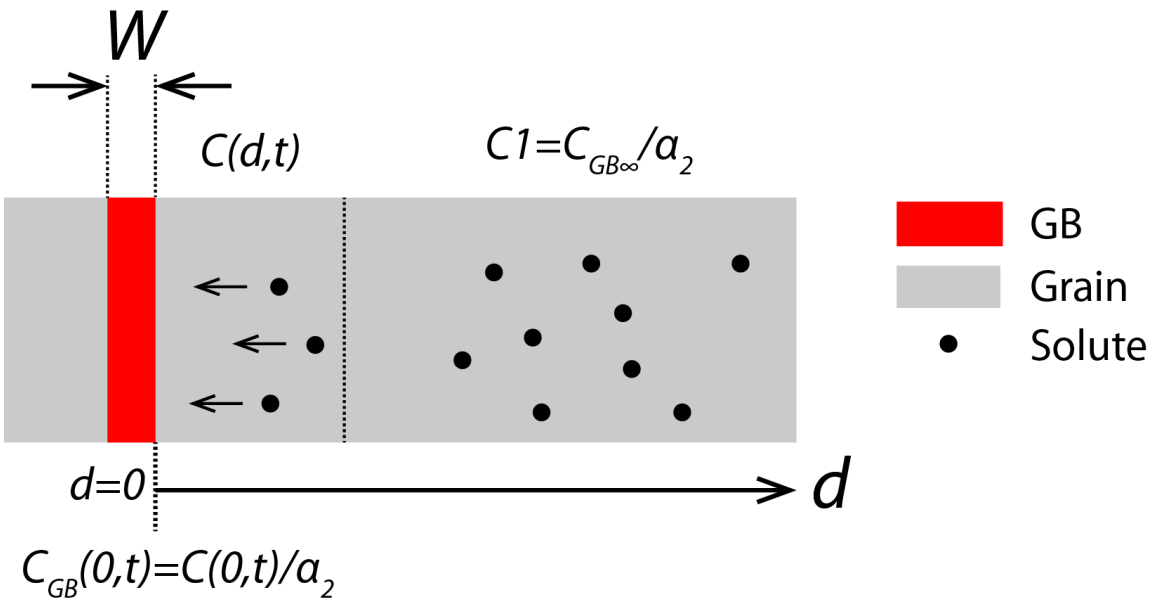

Figure 4- 22 Scheme that shows the filler segregation in a thin boundary between two semi-infinite crystals proposed by McLean [74]

not change as the filler concentration in grain boundary builds up. This is also true for our system because the volume of grain is very large compared to that of grain boundary.

According to McLean's approach, as shown in Figure 4- 22, the equation for kinetics of filler segregation is as follow[74]

$$\frac{C(gb,t)-C(gb,0)}{C(gb,\infty)-C(gb,0)} = 1 - e^{\frac{4Dt}{\alpha_2^2 W^2}} erfc\left(2\sqrt{\frac{Dt}{\alpha_2 W}}\right) = 1 - e^{A_M t} erfc\left(\sqrt{A_M t}\right) \quad (4.15)$$

where $C(gb,t)$ is the grain boundary concentration after time t.

$C(gb,0)$ is the initial grain boundary concentration.

$C(gb,\infty)$ is the equilibrium grain boundary concentration attained after infinite time

α_2 is the ratio $C(gb,\infty)/C(1)$

$C(1)$ is the grain interior concentration, assumed constant

D is the diffusion coefficient

W is the thickness of the grain boundary

$A_M = \frac{4D}{\alpha_2 W}$ is the fitting parameter

Figure 4- 23 shows the previously measured kinetics of normalized grain boundary concentration fitted to McLean's equation. The fit agrees well with the measured points in the plot. The fit gives $A_M = \frac{4D}{\alpha_2 W} = 6.62 \cdot 10^{-5} s^{-1}$. The α_2 is the ratio $\frac{C(gb,\infty)}{C(1)} \sim 6.8$.

Thickness of grain boundary, W, is equal to length of lamellae repeat unit, L~72nm, as shown in previous chapter. And now the diffusion coefficient of d-PS filler can be calculated. The calculated $D = 4.0 \cdot 10^{-14} cm^2 s^{-1}$. This value is in reasonable agreement with results by Lodge and coworkers who reported diffusion coefficient of PS (M_w=14kg/mol, 25kg/mol) in PS-PVP (2.2 x 10^4 g/mol). [75]

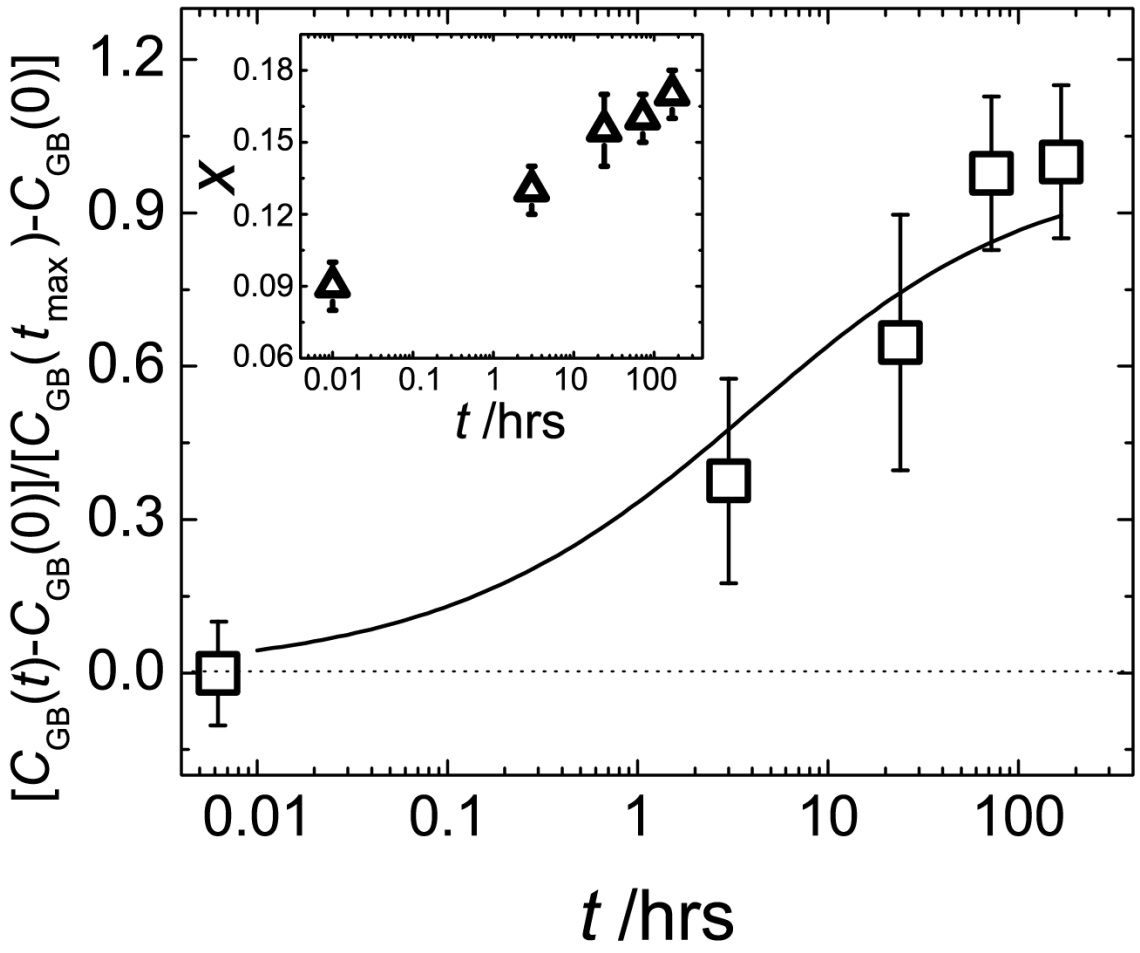

Figure 4- 23 Normalized kinetics of filler concentration within grain boundary is plotted as a function of thermal annealing time with McLean fit. (t_{max} is 168 hrs)

4.7 Summary

The USANS and TEM based techniques were used for comparative study on grain coarsening behavior of block copolymer. From the DSC and SANS, it was verified that d-PS dissolved well in PS domain of the PS-PI matrix and the composite maintained lamellae microstructure during the thermal annealing process. Similar system with *athermal* filler showed that there exists a threshold tilt angle, and above that angle the filler segregates within grain boundary. It is notable that the density of the segregated

filler within grain boundary stayed almost constant regardless of the tilt angle. This result makes it possible to assume there is no scattering length density difference between d-PS decorated high angle grain boundaries with different tilt angles. The grain mapping technique gave information about the microstructure including the volume percent of high angle grain boundary. Neutron scattering conducted on as-cast and annealed film showed very different results. With thermal annealing, the scattering intensity of ultra-small q increased dramatically. Invariant (Q) equation was used to quantify the increase of this scattering intensity with thermal annealing. Invariant (Q) along with the volume fraction of high angle grain boundary were used to calculate the scattering length density contrast change between the grain boundary and grain, and finally, the kinetics of grain boundary segregation was obtained with simple equation. The kinetics of the d-PS segregation in PS-PI agrees well with the McLean's model. The physical parameters such as diffusion coefficient of filler, obtained by applying McLean's model had good agreement with the literature value.

5. Kinetics of filler segregation to grain boundary during grain coarsening of block copolymer

5.1 Introduction

The thermodynamics and kinetics of grain boundary segregation was widely studied for metals and alloys. Due to the lattice disorder in structural defects such as grain boundary, the Gibbs free energy of the interface is higher than that of lattice without defects. To minimize the Gibbs free energy, the grain boundary interacts with lattice defects such as dislocations, vacancies and solute species. The interaction with the solute species results in grain boundary segregation.

There are two different types of grain boundary segregation. First is the equilibrium segregation, and this is caused by any inhomogeneous structure that gives sites with lower free energy for solute species. These sites include various in-homogeneities such as grain boundary, dislocations, free surface, phase interfaces, defect sites and stacking faults. At each temperature, there exists the equilibrium concentration of segregation that is approached as time goes infinity. The rate of approaching the equilibrium concentration is governed by diffusion. Second is the non-equilibrium segregation and it depends on kinetic events. The example of the non-equilibrium segregation includes solute pile-up at a moving interface and solute coupling to vacancies that are moving to other defects. In this research, we will only discuss equilibrium segregation since it is believed to be more relevant to the present material system. [76][73]

In previous chapter we have used McLean's model to explain the kinetics of grain boundary segregation in lamellar PS-PI microstructure. The physical parameters (D, α_2, d) that we obtained by fitting McLean's model were in good agreement with our

system. In this chapter, we further expand our study to calculate the equilibrium concentration of grain boundary segregation and make comparison with the experimental result.

5.2 Equilibrium grain boundary concentration

5.2.1 Langmuir-McLean theory

The original and simplest form of the segregation isotherm was proposed by McLean.[76] He proposed a model of *P* solute atoms distribute randomly amongst *J* lattice sites and *p* solute atoms distribute among *j* grain boundary sites. **Figure 5- 1** shows the scheme that illustrates this model system. The total free energy of this system due to solute atom is,

$$G = pe + PE - kT[\ln j!\, J! - \ln(j-p)!\, p!\, (J-P)!\, P!] \tag{5.1}$$

where *E*, *e* are the energy of the solute atom in lattice and grain boundaries and $\mathrm{k_B}$ is the Boltzmann constant. The ln-term on the right side of the equation is the configurational entropy of the solute atoms in grain and grain boundary. The equilibrium state occurs when *G* has the minimum value and this can be determined by differentiating *G* respect to *p*. At this state where *G* is minimum, the grain boundary analogue of Langmuir absorption at free surface is obtained,

$$\frac{X_0}{X_b^0 - X_b} = \frac{X_c}{1 - X_c} \exp\left(\frac{-\Delta G}{RT}\right) \tag{5.2}$$

where X_b^0 is the fraction of the grain boundary monolayer available for segregated atoms at saturation, X_b is the actual fraction covered with segregant, X_c is the bulk solute molar fraction and ΔG is the free energy of segregation per mole of solute.

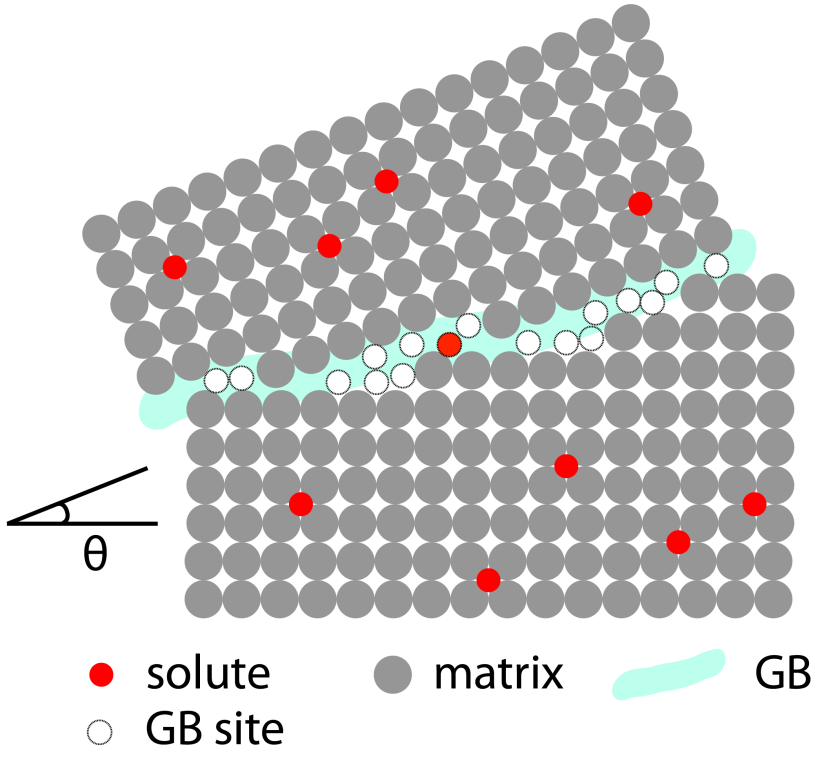

Figure 5- 1 Scheme that illustrates two crystals mis-oriented at the boundary. The solutes are dissolved in the lattice and occupy interstitial sites.

The value of ΔG was estimated by elastic strain energy of solute in the lattice by McLean. Following this argument we can extract ΔG in lamellar PS-PI microstructures by analysis of the strain energy of polymer chain stretching in grain boundaries. The next chapter will discuss our methods to calculate ΔG of grain boundary in lamellae PS-PI. In the following chapters, chain stretching energy will be determined based on the chain conformation within the grain boundary described by Gido and Thomas.[28] Geometrical constraints of graft chain as a function of tilt angle will be developed based on our observation of grain boundary morphology. The change of graft chain length that satisfies the geometric constraints of given tilt angle, θ, will be calculated and used to determined the strain stretching energy.

5.2.2 Chain stretching energy

In order to calculate ΔG, we have to estimate the strain energy of the polymer chain within the grain boundary. In this chapter, we will estimate the strain energy based on chain stretching energy by subsequent equations. Figure 5- 3 shows the chain volume element geometry in flat lamellae and in chevron grain boundary. As the curvature increases from flat state, the length of the lamellae increases at the grain boundary, therefore, graft chain has to stretch in order to fill the space. This stretching energy gives rise to high free energy state of the grain boundary. Our analysis follow an approach first used by Gido et al who analyzed the mechanics of deformations of layered structures.[28]

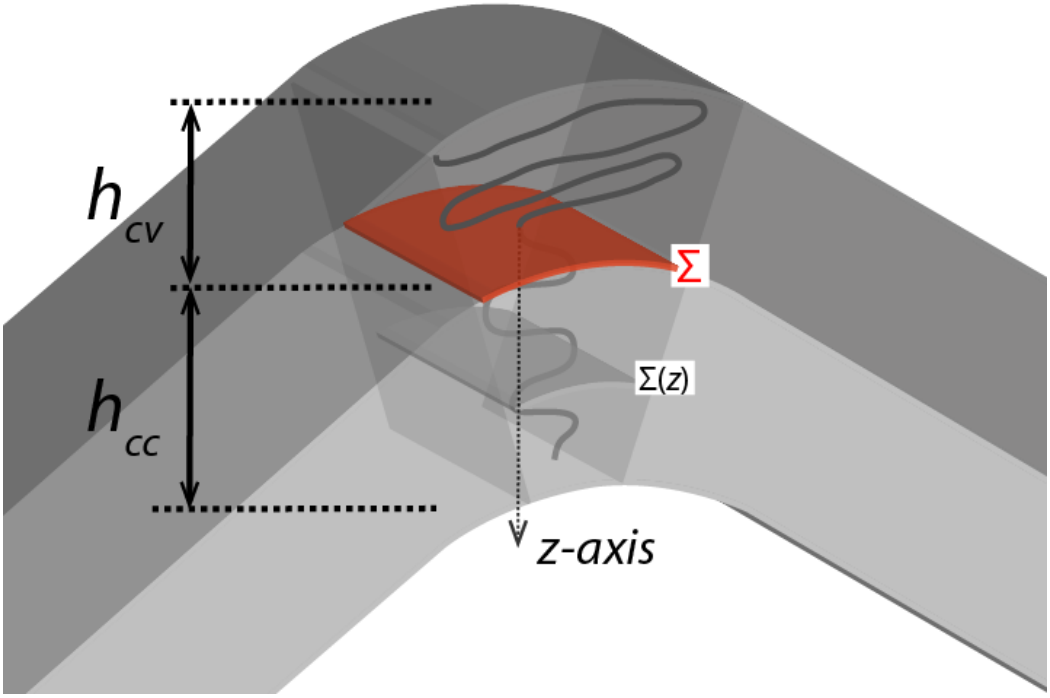

Figure 5- 2 Schematic diagram showing the geometry of chain volume element at tilt angle grain boundary. $\boldsymbol{\Sigma}$ is the interfacial area per chain at the interface, $\boldsymbol{\Sigma(z)}$ is the two dimensional slice through volume element parallel to the interface at height *z*. h is the graft chain length and they are distinguish as h_{cv} and h_{cc} for convex and concave side.

As shown in Figure 5- 2, the two dimensional slice through a volume element parallel to the PS-PI interface at a height z above the interface has area of:

$$\Sigma(z) = (1 + zc_1)(1 + zc_2)\Sigma = (1 + 2Hz + Kz^2)\Sigma \tag{5.3}$$

Where c_1,c_2 are principal curvatures of the interface, Σ is the interfacial area per chain, H is the mean curvature and K is the Gaussian curvature of the interface.

Due to the conservation of volume for a single chain, it is subject to the following constraint,

$$\int_0^h \Sigma(z)\, dz = N_A \nu \tag{5.4}$$

where h is the height of the grafted polymer, ν is the volume per monomer, N_A is the degree of the polymerization of the block on the side of the interface under consideration and z is height.

Integrating two equations above gives a cubic equation that relates h and Σ:

$$\frac{1}{3}Kh^3 + Hh^2 + h - \frac{N_A \nu}{\Sigma} = 0 \tag{5.5}$$

For chevron model, which is cylindrically shaped, K=0, therefore:

$$h^2 + \frac{h}{H} - \frac{N_A \nu}{H\Sigma} = 0 \tag{5.6}$$

In chevron grain boundary, the lamellar spacing at the center of the boundary becomes $2h^*/\cos\theta$ and it should equal to the sum of convex and concave brush height. Lamellar spacing at flat interface, L, is $4h^*$.

$$h_{cc} + h_{cv} = \frac{2h^*}{\cos\theta} \tag{5.7}$$

where h_{cc}, h_{cv} are brush height of concave and convex side of the PS-PI interface.

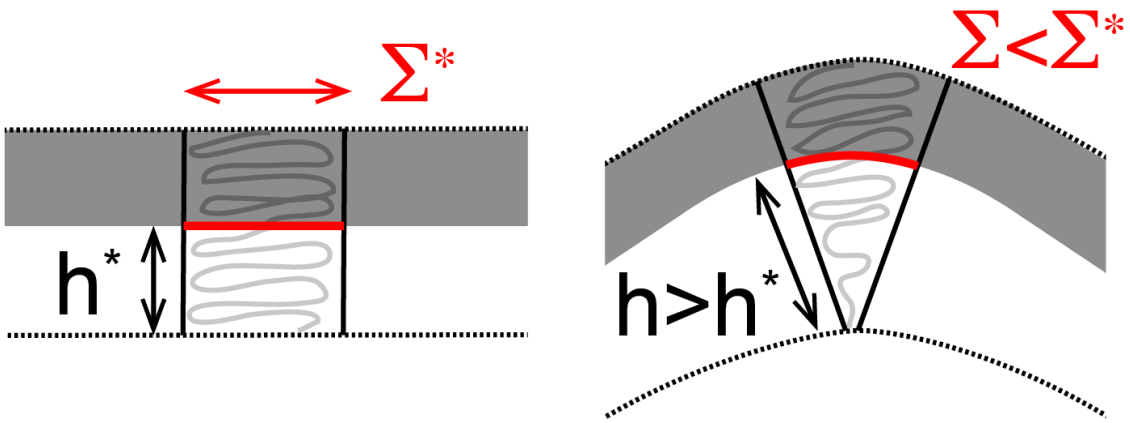

Figure 5- 3 chain volume element geometry in (left) flat plane (right) grain boundary. (L=4h*)

Solving above two equations simultaneously yields a relationship for possible combinations of H and Σ that satisfies the geometric constraints of given tilt angle, θ.

For convex side of the interface:

$$h^2 + \frac{h}{H} - \frac{N_A \upsilon}{\mathrm{H}\Sigma} = 0 \tag{5.8}$$

$$h_{cv} = \frac{-\frac{1}{H} \pm \sqrt{\frac{1}{H^2} + \frac{4N_A\upsilon}{\Sigma H}}}{2} = -\frac{2}{H} \pm \sqrt{\frac{1}{4H^2} + \frac{N_A\upsilon}{\Sigma H}} \tag{5.9}$$

In this quadratic equation we chose the value that satisfies $h_{cv} > 0$.

For concave side of the interface:

$$h^2 - \frac{h}{H} + \frac{N_A \upsilon}{\mathrm{H}\Sigma} = 0 \tag{5.10}$$

$$h_{cc} = \frac{2}{H} \pm \sqrt{\frac{1}{4H^2} - \frac{N_A\upsilon}{\Sigma H}} \tag{5.11}$$

Also in this quadratic equation we chose the value that satisfies $h_{cc} > 0$.

$$\therefore h_{cc} + h_{cv} = \frac{2}{H} - \sqrt{\frac{1}{4H^2} - \frac{N_A\upsilon}{\Sigma H}} - \frac{2}{H} + \sqrt{\frac{1}{4H^2} + \frac{N_A\upsilon}{\Sigma H}} = \sqrt{\frac{1}{4H^2} + \frac{N_A\upsilon}{\Sigma H}} - \sqrt{\frac{1}{4H^2} - \frac{N_A\upsilon}{\Sigma H}} \tag{5.12}$$

As the sum of convex and concave brush heights should equal to lamellae spacing:

$$\frac{2h*}{\cos\theta/_2} = \sqrt{\frac{1}{4H^2} + \frac{N_A v}{\Sigma H}} - \sqrt{\frac{1}{4H^2} - \frac{N_A v}{\Sigma H}} \tag{5.13}$$

$$\frac{4Hh*}{\cos\theta/_2} = \sqrt{1 + \frac{4HN_A v}{\Sigma}} - \sqrt{1 - \frac{4HN_A v}{\Sigma}} = \left(1 + \frac{4HN_A a_A^3}{\Sigma}\right)^{1/2} - \left(1 - \frac{4HN_A a_A^3}{\Sigma}\right)^{1/2} \tag{5.14}$$

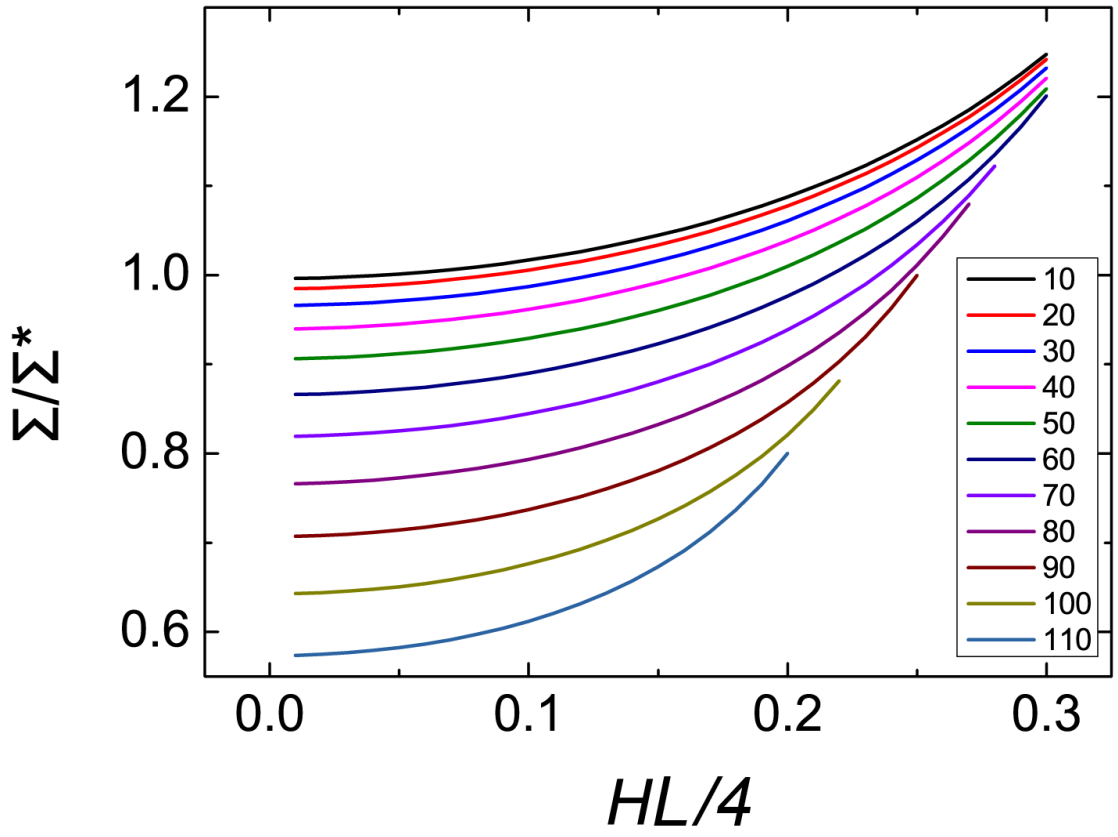

Figure 5- 4 The plot of **Σ/Σ*** as a function of the dimensionless *HL/4* for various tilt angle chevron grain boundary

Figure 5- 4 shows the possible combinations of H and Σ that satisfies the geometric constraints of given tilt angle, θ. Even though this graph gives numerous selection of H and Σ combinations for given tilt angle, θ, H is pre-determined from the

previous finding that the grain boundary width is constant. As the curvature of the grain boundary is related to the grain boundary width by:

$$R = \frac{W}{2\sin{}^{\theta}/_{2}} \tag{5.15}$$

where W=72nm, the curvature can be calculated for given angle. In order to test the validity of the calculated curvature, I have compared it with experimental values measured from TEM images.

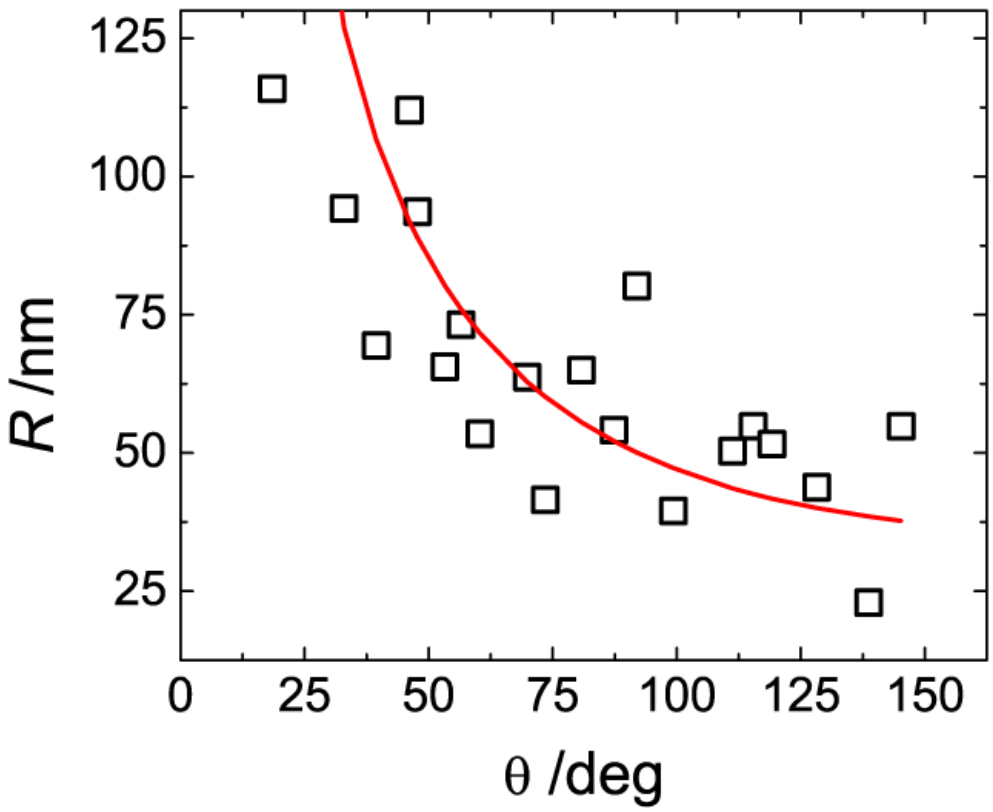

Figure 5- 5 (square) measured and (Red line) calculated radius of curvature as a function of tilt angle

As shown in **Figure 5- 5**, calculated and measured radius of curvature as a function of tilt angle shares similar trends. As $H = 1/(2R)$, we can choose the corresponding $HL/4$ values in Figure 5- 4 to find $\boldsymbol{\Sigma/\Sigma^*}$.

However, we still do not know the flat interface area per junction, $\boldsymbol{\Sigma}^*$, and flat lamellae brush height, h^*. The flat interface area per junction can be calculated using equations from the paper by Winey et al. [44]

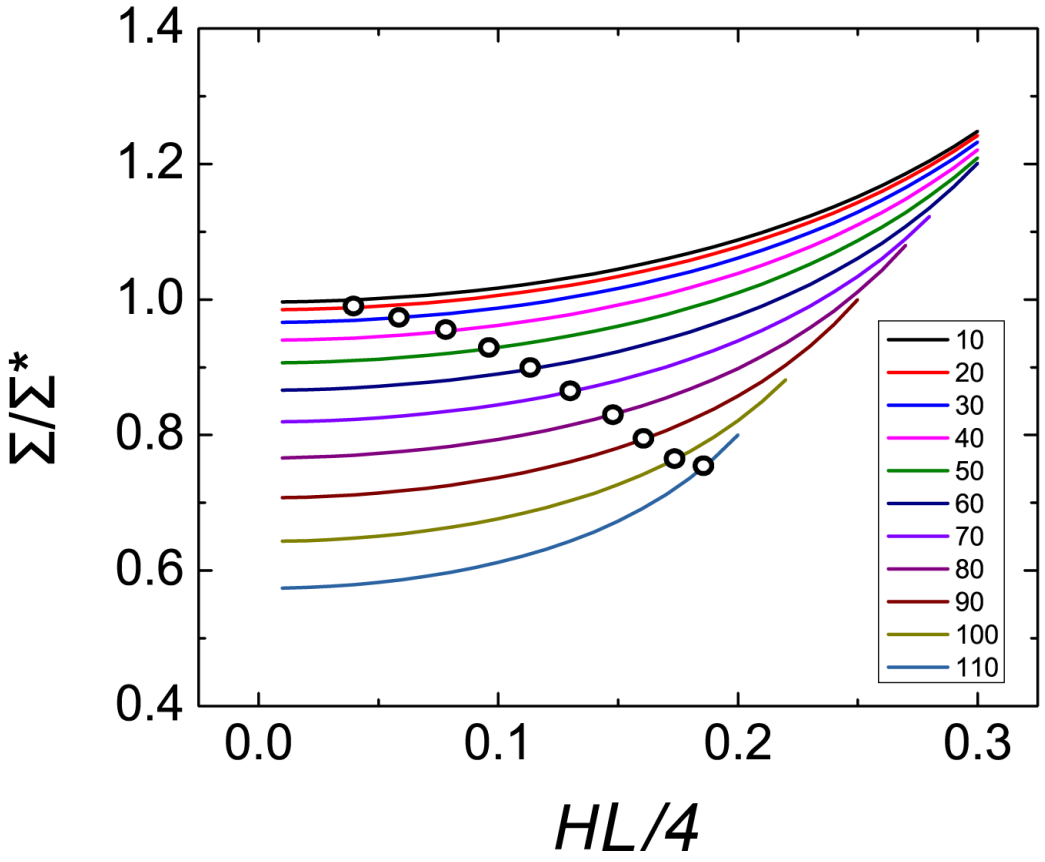

Figure 5- 6 The plot of $\boldsymbol{\Sigma/\Sigma}^*$ as a function of the dimensionless Hh^* for various tilt angle chevron grain boundary. The circles denotes the $\boldsymbol{\Sigma}$ and H combination that satisfies constant W=72nm

The average are per junction on the PS-PI interface is given by

$$\Sigma^* = \frac{2M_{PI}}{N_{AV}\tilde{\rho}_{PI}(1-\phi_{PS})L} \tag{5.16}$$

Here, $L = 4h^*$ and the flat lamellae brush height, h^*, is calculated by

$$h^* = \frac{N_A \nu}{\Sigma^*} \tag{5.17}$$

The physical parameters required to calculate Σ^*, h^* are summarized in Table 5- 1. Figure 5- 6 shows the Σ and *H* combinations that satisfy the constant grain boundary width.

M_{PI}	$\tilde{\rho}_{PI}$	ϕ_{PS}	L	Σ^*	h^*
46,000g/mol	0.903g/cm^3	0.46	72nm	438Å^2	164Å

Table 5- 1 physics parameters used to calculate flat interface area per junction and flat lamellae brush height

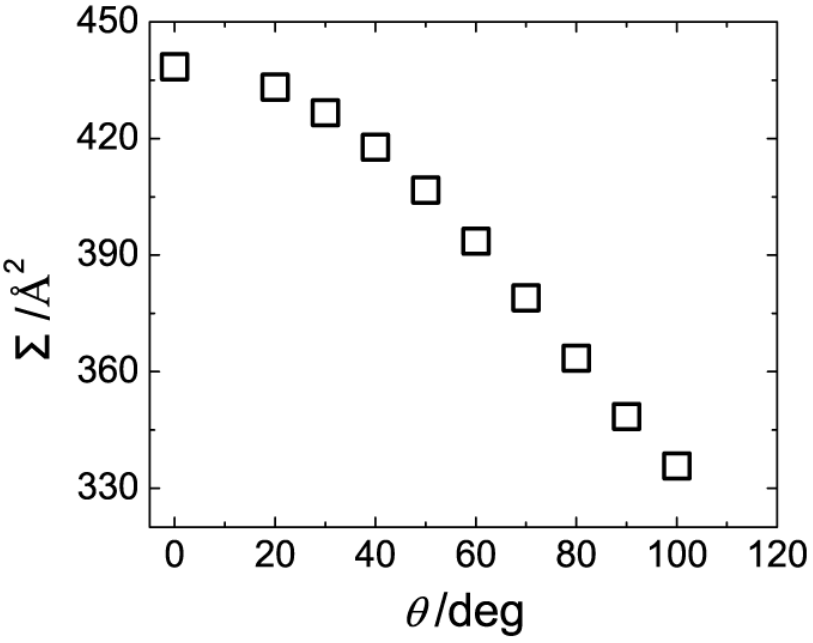

Figure 5- 7 Plot of area per junction as a function of tilt angle

Figure 5- 7 shows the change of area per junction as a function of tilt angle of the chevron grain boundary. It is shown that as the tilt angle increases, the area per junction decreases.

Now, the concave and convex graft chain length can be calculated as a function of tilt angle as we can substitute corresponding Σ for tilt angle to the following equation:

$$h^2 - \frac{h}{H} + \frac{N_A \upsilon}{H\Sigma} = 0 \qquad (5.18)$$

H is positive for concave side and negative for convex side of the interface.

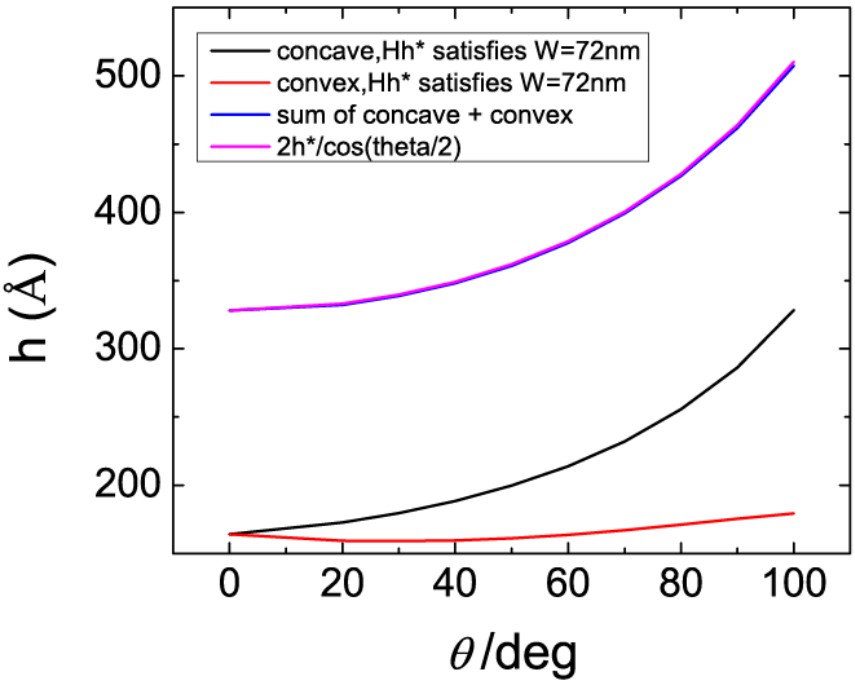

Figure 5- 8 Graft chain length of concave, convex side of the interface, sum of the convex and concave and estimated length of lamellae as a function of tilt angle

Figure 5- 8 shows the change of the convex, concave graft change length as a function of tilt angle. While the length of the convex graft chain stays almost constant, that of the concave graft chain increases rapidly.

The strain energy is calculated using the equation:

$$F(N, R_f) \cong kT \left(\frac{R_f}{R_0}\right)^2 \tag{5.19}$$

Here, R_f is the length of the chain after deformation.

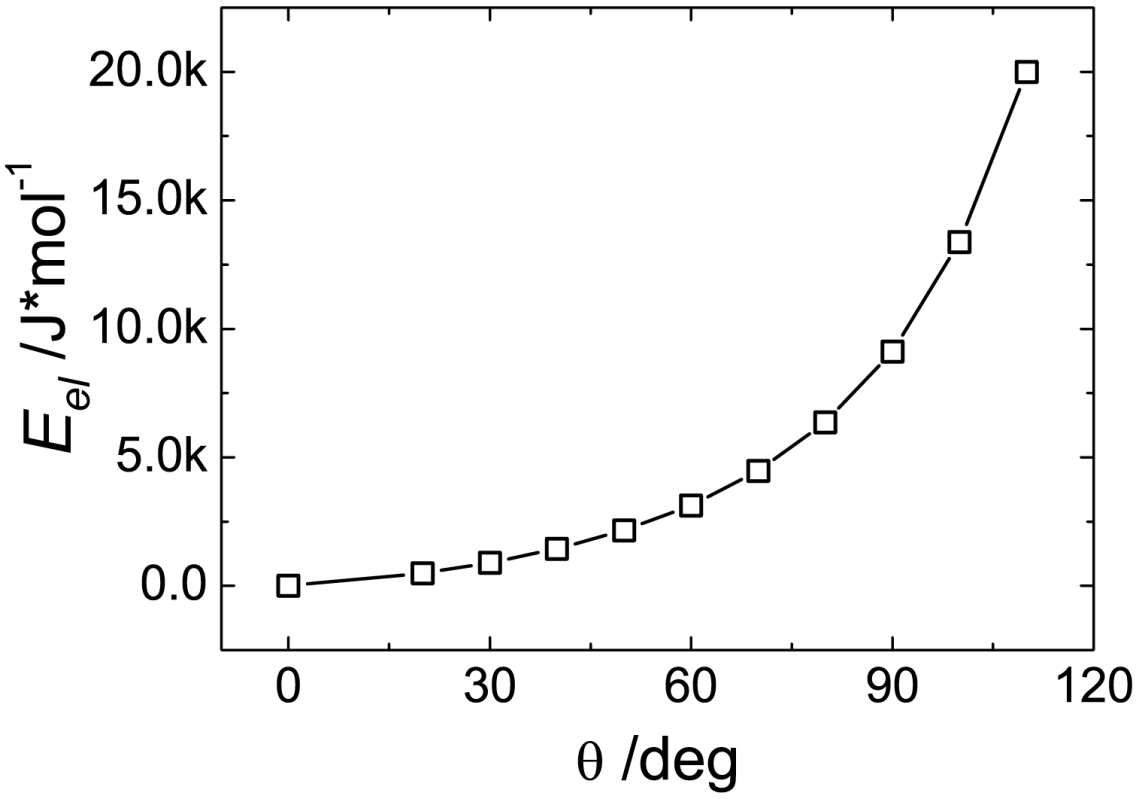

Figure 5- 9 Elastic strain energy of graft chain as a function of grain boundary tilt angle determined from equation 5.19.

Figure 5- 9 shows the change of strain energy of the graft chain in concave side of the interface as a function of tilt angle. However, this plot is only applicable to chevron grain boundary. From the self-consistent field theory (SCFT) by Matsen et al.[35]the grain boundary energy deviates from that of chevron from 78°. We can approximate the average strain energy of high angle grain boundary from strain energy calculated from chevron grain boundary. Figure 5- 10 shows SCFT study of grain boundary tension as a

function of tilt angle. Even though strain energy of tilt angle of 60° is small, the population of HAGB is dominated by θ>90°, therefore, the average grain boundary tension can be approximated by chevron strain energy at tilt angle of 80~90°. At 85°, the strain energy of the chevron grain boundary is ~7700 J/mol. As the chain stretching energy is dominant energy penalty in grain boundary of block copolymer, we can approximate that ΔG~ 7700 J/mol.

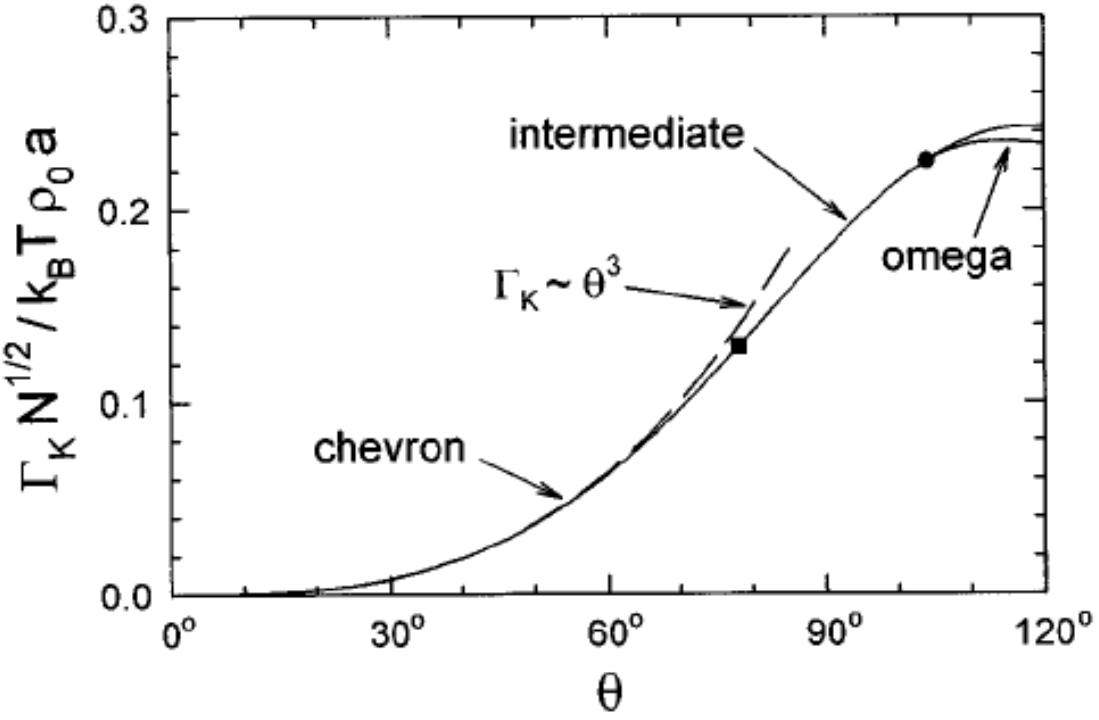

Figure 5- 10 Grain boundary tension as a function of angle. The solid square indicates the crossover from the chevron to intermediate kink and the solid dot indicates the phase transition to the omega kink. Reproduced from reference 35.[35]

5.2.3 Equilibrium grain boundary concentration

After obtaining ΔG, the equilibrium grain boundary segregation can be calculated using Langmuir-McLean's theory

$$\frac{X_b}{X_b^0 - X_b} = \frac{X_c}{1 - X_c} \exp\left(\frac{-\Delta G}{RT}\right) \tag{5.20}$$

$$\frac{X_b}{1 - X_b} = \frac{0.088}{1 - 0.088} \exp\left(\frac{-\frac{7700J}{mol}}{\frac{8.31J}{(K \cdot mol)403K}}\right)$$

$$\therefore X_b \sim 0.49$$

Figure 5- 11 shows the equilibrium concentration of grain boundary segregation as a function of free energy of segregation using Langmuir-McLean isotherm. The calculated equilibrium concentration of grain boundary segregation is very close (within 6% error) to what we have measured in the previous chapter using scattering length density contrast. The experimentally measured concentration of grain boundary segregation was 0.52.

The possible sources of error exist both in experiment and the calculation. First, in experimental part, even though we have covered large area exceeding 500 μm^2, volume fraction of HAGB measured from TEM might not be identical to that of the whole volume. Also the estimating volume fraction of HAGB from two-dimensional projection using quantitative stereology has potential source of error. The error in measurement of thickness of the sample, ~250 μm, could give rise to the absolute intensity of the neutron scattering experiment. Second, in calculation part, we have used approximated model for the energy penalty associated with grain boundary. However, the elastic strain energy from chain stretching within grain boundary is the strongest and dominating other factors such as interfacial surface energy.

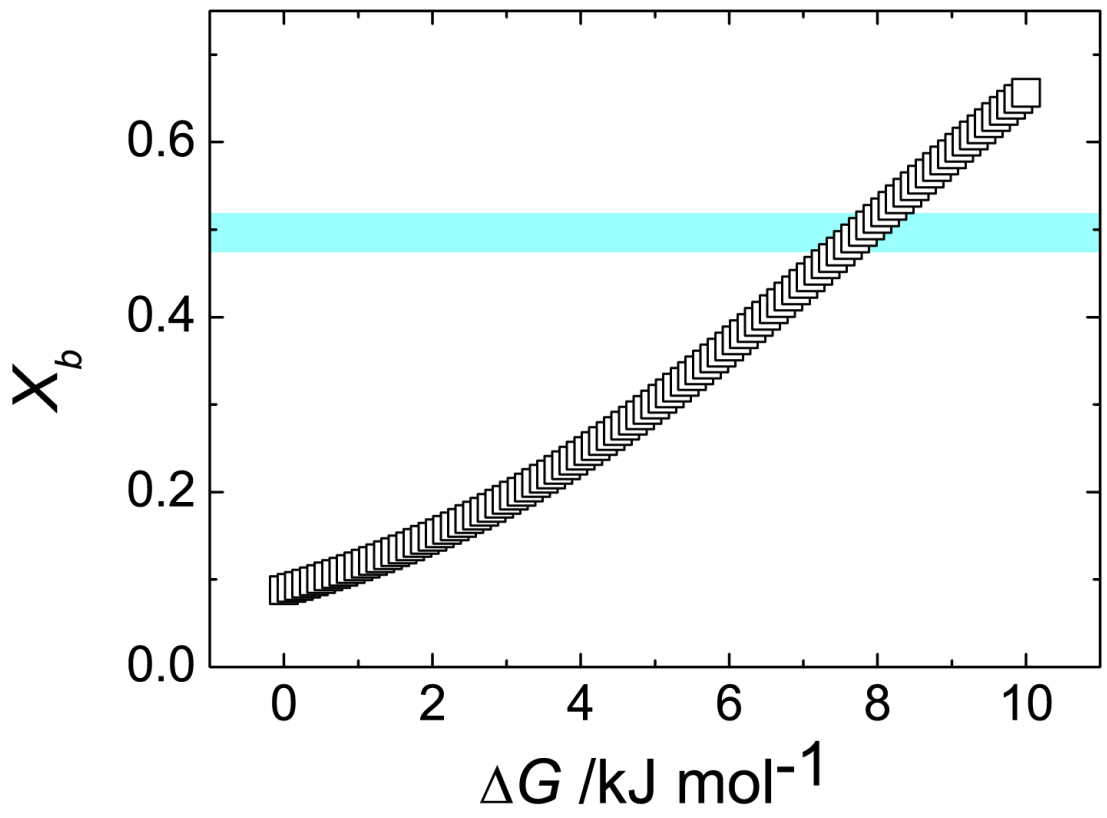

Figure 5- 11 Equilibrium concentration of grain boundary segregation calculated as a function of free energy of segregation using Langmuir-McLean isotherm

5.3 Summary

This chapter it spent on studying the equilibrium concentration was grain boundary segregation. It estimates the final state of the kinetics study provided in the previous chapter. The Langmuir-McLean's segregation isotherm used to predict the equilibrium concentration of filler in grain boundary. However, the elastic strain energy of solute they use in metals is different from that of lamellae block copolymer where chain stretching is the dominant contribution to the high free energy of the defect. Therefore, based on Gido et el.'s work on describing the geometry of the graft chain in the center of the grain boundary, we have calculated the graft chain length and

corresponding chain stretching energy as a function of tilt angle. The equilibrium concentration of grain boundary segregation was obtained by substituting the chain stretching energy of graft chain to Langmuir-McLean's segregation isotherm. The equilibrium concentration calculated was 0.49, and it is very close to the value that we measured from previous chapter, 0.52.

6. Conclusion and Suggestions for Future Research

The kinetics as well as the equilibrium of the grain boundary segregation in lamellae block copolymer was studied. The kinetics of grain boundary segregation shows there are two different stages. First stage is the early annealing stage, and the concentration of filler increases rapidly. The second stage is the later annealing stage, and the concentration of filler does not increase rapid anymore but almost stays constant. The second stage is near the equilibrium stage of the grain boundary segregation. The kinetics of the grain boundary segregation is in agreement with the McLean's equation that was used in metals and alloy as the basic motivation for the segregation are applicable to both the systems. The kinetic model that is constructed gives us rich knowledge about the segregation behavior of filler in lamellae block copolymer system.

In order to verify the grain boundary segregation behavior obtained in chapter 4, we have further more investigated the equilibrium concentration of grain boundary segregation using Langmuir-McLean's segregation isotherm. The elastic strain energy of the graft chain within grain boundary was calculated based on our TEM images and equations borrowed from literature. The obtained equilibrium concentration of grain boundary segregation agreed very close to the concentration that we obtained experimentally in the longest thermal annealing sample shown in chapter 4. This gives more credibility of the results that we have gotten in chapter 4. This Langmuir-McLean's segregation isotherm applied to our system gives more understanding about what determines the equilibrium concentration of grain boundary segregation.

In the Future, the morphology of high angle grain boundary will be studied. I have preliminary result that correlates the morphology of high angle grain boundary and the neutron scattering and it is briefly shown as supplementary information. Developing this technique will enable us to study the evolution of high angle grain boundary morphology during thermal annealing procedure. This will give deeper understanding on the grain boundary morphology and networks in lamellae block copolymer.

And the order-order transition observed in BCP/AuPS annealed system will be studied. We have observed lamellar to cylinder order-order transition at high angle grain boundary where higher density of AuPS is observed. Comparison of AuPS density map with microstructure map will enable quantitative analysis on this observation.

Also, the role of matrix-filler interaction on grain coarsening of BCP will be studied. In the present study where *athermal* filler is used, the filler segregated to grain boundary and stabilizes the high angle grain boundary energy. However, *thermal* filler, has favorable interaction in the matrix, and therefore, there is driving force for filler to be uniformly mixed in lamellae domains. We assume that the grain coarsening behavior of BCP/*thermal* filler will be more accelerated than BCP/*athermal* filler because thermal filler will not segregate to grain boundary, therefore, the high angle grain boundary will remain unstable.

7. Supplementary information

Analysis of HAGB morphologies

Not only the absolute intensity of USANS but also the shape of it gives us structural information about the grain boundary structure. Until this part we have only used neutron scattering data for invariant (Q) analysis to calculate scattering length density contrast.

For annealed samples, USANS graph can be divided into two regions where each region decays with different power-law. This means that material system have multiple structural levels. It is common that PS-PI/d-PS 10wt% annealed systems show power-law decay with exponent between -2 and -2.5 at $\xi < q < r_0$ ($1\times10^{-4}\text{Å}^{-1} < q < 5\times 10^{-3}\text{Å}^{-1}$). At lower q values ($4\times10^{-5}\text{Å}^{-1} < q < 8\times10^{-5}\text{Å}^{-1}$), the slope changes to higher value. The power law exponents at this q range are between -3 and -4. The q range where power law exponent is $2<m<2.3$ corresponds to the scattering from a clustered networks (mass fractal) explained in background chapter. From the previous studies, the athermal filler will segregate to high angle grain boundaries and its network will mostly correspond to the trace of high angle grain boundary. The parameter ξ is the characteristic size for mass fractal and r_0 is the radius of the individual units that are clustered. Detail about mass fractal scattering is explained in background chapter. r_0 can be assumed to be the diameter of the segregated deuterated polystyrene and this value is comparable to the spacing of the lamellar domain as the grain boundary thickness is similar to or less than lamellar spacing. ξ can be measured from the lower cut-off q value of this mass fractal scattering. As shown in Figure 7- 1, the cut-off q value gradually

increases with the duration of thermal annealing. This implies that the characteristic size of the mass fractal decreases with thermal annealing and it is worthwhile to compare with the length of individual HAGB as a function of thermal annealing time.

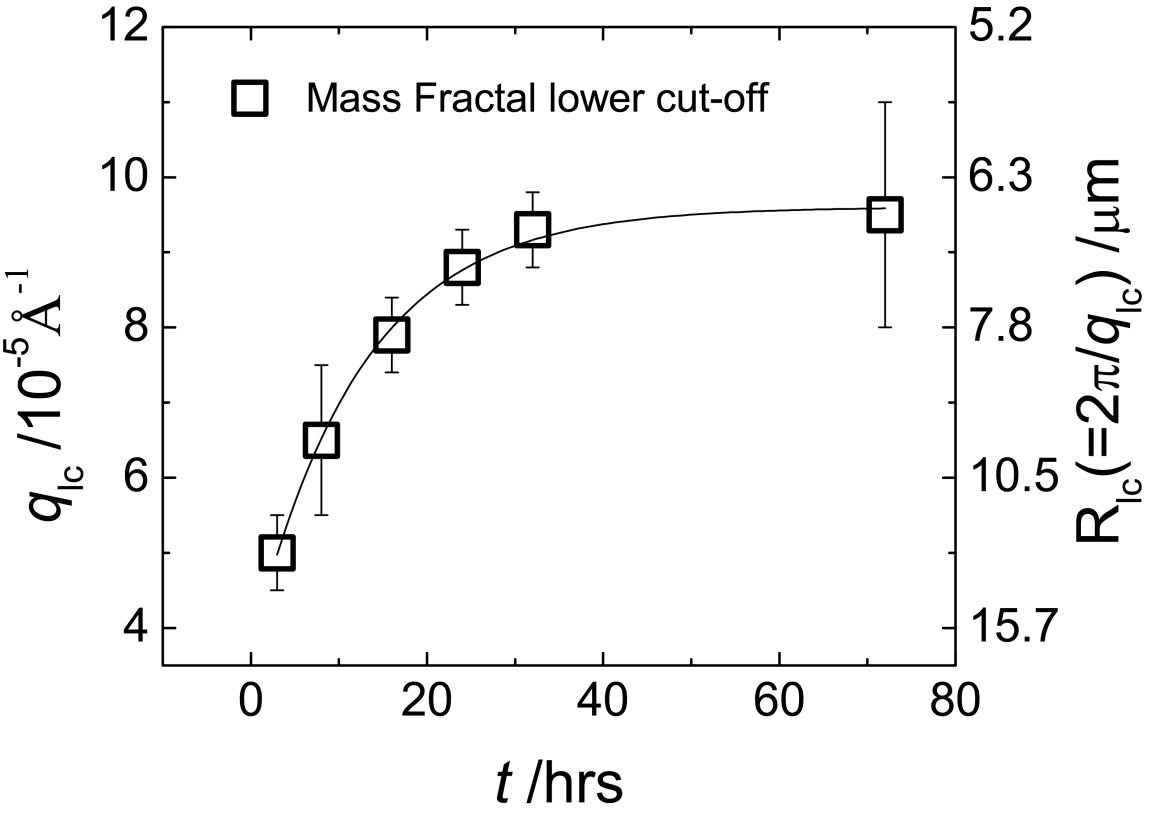

Figure 7- 1 Plot of lower cut-off q and corresponding length of mass fractal structure as a function of thermal annealing time for PS-PI/d-PS 10wt% sample

The linear regime in log-log USANS/SANS graph has the slope that ranges from -2 to 2.3 show lower cutoff q, q_{lc}. The low cutoff q shows the size of the aggregated d-PS in HAGB[77]. In Figure 7- 1, as the PS-PI/d-PS is thermally annealed, q_{lc} shifts toward higher q and this suggests that the size of the aggregate is decreasing. The comparison with the HAGB map is being conducted and will be the future work.

8. Reference

[1] G. Strobl, *The Physics of Polymers*, Springer, **1997**.

[2] N. Hadjichristidis, H. Iatrou, S. Pispas, M. Pitsikalis, *J. Polym. Sci. Part A Polym. Chem.* **2000**, *38*, 3211.

[3] M. S. H. Block, H. Iatrou, A. Avgeropoulos, N. Hadjichristidis, **1994**, *27*, 6232.

[4] M. Bockstaller, R. Kolb, E. L. Thomas, *Adv. Mater.* **2001**, *13*, 1783.

[5] F. S. Bates, G. H. Fredrickson, *Annu. Rev. Phys. Chem.* **1990**, *41*, 525.

[6] Y. Kang, J. J. Walish, T. Gorishnyy, E. L. Thomas, *Nat. Mater.* **2007**, *6*, 957.

[7] J. Yoon, C. Park, E. L. Thomas, *Polymer (Guildf).* **2003**, *44*, 6725.

[8] E. D. Gomez, A. Panday, E. H. Feng, V. Chen, G. M. Stone, A. M. Minor, C. Kisielowski, K. H. Downing, O. Borodin, G. D. Smith, N. P. Balsara, *Nano Lett.* **2009**, *9*, 1212.

[9] C. Guo, Y. H. Lin, M. D. Witman, K. a. Smith, C. Wang, A. Hexemer, J. Strzalka, E. D. Gomez, R. Verduzco, *Nano Lett.* **2013**, *13*, 2957.

[10] M. R. Bockstaller, R. a. Mickiewicz, E. L. Thomas, *Adv. Mater.* **2005**, *17*, 1331.

[11] S. C. Warren, L. C. Messina, L. S. Slaughter, M. Kamperman, Q. Zhou, S. M. Gruner, F. J. DiSalvo, U. Wiesner, *Science* **2008**, *320*, 1748.

[12] M. R. Bockstaller, E. L. Thomas, *J. Phys. Chem. B* **2011**, *107*, 10017.

[13] M. R. Bockstaller, E. L. Thomas, *Phys. Rev. Lett.* **2004**, *93*, 166106.

[14] E. J. W. Crossland, M. Kamperman, M. Nedelcu, C. Ducati, U. Wiesner, D. Smilgies, G. E. S. Toombes, M. a Hillmyer, U. Steiner, H. J. Snaith, *Nano Lett.* **2009**, *9*, 2807.

[15] and E. L. T. Yoel Fink, Ausustine M.Urbas, Moungji G. Bawendi, John D.Joannopoulos, *J. Light. Technol.* **1999**, *17*, 1963.

[16] P. a. Kossyrev, M. R. Bockstaller, E. L. Thomas, *Langmuir* **2005**, *21*, 814.

[17] D. E. Fogg, L. H. Radzilowski, R. Blanski, R. R. Schrock, E. L. Thomas, *Macromolecules* **1997**, *30*, 417.

[18] B.-K. Cho, a Jain, S. M. Gruner, U. Wiesner, *Science* **2004**, *305*, 1598.

[19] N. a. Lynd, A. J. Meuler, M. a. Hillmyer, *Prog. Polym. Sci.* **2008**, *33*, 875.

[20] J. Derouchey, T. P. Russell, H. M. Jaeger, **2000**, 3250.

[21] T. Q. Chastek, T. P. Lodge, *J. Polym. Sci. Part B Polym. Phys.* **2006**, *44*, 481.

[22] T. Q. Chastek, T. P. Lodge, **2004**, *37*, 4891.

[23] M. C. Newstein, B. a Garetz, N. P. Balsara, M. Y. Chang, H. J. Dai, *Macromolecules* **1998**, *31*, 64.

[24] R. T. Myers, R. E. Cohen, **1999**, 2706.

[25] S. P. Gido, J. Gunther, L. Thomas, D. Hoffman, **1993**, 4506.

[26] S. P. Gido, E. L. Thomas, *Macromolecules* **1994**, *27*, 849.

[27] S. P. Gido, E. L. Thomas, *Macromolecules* **1997**, *30*, 3739.

[28] S. P. Gidot, E. L. Thomas, **1994**, 6137.

[29] S. P. Gido, D. W. Schwark, E. L. Thomas, M. D. C. Gonçalves, *Macromolecules* **1993**, *26*, 2636.

[30] Y. Nishikawa, H. Kawada, H. Hasegawa, T. Hashimoto, *Acta Polym.* **1993**, *44*, 247.

[31] D. J. J. R.D. Doherty, D.A. Hughes, F.J. Humphreys, J.J. Jonas, H. J. M. M.E. Kassner, W.E. King, T.R. McNelley, A. D. Rollett, *Mater. Sci. Eng. A* **1997**, *238*, 219.

[32] L. S. Gottstein, G. and Shvindlerman, *Grain Boundary Migration in Metals: Thermodynamics, Kinetics, Applications*, CRC Press, **1999**.

[33] G. H. Fredrickson, K. Binder, *J. Chem. Phys.* **1989**, *91*, 7265.

[34] Y. Tsori, D. Andelman, M. Schick, **1999**, *61*, 11.

[35] M. W. Matsen, *J. Chem. Phys.* **1997**, *107*, 8110.

[36] M. Matsen, M. Schick, *Phys. Rev. Lett.* **1994**, *72*, 2660.

[37] Z.-G. Wang, S. a. Safran, *J. Chem. Phys.* **1991**, *94*, 679.

[38] T. Kawakatsu, *Statistical Physics of Polymers, An Introduction*, Springer, Berlin, **2001**.

[39] R. R. Netz, D. Andelman, M. Schick, **1998**, 4.

[40] S. Villain-Guillot, R. R. Netz, D. Andelman, M. Schick, **1998**, *249*, 9.

[41] H. J. Ryu, D. B. Fortner, S. Lee, R. Ferebee, M. De Graef, K. Misichronis, A. Avgeropoulos, M. R. Bockstaller, **2013**.

[42] M. Bockstaller, D. Fortner, H. Ryu, G. Rohrer, *Phys. Rev. Lett.* **2012**, *108*, 107801.

[43] T. Hashimoto, H. Tanaka, H. Hasegawa, *Macromolecules* **1990**, *23*, 4378.

[44] K. I. Winey, E. L. Thomas, L. J. Fetters, *Macromolecules* **1991**, *24*, 6182.

[45] K. R. Shull, K. I. Winey, **1992**, *25*, 2637.

[46] E. Burgaz, S. P. Gido, *Macromolecules* **2000**, *33*, 8739.

[47] J. Listak, M. R. Bockstaller, *Macromolecules* **2006**, *39*, 5820.

[48] R. J. Spontak, R. Shankar, M. K. Bowman, A. S. Krishnan, M. W. Hamersky, J. Samseth, M. R. Bockstaller, K. Rasmussen, *Nano Lett.* **2006**, *6*, 2115.

[49] M. P. Stoykovich, M. Müller, S. O. Kim, H. H. Solak, E. W. Edwards, J. J. de Pablo, P. F. Nealey, *Science* **2005**, *308*, 1442.

[50] H. J. Ryu, J. Sun, A. Avgeropoulos, M. R. Bockstaller, *Macromolecules* **2014**, *47*, 1419.

[51] R. Roe, *Methods of X-Ray and Neutron Scattering in Polymer Science*, **2000**.

[52] R. Rinaldi, L. Liang, *Neutron Appl. Earth, Energy Environ. Sci.* **2009**, 1.

[53] "NCNR webpage," **n.d.**

[54] G. R. Strobl, M. Schneider, *J. Polym. Sci. Polym. Phys. Ed.* **1980**, *18*, 1343.

[55] S. R. Kline, *J. Appl. Crystallogr.* **2006**, *39*, 895.

[56] T. Vad, W. F. C. Sager, *J. Appl. Crystallogr.* **2011**, *44*, 32.

[57] S. Koizumi, H. Hasegawa, T. Hashimoto, *Macromolecules* **1994**, *27*, 7893.

[58] M. Rubinstein, *Polymer Physics*, Oxford, **2003**.

[59] M. W. Matsen, F. S. Bates, *Macromolecules* **1996**, *29*, 1091.

[60] A. Hariharan, S. K. Kumar, T. P. Russell, *J. Chem. Phys.* **1993**, *98*, 4163.

[61] S. K. Kumar, T. P. Russell, *Macromolecules* **1991**, *24*, 3816.

[62] T. Hashimoto, N. Sakamoto, T. Koga, *Phys. Rev. E* **1996**, *54*, 5832.

[63] H. J. Dai, N. P. Balsara, B. A. Garetz, M. C. Newstein, **1996**, 3677.

[64] B. A. Garetz, N. P. Balsara, H. J. Dai, Z. Wang, M. C. Newstein, B. Majumdar, **1996**, 4675.

[65] W. G. Kim, M. Y. Chang, B. a Garetz, M. C. Newstein, N. P. Balsara, J. H. Lee, H. Hahn, S. S. Patel, *J. Chem. Phys.* **2001**, *114*, 10196.

[66] W. G. Kim, B. a Garetz, M. C. Newstein, N. P. Balsara, *J. Polym. Sci. Part B-Polymer Phys.* **2001**, *39*, 2231.

[67] M. Y. Chang, F. M. Abuzaina, W. G. Kim, J. P. Gupton, B. A. Garetz, M. C. Newstein, N. P. Balsara, L. Yang, S. P. Gido, R. E. Cohen, Y. Boontongkong, A. Bellare, *Macromolecules* **2002**, *35*, 4437.

[68] N. P. Balsara, C. M. Marques, B. a Garetz, M. C. Newstein, S. P. Gido, *Phys. Rev. E. Stat. Nonlin. Soft Matter Phys.* **2002**, *66*, 52802.

[69] T. Q. Chastek, T. P. Lodge, *J. Polym. Sci. Part B Polym. Phys.* **2005**, *43*, 405.

[70] C. M. Hui, J. Pietrasik, M. Schmitt, C. Mahoney, J. Choi, M. R. Bockstaller, K. Matyjaszewski, *Chem. Mater.* **2014**, *26*, 745.

[71] M. Brust, M. Walker, D. Bethell, D. J. Schiffrin, R. Whyman, *Chem. Commun.* **1994**, 801.

[72] R. J. Roe, *Macromolecules* **1981**, *1091*, 1091.

[73] T. R. Society, R. Society, P. Sciences, *Met. Phys.* **1973**, *335*, 191.

[74] D. McLean, *Grain Boundaries in Metals*, Oxford, **1957**.

[75] C. E. Eastman, T. P. Lodge, *Macromolecules* **1994**, *27*, 5591.

[76] P. Lejcek, *Grain Boundary Segregation in Metals*, Springer, **2010**.

[77] T. Koga, T. Hashimoto, M. Takenaka, K. Aizawa, N. Amino, M. Nakamura, D. Yamaguchi, S. Koizumi, *Macromolecules* **2008**, *41*, 453.

9. Appendix

9.1 Grain map

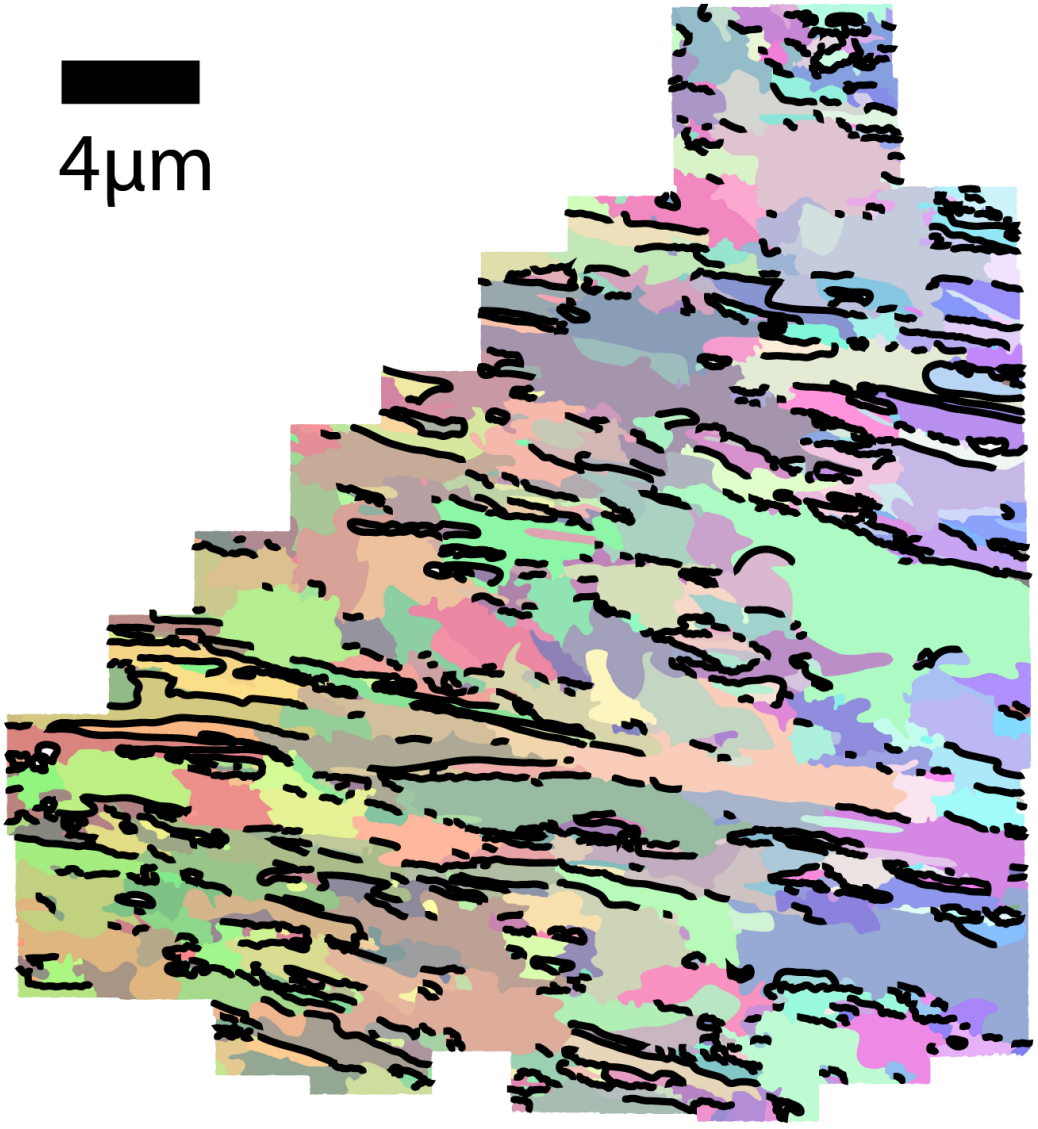

Grain map of PS-PI/d-PS 10wt% as cast overlaid with high angle grain boundary map (scale bar = 4µm)

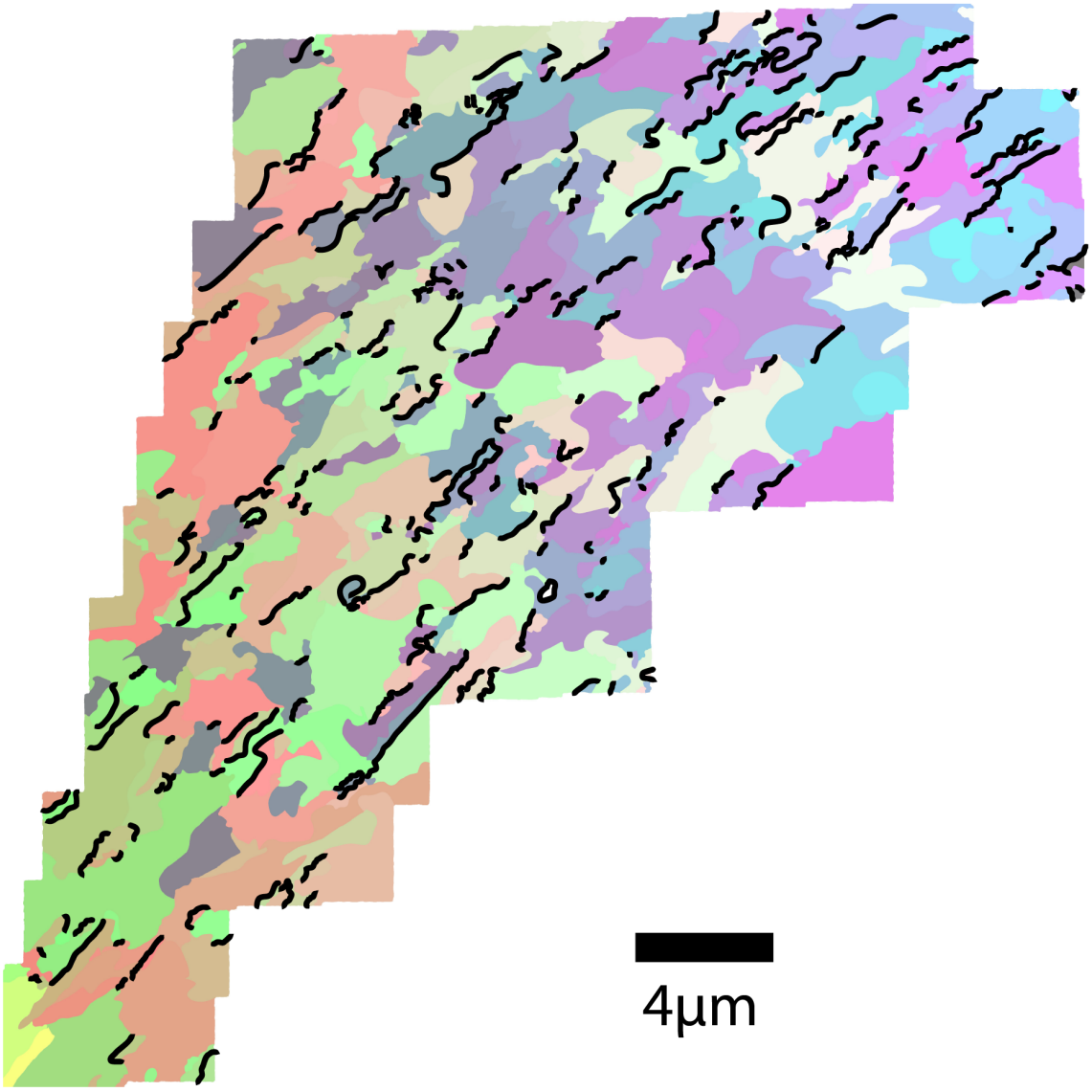

Grain map of PS-PI/d-PS 10wt% thermally annealed at 130C for 3 hours overlaid with high angle grain boundary map (scale bar = 4μm)

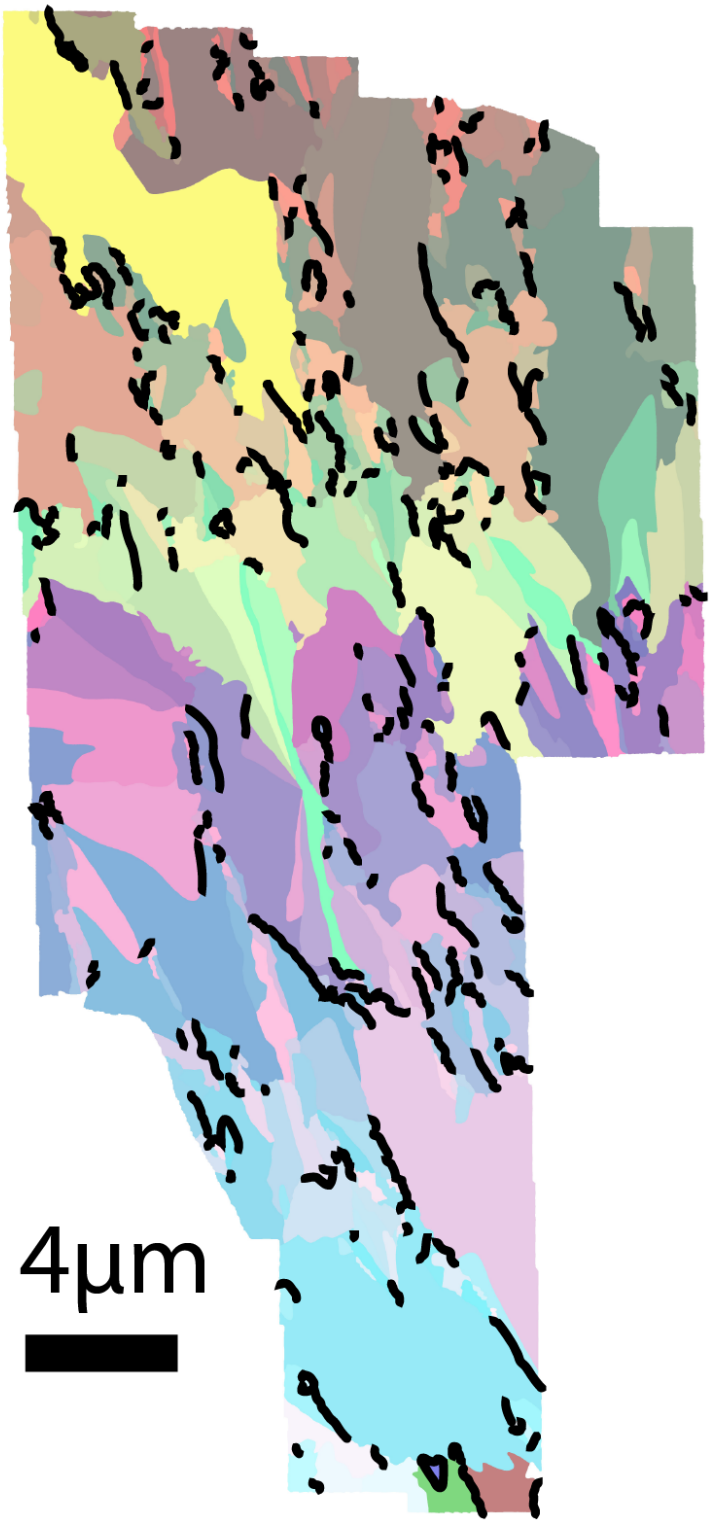

Grain map of PS-PI/d-PS 10wt% thermally annealed at 130C for 24 hrs overlaid with high angle grain boundary map (scale bar = 4µm)

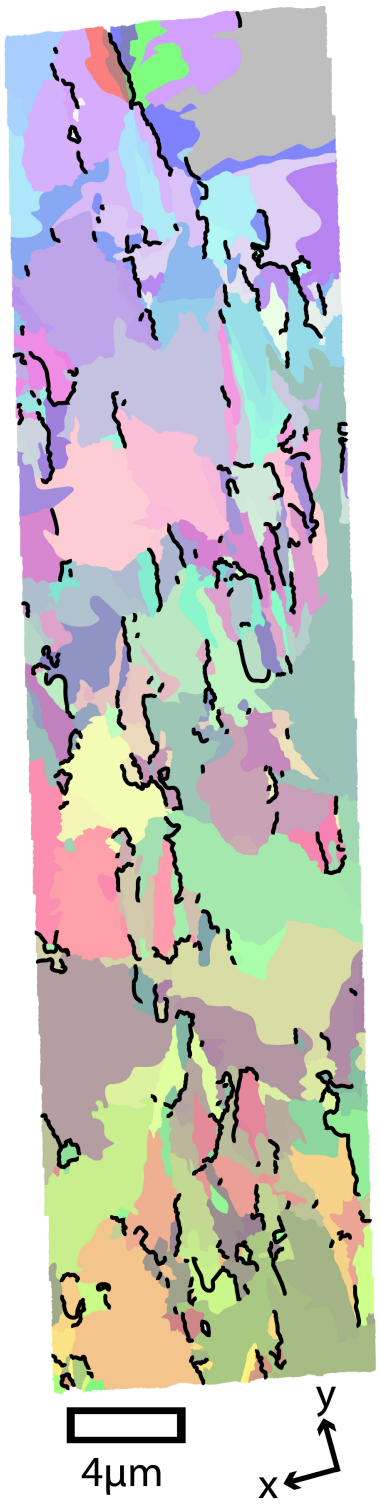

Grain map of PS-PI/d-PS 10wt% thermally annealed at 130C for 3 days overlaid with high angle grain boundary map (scale bar = 4µm)

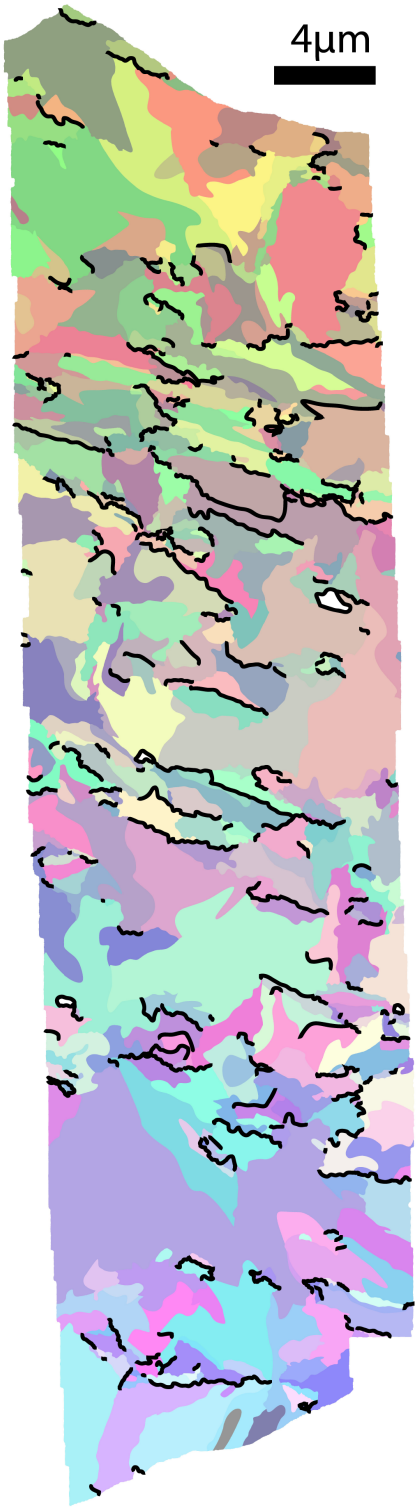

Grain map of PS-PI/d-PS 10wt% thermally annealed at 130C for 7 days overlaid with high angle grain boundary map (scale bar = 4µm)

9.2 Raw USANS data

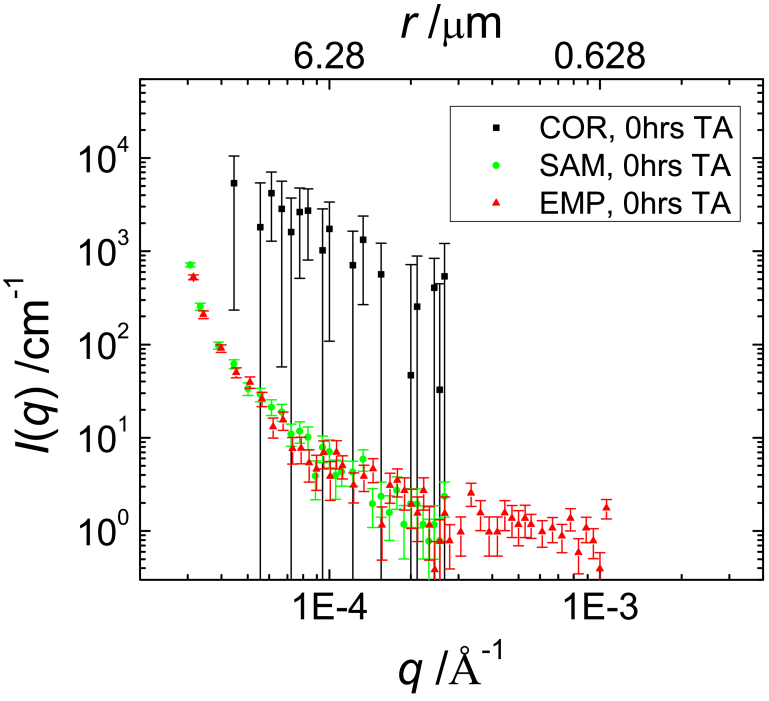

Plot of raw USANS data (Sample, Empty, Corrected) of PS-PI/d-PS 10wt% as-cast. (SAM, EMP are in arbitrary unit)

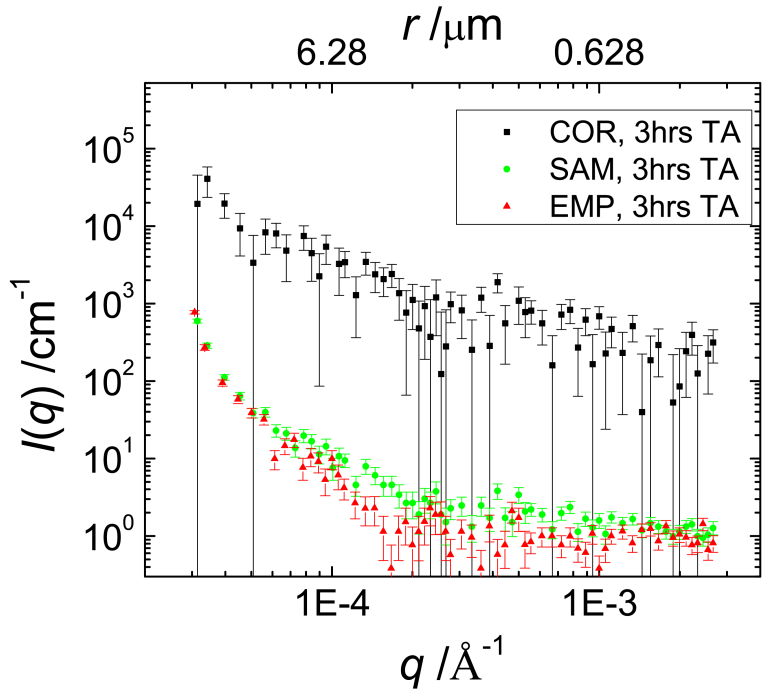

Plot of raw USANS data (Sample, Empty, Corrected) of PS-PI/d-PS 10wt% annealed at 130°C for 3hrs (SAM, EMP are in arbitrary unit)

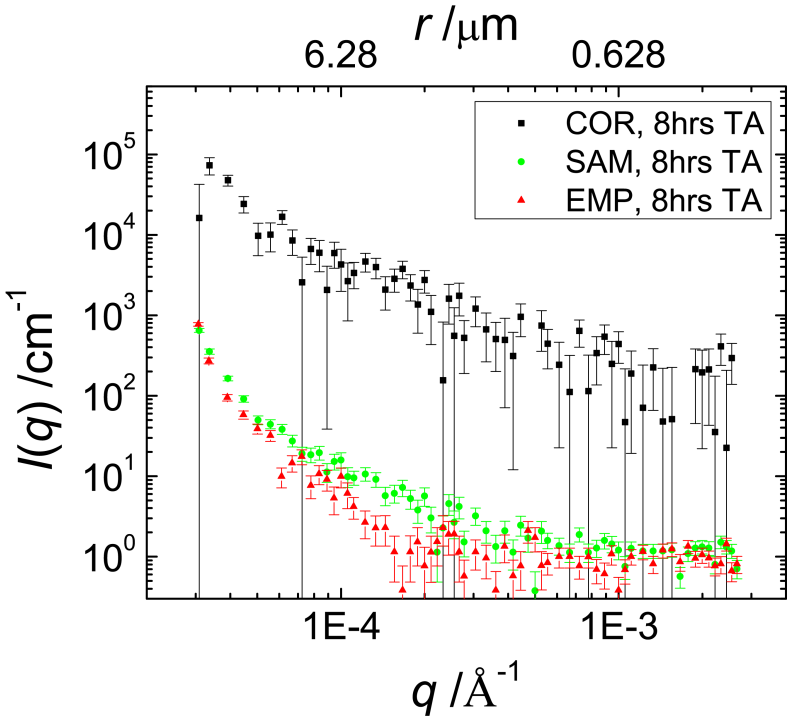

Plot of raw USANS data (Sample, Empty, Corrected) of PS-PI/d-PS 10wt% annealed at 130°C for 8hrs (SAM, EMP are in arbitrary unit)

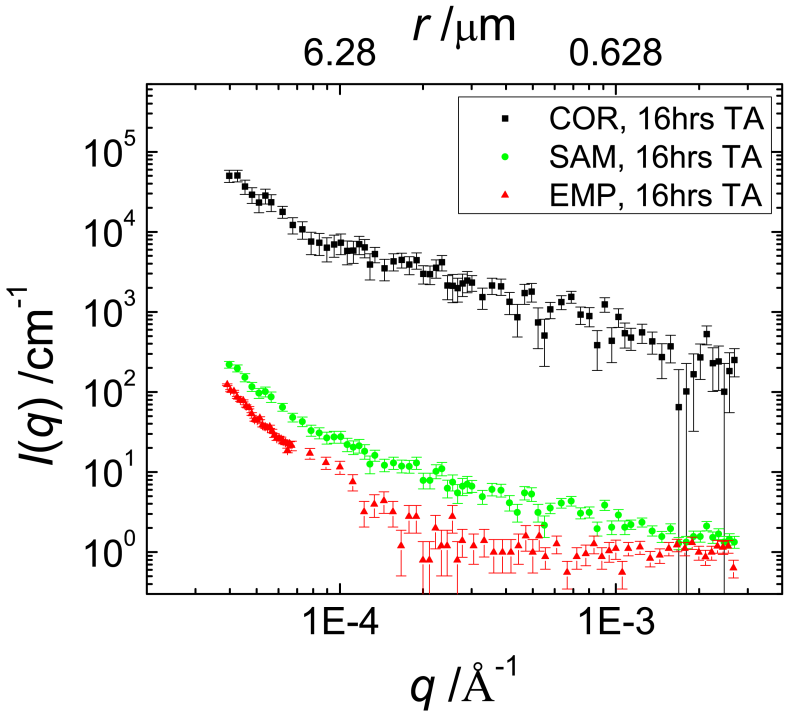

Plot of raw USANS data (Sample, Empty, Corrected) of PS-PI/d-PS 10wt% annealed at 130°C for 16hrs (SAM, EMP are in arbitrary unit)

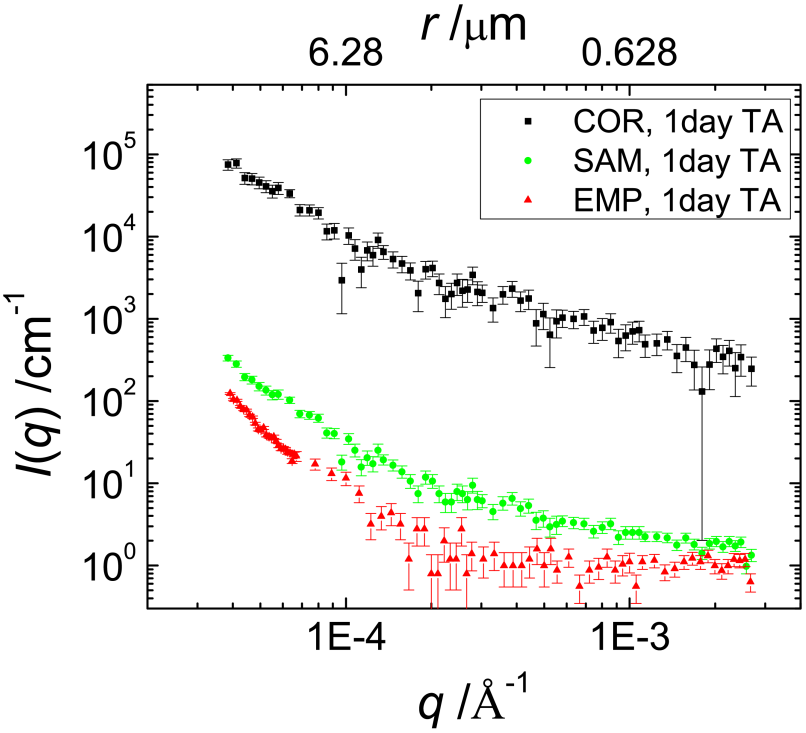

Plot of raw USANS data (Sample, Empty, Corrected) of PS-PI/d-PS 10wt% annealed at 130°C for 24hrs (1day) (SAM, EMP are in arbitrary unit)

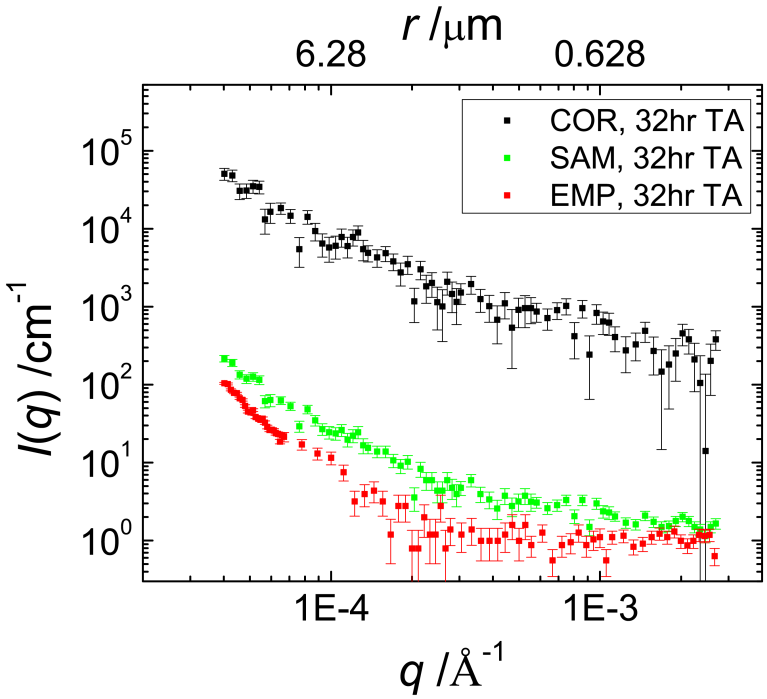

Plot of raw USANS data (Sample, Empty, Corrected) of PS-PI/d-PS 10wt% annealed at 130°C for 32hrs (SAM, EMP are in arbitrary unit)

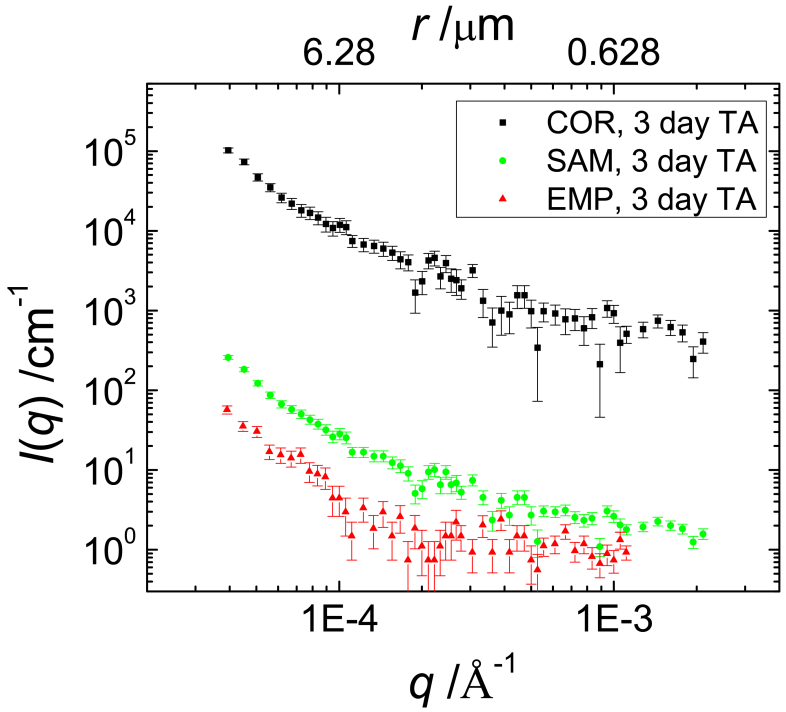

Plot of raw USANS data (Sample, Empty, Corrected) of PS-PI/d-PS 10wt% annealed at 130°C for 72hrs (3days). (SAM, EMP are in arbitrary unit)

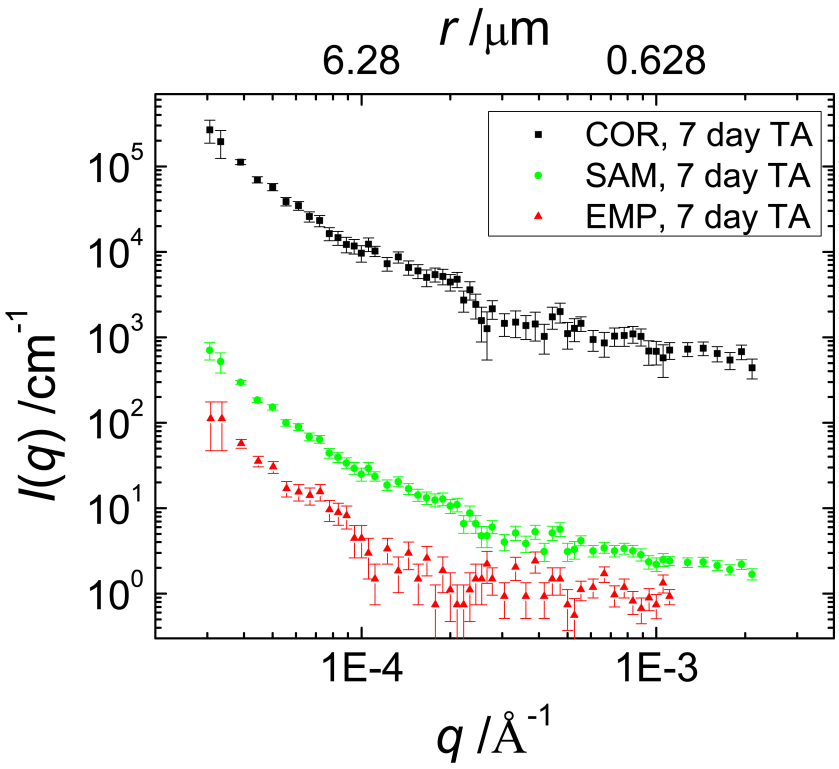

Plot of raw USANS data (Sample, Empty, Corrected) of PS-PI/d-PS 10wt% annealed at 130°C for 168hrs (SAM, EMP are in arbitrary unit)

9.3 Thermal density fluctuation

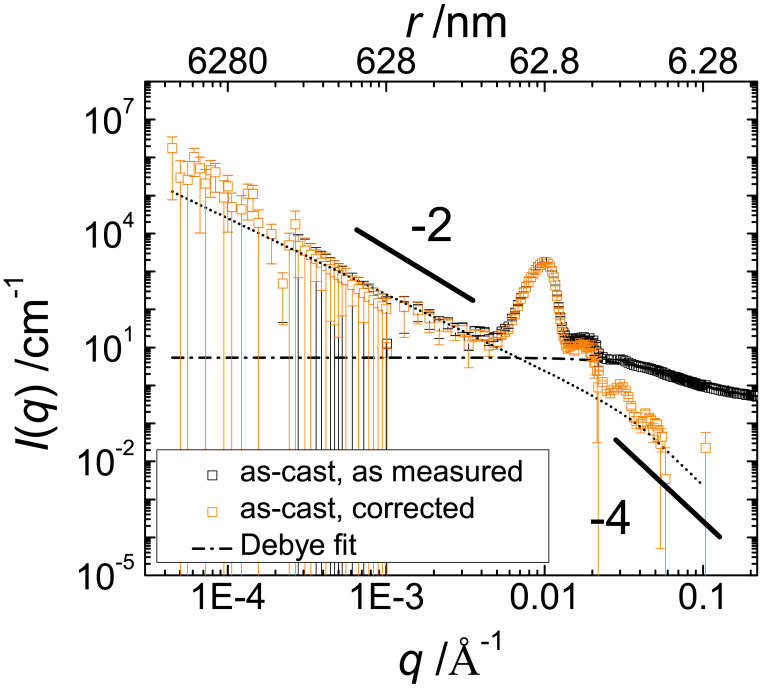

As-measured USANS/SANS and Debye corrected USANS/SANS of PS-PI/d-PS 10wt% as-cast sample . The dash-dot line shows the Debye fit.

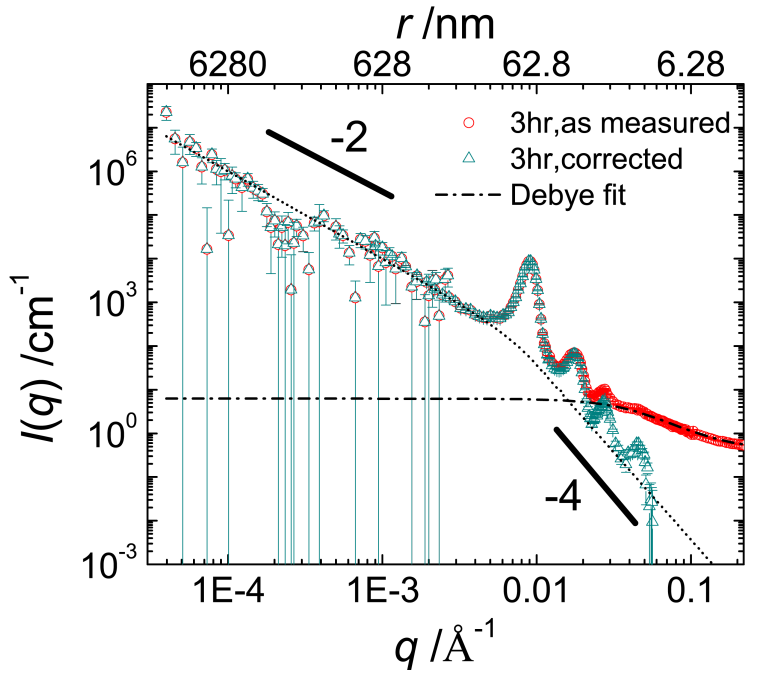

As-measured USANS/SANS and Debye corrected USANS/SANS of PS-PI/d-PS 10wt% 130°C 3hr annealed sample. The dash-dot line shows the Debye fit.

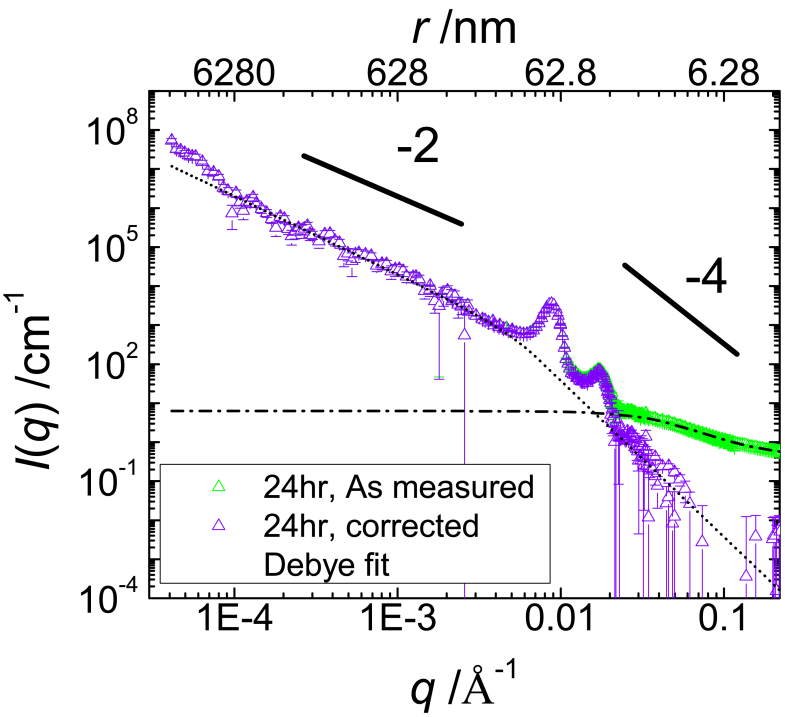

As-measured USANS/SANS and Debye corrected USANS/SANS of PS-PI/d-PS 10wt% 130°C 24hr annealed sample. The dash-dot line shows the Debye fit.

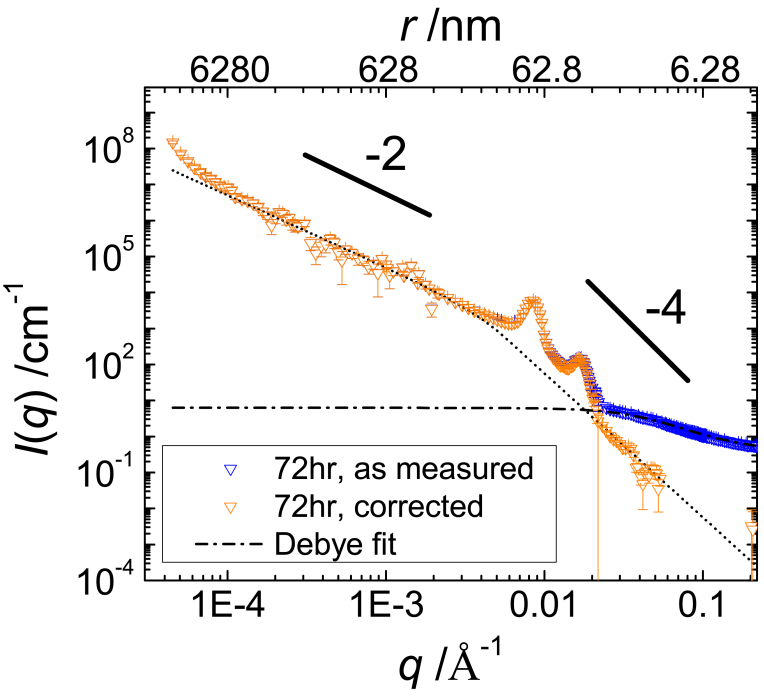

As-measured USANS/SANS and Debye corrected USANS/SANS of PS-PI/d-PS 10wt% 130°C 72hr (3day) annealed sample. The dash-dot line shows the Debye fit.

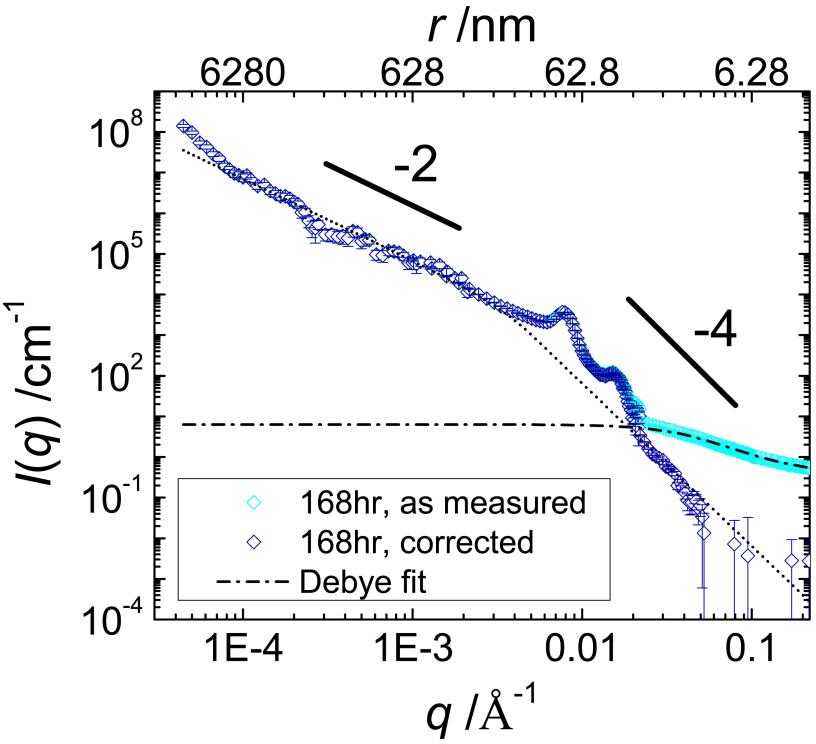

As-measured USANS/SANS and Debye corrected USANS/SANS of PS-PI/d-PS 10wt% 130°C 168hr (7day) annealed sample. The dash-dot line shows the Debye fit.

9.4 *SLD* of grain boundary, grain and Δ*SLD*

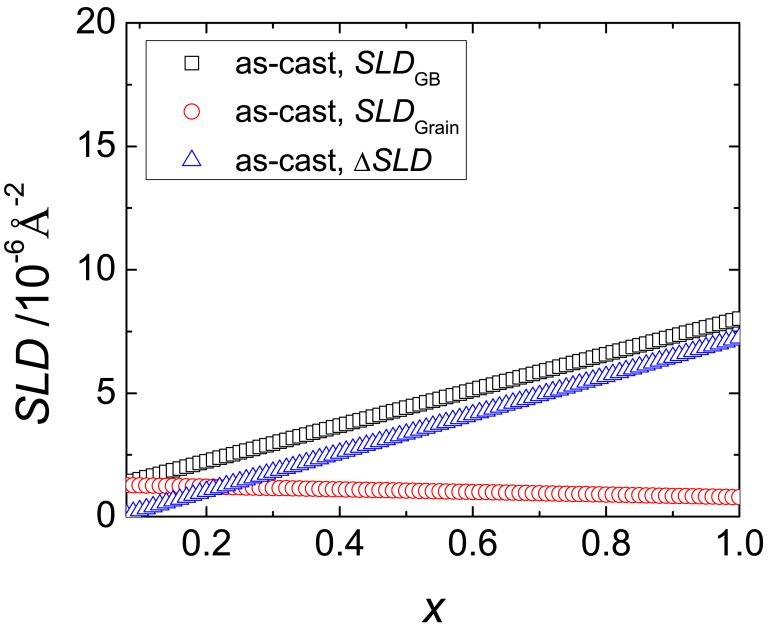

SLD of grain boundary, grain and Δ*SLD* of PS-PI/d-PS 10wt% as-cast sample as a function of total volume fraction of d-PS segregated to HAGB (*x*)

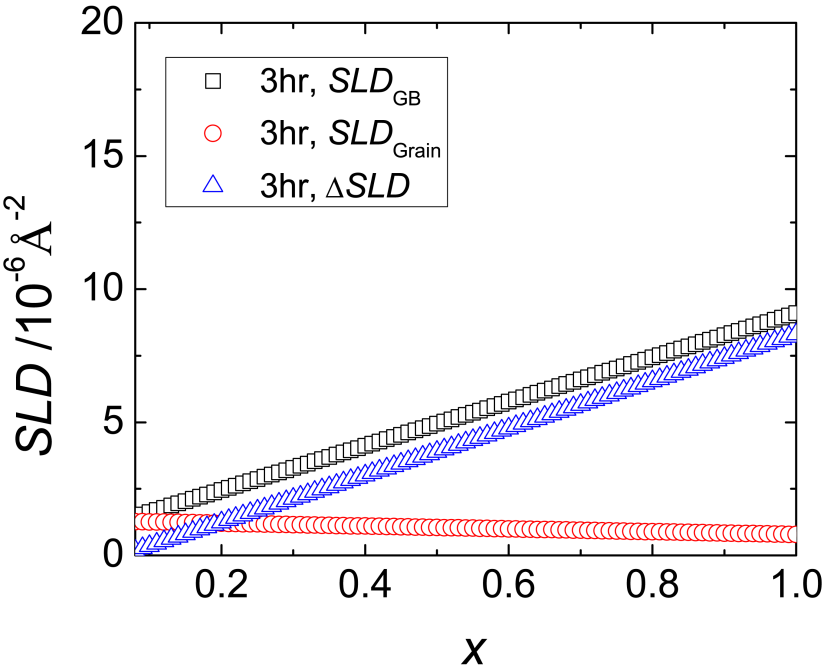

SLD of grain boundary, grain and Δ*SLD* of PS-PI/d-PS 10wt% 130°C 3hr annealed sample as a function of total volume fraction of d-PS segregated to HAGB (*x*)

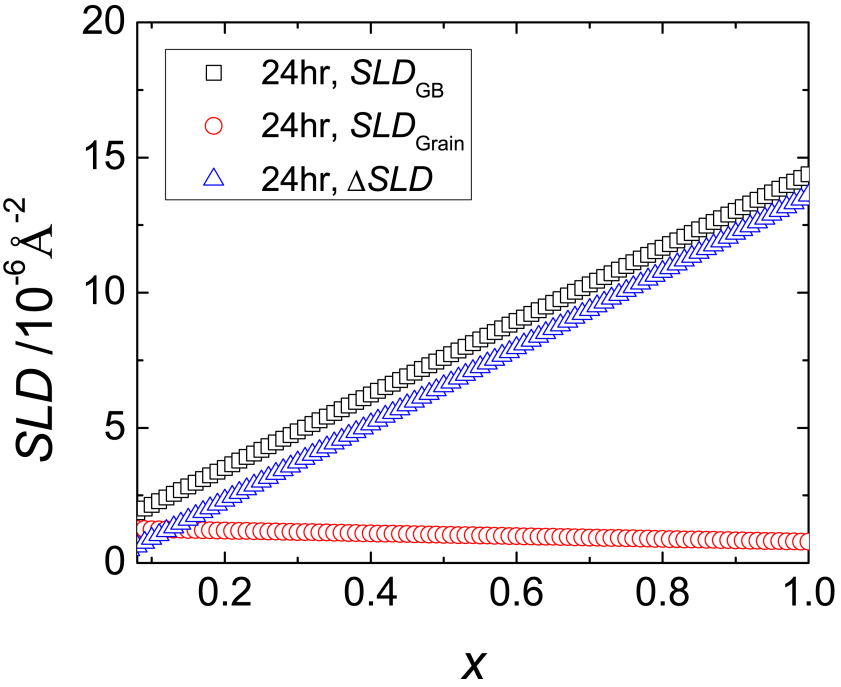

SLD of grain boundary, grain and Δ*SLD* of PS-PI/d-PS 10wt% 130°C 24hr annealed sample as a function of total volume fraction of d-PS segregated to HAGB (*x*)

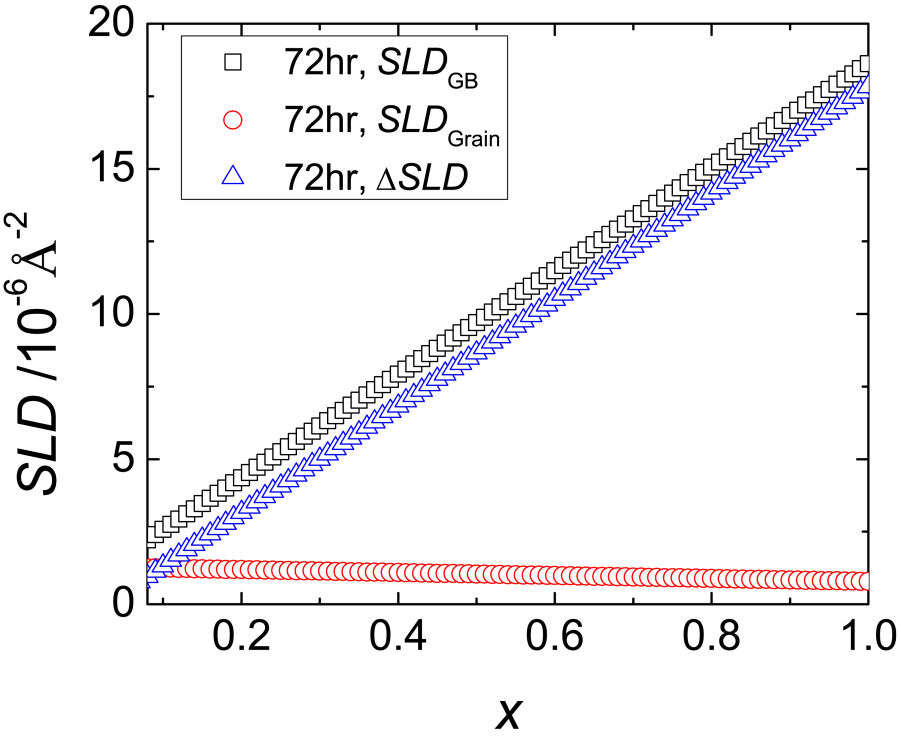

SLD of grain boundary, grain and Δ*SLD* of PS-PI/d-PS 10wt% 130°C 72hr annealed sample as a function of total volume fraction of d-PS segregated to HAGB (*x*)

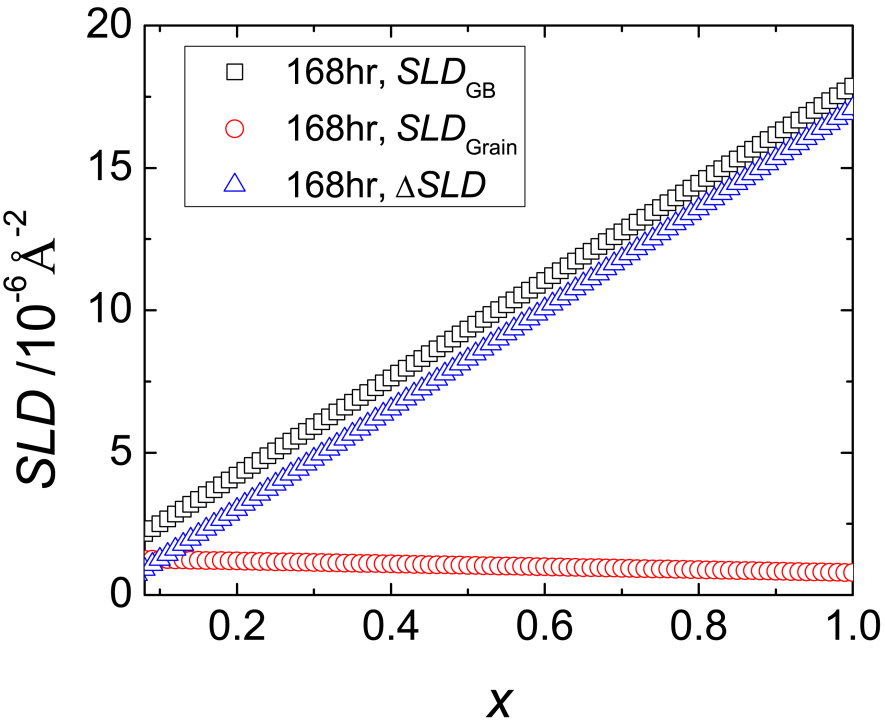

SLD of grain boundary, grain and Δ*SLD* of PS-PI/d-PS 10wt% 130°C 3hr annealed sample as a function of total volume fraction of d-PS segregated to HAGB (x)

9.5 MATLAB code

All the MATLAB codes were developed by Hyungju Ryu.

Calculate Orientation of Lamellae

```
tic % opening an image
sample_name=strcat('XXXXXXXXXX'); file_name=strcat(sample_name,'.jpg');
ImageMaster=imread(file_name);
bw=im2bw(ImageMaster,graythresh(ImageMaster)); bw_inv=~bw;
bw_inv=bwareaopen(bw_inv,3);
for times=1:5
   bw_inv=bwmorph(bw_inv,'skel',1); bw_inv=bwmorph(bw_inv,'close');
end
bw_inv=bwmorph(bw_inv,'skel',Inf);
% generating a modified image for the analysis
ACell=32; margin=floor(ACell/2);
a=size(bw,1); b=size(bw,2); bw_mod=zeros(a+ACell,b+ACell);
bw_mod(margin+1:margin+a,margin+1:margin+b)=bw_inv;
% hough transform from each cell and getting distance and angle
Angle_prev(a,b)=0;
clear('ImageMaster','bw','bw_inv','margin','times');
matlabpool
parfor i=1:a*b
   [r,c]=ind2sub([a,b],i);
   bw_hough=bw_mod(r:(r-1)+ACell,c:(c-1)+ACell,:);
   if size(find(bw_hough==1)) < round(ACell/3)
      Angle_prev(i)=NaN; continue
   end
   bw_hough=imresize(bw_hough,5);
   bw_fft=abs(fftshift(fft2(bw_hough))); x=[]; y=[];
   bw_fft(bw_fft==max(max(bw_fft)))=-100;
   bw_fft(bw_fft==max(max(bw_fft)))=-100;
   bw_fft(bw_fft==max(max(bw_fft)))=-100;
   [y x]=find(bw_fft==-100);
   if size(unique(x),1)==1
      Angle_prev(i)=Inf;
   else
      p=polyfit(x,y,1);
      Angle_prev(i)=90-rad2deg(atan(p(1)));
   end
end
matlabpool close
clear('y','x','bw_hough','bw_fft','x','r','c','bw_mod')
%
Angle=Angle_prev; Angle=round(Angle);
Angle(Angle==180)=0; nan_position=isnan(Angle); nan_matrix=ones(size(Angle));
nan_position1=bwareaopen(nan_position,100001);
nan_position=nan_position-nan_position1;
nan_matrix(nan_position==1)=0;
[~,dist2]=bwdist_old(nan_matrix); Angle(:)=Angle(dist2(:));
clear('nan_matrix','conn','label','nan_position','coor','nan_position1','dist2');
```

```
%
A=isinf(Angle); conn=bwconncomp(A); label=labelmatrix(conn);
for i=1:max(max(label))
   [y_coor x_coor]=find(label==i);
   y_max=min(max(y_coor)+20,size(Angle,1)); y_min=max(min(y_coor)-20,1);
   x_max=min(max(x_coor)+20,size(Angle,2)); x_min=max(min(x_coor)-20,1);
   AA=Angle(y_min:y_max, x_min:x_max);
   A1=label(y_min:y_max, x_min:x_max);
   near= bwdist_old(A1==i)<=sqrt(2) & bwdist_old(A1==i)>0;
   num_mod=mode(AA(near));
   if num_mod >= 90
      Angle(label==i)=180;
   else
      Angle(label==i)=0;
   end
end
clear('y_coor','x_coor','y_max','y_min','x_max','x_min','AA','A1','near',...
   'num_mod')
% save a data file
cell_size=num2str(ACell);
cell_name=strcat(sample_name,'_Set_Angle_cell_',cell_size,'_v10_pixel_fft_corrected.mat');
save(cell_name, 'Angle_prev','ACell','Angle','file_name','sample_name');
toc
save('XXXXXXX.mat');
```

Grain map construction

```
tic;
clear('ALatitude','Angle_prev','Distance','Distance_prev','Distance_prev1',...
   'dist_min');
% cleaning boudary area
Angle_mod=Angle;
se=strel('disk',15);
nan_loc=isnan(Angle_mod); nan_loc=imdilate(nan_loc,se);
Angle_mod(nan_loc==1)=NaN;
clear('se','nan_loc')
% removing 0 and 180 degree
Angle2=Angle;
Angle2(Angle2==0)=NaN; Angle2(Angle2==180)=NaN;
Angle5=Angle;
Angle5(Angle5==0)=max(min(min(Angle2))-1,0.1);
Angle5(Angle5==180)=min(max(max(Angle2))+1,179.9);
clear('Angle2')
% excluding image boundary areas since FFT results might be biased
Angle5(isnan(Angle_mod))=NaN;
% generating a grain map
[label2 Angle1 grad grain_seg]=grainmap(Angle5, 15);
% remove small grains
mini_size=mini_grain(label2,0,3000);
A=label2~=0; A=bwareaopen(A,mini_size);
conn=bwconncomp(A); grain_lab=labelmatrix(conn);
[~,dist2]=bwdist_old(grain_lab); grain_lab(:)=grain_lab(dist2(:));
grain_lab(isnan(Angle5))=0;
% rearray the grain numbers again
non_zero=grain_lab~=0;
```

```
[~, ~, uni2]=unique(grain_lab(non_zero)); uni4=(1:numel(uni2))';
grain_lab(non_zero)=uni4(uni2);
clear('A','conn','dist2','non_zero','uni2','uni4')

% merging grains smaller than specific size
grain_lab2=smgrain_merge(grain_lab,Angle1,38000);
% rearray the grain numbers again
non_zero=grain_lab2~=0;
[~, ~, uni2]=unique(grain_lab2(non_zero)); uni4=(1:numel(uni2))';
grain_lab2(non_zero)=uni4(uni2);
clear('non_zero','uni2','uni4')

% removing island grains
grain_lab3=remove_island(grain_lab2);
% smoothing gbs
grain_gb=gb_map(grain_lab3);
% obtaining a grainp map from smoothed gb map
se=strel('disk',1);
A=grain_gb; A=imdilate(A,se);
A=~A; A(isnan(Angle5))=0; A=bwareaopen(A,500);
conn=bwconncomp(A); grain_lab4=double(labelmatrix(conn));
[~,dist2]=bwdist_old(grain_lab4); grain_lab4(:)=grain_lab4(dist2(:));
grain_lab4(isnan(Angle5))=0;
clear('A','dist2','conn','se');

%%%%%%%%%%%%  SAVE FILE HERE
%%%%%%%%%%%%%%%%%%%%%%%%%%%%%%%%%%%%%%%%%%%%

clear('grain_lab','grain_lab1','grain_lab3','grain_seg','label2',...
   'grad','grain_gb','grain_lab2','label3','Angle','Angle5','Angle_mod')

TEM_ratio=0.2/49; %changed from 39 to 49 by BJ
gb_area=zeros(max(max(grain_lab4)),4);
for i=1:max(max(grain_lab4))
   gb_area(i,2)=size(find(grain_lab4==i),1);
   gb_area(i,1)=i;
   gb_area(i,3)=gb_area(i,2)*TEM_ratio^2;
   gb_area(i,4)=gb_area(i,3)*gb_area(i,3);
end


% MEASURING GB orientation
GB_orien=gb_ori_BJ_2014_06_24(grain_lab4); %BJ, changed from gb_ori
[GB_tilt GB_symm]=gb_tilt(grain_lab4,GB_orien,Angle1);

se=strel('disk',3);
GB_tilt_show=imdilate(GB_tilt,se);
GB_symm_show=imdilate(GB_symm,se);

high_gb=GB_tilt_show > 90;
L=zeros(a,b,3); L(:,:,1)=high_gb; L(:,:,2)=high_gb; L(:,:,3)=high_gb;
L=im2uint8(L);
imwrite(L,XXXXXXX.jpg'); clear('high_gb')
```

```
low_gb=GB_tilt_show <= 90 & GB_tilt_show > 0;
L=zeros(a,b,3); L(:,:,1)=low_gb; L(:,:,2)=low_gb; L(:,:,3)=low_gb;
L=im2uint8(L);
imwrite(L,’XXXXXXX.jpg'); clear('low_gb','GB_tilt_show')

symm_gb=GB_symm_show==1;
L=zeros(a,b,3); L(:,:,1)=symm_gb; L(:,:,2)=symm_gb; L(:,:,3)=symm_gb;
L=im2uint8(L);
imwrite(L,’XXXXXXX.jpg'); clear('symm_gb')

asymm_gb=GB_symm_show==2;
L=zeros(a,b,3); L(:,:,1)=asymm_gb; L(:,:,2)=asymm_gb; L(:,:,3)=asymm_gb;
L=im2uint8(L);
imwrite(L,’XXXXXXX.jpg');
clear('asymm_gb','GB_symm_show','se','L','overlaid','file_name','I');

%%%%%%%%%%%%%%%%%%%%%%%% MEASURING PARAMETERS
%%%%%%%%%%%%%%%%%%%%%%%%%%
AA_1_gb_area_number_avg=sum(gb_area(:,3))/max(max(grain_lab4));
AA_2_gb_area_weighted_avg=sum(gb_area(:,4))/sum(gb_area(:,3));
AA_3_high_gb_ratio=size(find(GB_tilt > 90),1) / size(find(GB_tilt~=0),1);
AA_4_low_gb_ratio=size(find(GB_tilt <= 90 & GB_tilt >0),1) / size(find(GB_tilt~=0),1);
AA_5_T_junc_ratio=size(find(GB_symm==2),1) / size(find(GB_symm~=0),1);
AA_6_GB_density=size(find(GB_symm~=0),1) / sum(gb_area(:,2));
%%%%%%%%%%%%%%%%%%%%%%%%%%%%%%%%%%%%%%%%%%%%%%%%%%%
%%%%%%%%%%%%%%%%%%%%%%
Grain_orimap=zeros(size(Angle1));
for i=1:max(max(grain_lab4))
   Grain_orimap(grain_lab4==i)=median(Angle1(grain_lab4==i));
end
%%%%%%%%%%%%%%%%%%%%%%%%%%%%%%%%%%%%%%%%%%%%%%%%%%%
%%%%%%%%%%%%%%%%%%%%%%
% removing 180 degree from GB_orien
GB_orien2=GB_orien;
GB_orien2(GB_orien2==180)=0;
GB_ori=GB_orien2(~isnan(GB_orien2));
GB_ori_median=median(GB_ori);
clear('GB_orien2')
% GB_orien of high angle GBs
GB_orien2=GB_orien;
GB_orien2(GB_orien2==180)=0;
GB_orien2(GB_tilt <= 90)=NaN;
GB_ori_high=GB_orien2(~isnan(GB_orien2));
GB_ori_high_median=median(GB_ori_high);
clear('GB_orien2')
% GB_orien of low angle GBs
GB_orien2=GB_orien;
GB_orien2(GB_orien2==180)=0;
GB_orien2(GB_tilt > 90)=NaN;
GB_ori_low=GB_orien2(~isnan(GB_orien2));
GB_ori_low_median=median(GB_ori_low);
clear('GB_orien2')
%%%%%%%%%%%%%%%%%%%%%%%%%%%%%%%%%%%%%%%%%%%%%%%%%%%
%%%%%%%%%%%%%%%%%%%%%%%
Misorientation=GB_tilt(GB_tilt~=0);
```

```
%%%%%%%%%%%%%%%%%%%%%%%%%%%%%%%%%%%%%%%%%%%%%%%%%%%
%%%%%%%%%%%%%%%%%%%%%%%%
% aspect ratio of grains
[Anisotropic Anisotropic_avg]=aspect_ratio(grain_lab4);

[Aniso_sel Aniso_avg_sel]=aspect_ratio_selec(grain_lab4,gb_area,0.03,10);
%%%%%%%%%%%%%%%%%%%%%%%%%%%%%%%%%%%%%%%%%%%%%%%%%%%
%%%%%%%%%%%%%%%%%%%%%%%%%%%%
% GB Energy
[Triple_junc Triple_sorted]=triple(grain_lab4,GB_tilt);

GB_E=gbenergy(Triple_sorted,20);

[Triple_junc1 Triple_sorted1]=triple_1(grain_lab4,GB_tilt);

GB_E1=gbenergy(Triple_sorted1,20);

toc

save(‘XXXXXXX.mat');
```

gb_map.m

```
function X=gb_map(A)

grain_near_number{max(max(A))}=[];
for i=1:max(max(A))
    [y_coor x_coor]=find(A==i);
    y_max=min(max(y_coor)+10,size(A,1)); y_min=max(min(y_coor)-10,1);
    x_max=min(max(x_coor)+10,size(A,2)); x_min=max(min(x_coor)-10,1);
    location1=A(y_min:y_max, x_min:x_max);
    near= bwdist_old(location1==i)<=sqrt(2) & bwdist_old(location1==i)>0;
    grain_near_number{i}=unique(location1(near));
    grain_near_number{i}(grain_near_number{i}==0)=[];
end
for i=1:max(max(A))
    if size(grain_near_number{i},2)==0
        continue
    else
        for j=1:size(grain_near_number{i},1)
            grain_num=grain_near_number{i}(j);
            grain_near_number{grain_num}(grain_near_number{grain_num}==i)=[];
        end
    end
end
clear('y_coor','x_coor','y_max','y_min','x_min','x_max','location1','near',...
    'grain_num')

A_gb=zeros(size(A)); se=strel('disk',1); se1=strel('disk',3);
h=waitbar(0,'Please be patient...');
for i=1:max(max(A))
```

```
if size(grain_near_number{i},2)==0
   continue
end
size_1=size(find(A==i),1);
for j=1:size(grain_near_number{i},1)
   size_2=size(find(A==grain_near_number{i}(j)),1);
   if size_1 <= size_2
      [y_coor x_coor]=find(A==i);
      y_max=min(max(y_coor)+100,size(A,1)); y_min=max(min(y_coor)-100,1);
      x_max=min(max(x_coor)+100,size(A,2)); x_min=max(min(x_coor)-100,1);
      location1=A(y_min:y_max, x_min:x_max);
   else
      [y_coor x_coor]=find(A==grain_near_number{i}(j));
      y_max=min(max(y_coor)+100,size(A,1)); y_min=max(min(y_coor)-100,1);
      x_max=min(max(x_coor)+100,size(A,2)); x_min=max(min(x_coor)-100,1);
      location1=A(y_min:y_max, x_min:x_max);
   end
   % finding original GBs
   location2=zeros(size(location1));
   location2(location1==i)=1; location2(location1==grain_near_number{i}(j))=2;
   near= bwdist_old(location2==2)<=sqrt(2) & bwdist_old(location2==2)>0;
   location2(near)=location2(near)+2;
   conn=bwconncomp(bwareaopen(location2==3,4)); label=labelmatrix(conn);
   for k=1:max(max(label))
      AAA=bwmorph(label==k,'skel',inf);
      A1=bwmorph(AAA,'endpoints');
      [yyy1 xxx1]=find(A1==1);
      for m=1:length(yyy1)
         if AAA(yyy1(m),xxx1(m))==0
            AAA(yyy1(m),xxx1(m))=1;
         end
      end
      % finding "two" endpoints
      if length(yyy1)> 2
         num_el=linspace(1,length(yyy1),length(yyy1));
         com_el=combnk(num_el,2);
         length_el=zeros(length(com_el),2);
         for m=1:length(com_el)
            yy_1=yyy1(com_el(m,1)); yy_2=yyy1(com_el(m,2));
            xx_1=xxx1(com_el(m,1)); xx_2=xxx1(com_el(m,2));
            BB=bwtraceboundary(AAA,[yy_1 xx_1],'W',8,inf,'clockwise');
            coor1=find(BB(:,1)==yy_2 & BB(:,2)==xx_2);
            BB1=bwtraceboundary(AAA,[yy_1 xx_1],'W',8,inf,'counterclockwise');
            coor2=find(BB1(:,1)==yy_2 & BB1(:,2)==xx_2);
            if coor1 >= coor2
               BB1(coor2+1:end, :)=[];
               length_el(m,1)=length(BB1);
            else
               BB(coor1+1:end,:)=[];
               length_el(m,1)=length(BB);
            end
            length_el(m,2)=m;
         end
         length_el=sortrows(length_el,-1);
         num_i=length_el(1,2);
         coor=zeros(2,2);
```

```
coor(1,1)=xxx1(com_el(num_i,1));
coor(1,2)=yyy1(com_el(num_i,1));
coor(2,1)=xxx1(com_el(num_i,2));
coor(2,2)=yyy1(com_el(num_i,2));
coor=sortrows(coor); clear('xxx1','yyy1')
xxx1(1)=coor(1,1); yyy1(1)=coor(1,2);
xxx1(2)=coor(2,1); yyy1(2)=coor(2,2);
clear('num_el','com_el','length_el','yy_1','yy_2','xx_1',...
   'xx_2','BB','coor1','BB1','coor2','coor')
dist=sqrt((xxx1(1)-xxx1(2))^2 + ((yyy1(1)-yyy1(2))^2));
B=bwtraceboundary(label==k,[yyy1(1) xxx1(1)],'E');
coor=find(B(:,1)==yyy1(2) & B(:,2)==xxx1(2));
B(coor+1:end,:)=[];
yy=B(:,1); xx=B(:,2);
t=1:length(yy);
if length(t)/dist < 1.5
   xs=round(smooth(t,xx,0.3,'loess'));
   ys=round(smooth(t,yy,0.3,'loess'));
else
   xs=round(smooth(t,xx,0.5,'loess'));
   ys=round(smooth(t,yy,0.5,'loess'));
end
move_1=yy(1)-ys(1); ys=ys+move_1;
move_2=xx(1)-xs(1); xs=xs+move_2;
x1=xx-xx(1); y1=yy-yy(1);
x2=xs-xx(1); y2=ys-yy(1);
slope_ori=y1(end)/x1(end);
if y1(end)>0 && x1(end)>0
   theta1=atan(slope_ori);
elseif y1(end)>0 && x1(end)<0
   theta1=pi+atan(slope_ori);
elseif y1(end)<0 && x1(end)<0
   theta1=pi+atan(slope_ori);
elseif y1(end)<0 && x1(end)>0
   theta1=2*pi+atan(slope_ori);
elseif y1(end)==0
   theta1=0;
elseif x1(end)==0 && y1(end) > 0
   theta1=deg2rad(90);
elseif x1(end)==0 && y1(end) < 0
   theta1=deg2rad(270);
end
slope_smo=y2(end)/x2(end);
if y2(end)>0 && x2(end)>0
   theta2=atan(slope_smo);
elseif y2(end)>0 && x2(end)<0
   theta2=pi+atan(slope_smo);
elseif y2(end)<0 && x2(end)<0
   theta2=pi+atan(slope_smo);
elseif y2(end)<0 && x2(end)>0
   theta2=2*pi+atan(slope_smo);
elseif y2(end)==0
   theta2=0;
elseif x2(end)==0 && y2(end) > 0
   theta2=deg2rad(90);
elseif x2(end)==0 && y2(end) < 0
```

```
    theta2=deg2rad(270);
end
theta=theta2-theta1;
if theta1 < theta2
    xxx=round(cos(-theta)*x2 - sin(-theta)*y2);
    yyy=round(sin(-theta)*x2 + cos(-theta)*y2);
else
    xxx=round(cos(-theta)*x2 - sin(-theta)*y2);
    yyy=round(sin(-theta)*x2 + cos(-theta)*y2);
end
xxx=xxx+xx(1); yyy=yyy+yy(1);
location3=zeros(size(location2));
for m=1:length(yyy)
    if yyy(m) > size(location2,1)
        yyy(m)=size(location2,1);
    elseif yyy(m)<=0
        yyy(m)=1;
    end
    if xxx(m) > size(location2,2)
        xxx(m)=size(location2,2);
    elseif xxx(m) <= 0
        xxx(m)=1;
    end
    location3(yyy(m),xxx(m))=1;
end
if xxx(end)~=xxx1(2) || yyy(end)~=yyy1(2)
    x_size=abs(xxx(end)-xxx1(2))+1;
    y_size=abs(yyy(end)-yyy1(2))+1;
    if x_size >= y_size
        if xxx(end) <= xxx1(2)
            x_start=xxx(end); x_end=xxx1(2);
            y_start=yyy(end); y_end=yyy1(2);
        else
            x_start=xxx1(2); x_end=xxx(end);
            y_start=yyy1(2); y_end=yyy(end);
        end
        x_coor=(x_start:1:x_end);
        y_coor=round(interp1([x_start x_end],[y_start y_end],x_coor));
        coor=[y_coor' x_coor'];
    else
        if yyy(end) <= yyy1(2)
            y_start=yyy(end); y_end=yyy1(2);
            x_start=xxx(end); x_end=xxx1(2);
        else
            y_start=yyy1(2); y_end=yyy(end);
            x_start=xxx1(2); x_end=xxx(end);
        end
        y_coor=(y_start:1:y_end);
        x_coor=round(interp1([y_start y_end],[x_start x_end],y_coor));
        coor=[y_coor' x_coor'];
    end
    for m=1:length(coor)
        location3(coor(m,1),coor(m,2))=1;
    end
end
location3=imdilate(location3,se);
```

```
    AA=zeros(size(A));
    AA(y_min:y_max, x_min:x_max)=location3;
    A_gb(AA==1)=1;
elseif length(yyy1)==2
    dist=sqrt((xxx1(1)-xxx1(2))^2 + ((yyy1(1)-yyy1(2))^2));
    B=bwtraceboundary(label==k,[yyy1(1) xxx1(1)],'E');
    coor=find(B(:,1)==yyy1(2) & B(:,2)==xxx1(2));
    B(coor+1:end,:)=[];
    yy=B(:,1); xx=B(:,2);
    t=1:length(yy);
    if length(t)/dist < 1.5
        xs=round(smooth(t,xx,0.3,'loess'));
        ys=round(smooth(t,yy,0.3,'loess'));
    else
        xs=round(smooth(t,xx,0.5,'loess'));
        ys=round(smooth(t,yy,0.5,'loess'));
    end
    move_1=yy(1)-ys(1); ys=ys+move_1;
    move_2=xx(1)-xs(1); xs=xs+move_2;
    x1=xx-xx(1); y1=yy-yy(1);
    x2=xs-xx(1); y2=ys-yy(1);
    slope_ori=y1(end)/x1(end);
    if y1(end)>0 && x1(end)>0
        theta1=atan(slope_ori);
    elseif y1(end)>0 && x1(end)<0
        theta1=pi+atan(slope_ori);
    elseif y1(end)<0 && x1(end)<0
        theta1=pi+atan(slope_ori);
    elseif y1(end)<0 && x1(end)>0
        theta1=2*pi+atan(slope_ori);
    elseif y1(end)==0
        theta1=0;
    elseif x1(end)==0 && y1(end) > 0
        theta1=deg2rad(90);
    elseif x1(end)==0 && y1(end) < 0
        theta1=deg2rad(270);
    end
    slope_smo=y2(end)/x2(end);
    if y2(end)>0 && x2(end)>0
        theta2=atan(slope_smo);
    elseif y2(end)>0 && x2(end)<0
        theta2=pi+atan(slope_smo);
    elseif y2(end)<0 && x2(end)<0
        theta2=pi+atan(slope_smo);
    elseif y2(end)<0 && x2(end)>0
        theta2=2*pi+atan(slope_smo);
    elseif y2(end)==0
        theta2=0;
    elseif x2(end)==0 && y2(end) > 0
        theta2=deg2rad(90);
    elseif x2(end)==0 && y2(end) < 0
        theta2=deg2rad(270);
    end
    theta=theta2-theta1;
    if theta1 < theta2
        xxx=round(cos(-theta)*x2 - sin(-theta)*y2);
```

```
        yyy=round(sin(-theta)*x2 + cos(-theta)*y2);
    else
        xxx=round(cos(-theta)*x2 - sin(-theta)*y2);
        yyy=round(sin(-theta)*x2 + cos(-theta)*y2);
    end
    xxx=xxx+xx(1); yyy=yyy+yy(1);
    location3=zeros(size(location2));
    for m=1:length(yyy)
        if yyy(m) > size(location2,1)
            yyy(m)=size(location2,1);
        elseif yyy(m)<=0
            yyy(m)=1;
        end
        if xxx(m) > size(location2,2)
            xxx(m)=size(location2,2);
        elseif xxx(m)<=0
            xxx(m)=1;
        end
        location3(yyy(m),xxx(m))=1;
    end
    if xxx(end)~=xxx1(2) || yyy(end)~=yyy1(2)
        x_size=abs(xxx(end)-xxx1(2))+1;
        y_size=abs(yyy(end)-yyy1(2))+1;
        if x_size >= y_size
            if xxx(end) <= xxx1(2)
                x_start=xxx(end); x_end=xxx1(2);
                y_start=yyy(end); y_end=yyy1(2);
            else
                x_start=xxx1(2); x_end=xxx(end);
                y_start=yyy1(2); y_end=yyy(end);
            end
            x_coor=(x_start:1:x_end);
            y_coor=round(interp1([x_start x_end],[y_start y_end],x_coor));
            coor=[y_coor' x_coor'];
        else
            if yyy(end) <= yyy1(2)
                y_start=yyy(end); y_end=yyy1(2);
                x_start=xxx(end); x_end=xxx1(2);
            else
                y_start=yyy1(2); y_end=yyy(end);
                x_start=xxx1(2); x_end=xxx(end);
            end
            y_coor=(y_start:1:y_end);
            x_coor=round(interp1([y_start y_end],[x_start x_end],y_coor));
            coor=[y_coor' x_coor'];
        end
        for m=1:length(coor)
            location3(coor(m,1),coor(m,2))=1;
        end
    end
    location3=imdilate(location3,se);
    AA=zeros(size(A));
    AA(y_min:y_max, x_min:x_max)=location3;
    A_gb(AA==1)=1;
else
    location3=label==k;
```

```
            location3=imdilate(location3,se1);
            AA=zeros(size(A));
            AA(y_min:y_max, x_min:x_max)=location3;
            A_gb(AA==1)=1;
         end
      end
   end
   waitbar(i/max(max(A)));
end
close(h)
X=A_gb;
end
```

gb_tilt.m

```
function [X XX]=gb_tilt(A,B,C)

% A : grain_map
% B : GB_orientation map
% C : orientation matrix
% X : tilt_map
% XX : tilt_symmetry_map

grain_near_number{max(max(A))}=[];
for i=1:max(max(A))
   [y_coor x_coor]=find(A==i);
   y_max=min(max(y_coor)+10,size(A,1)); y_min=max(min(y_coor)-10,1);
   x_max=min(max(x_coor)+10,size(A,2)); x_min=max(min(x_coor)-10,1);
   location1=A(y_min:y_max, x_min:x_max);
   near= bwdist_old(location1==i)<=sqrt(2) & bwdist_old(location1==i)>0;
   grain_near_number{i}=unique(location1(near));
   grain_near_number{i}(grain_near_number{i}==0)=[];
end
for i=1:max(max(A))
   if size(grain_near_number{i},2)==0
      continue
   else
      for j=1:size(grain_near_number{i},1)
         grain_num=grain_near_number{i}(j);
         grain_near_number{grain_num}(grain_near_number{grain_num}==i)=[];
      end
   end
end
clear('y_coor','x_coor','y_max','y_min','x_min','x_max','location1','near',...
   'grain_num')

A_tilt=zeros(size(A)); A_symm=zeros(size(A));
h=waitbar(0,'Please be patient...');
for i=1:max(max(A))
   if size(grain_near_number{i},2)==0
      continue
   end
   size_1=size(find(A==i),1);
```

```
for j=1:size(grain_near_number{i},1)
   size_2=size(find(A==grain_near_number{i}(j)),1);
   if size_1 <= size_2
      [y_coor x_coor]=find(A==i);
      y_max=min(max(y_coor)+100,size(A,1)); y_min=max(min(y_coor)-100,1);
      x_max=min(max(x_coor)+100,size(A,2)); x_min=max(min(x_coor)-100,1);
      location1=A(y_min:y_max, x_min:x_max);
      location2=B(y_min:y_max, x_min:x_max);
      location5=C(y_min:y_max, x_min:x_max);
   else
      [y_coor x_coor]=find(A==grain_near_number{i}(j));
      y_max=min(max(y_coor)+100,size(A,1)); y_min=max(min(y_coor)-100,1);
      x_max=min(max(x_coor)+100,size(A,2)); x_min=max(min(x_coor)-100,1);
      location1=A(y_min:y_max, x_min:x_max);
      location2=B(y_min:y_max, x_min:x_max);
      location5=C(y_min:y_max, x_min:x_max);
   end
   location2(location2==0)=0.1;
   B_tilt=zeros(size(location2)); B_symm=zeros(size(location2));
   % finding original GBs
   location3=zeros(size(location1));
   location3(location1==i)=1; location3(location1==grain_near_number{i}(j))=2;
   near= bwdist_old(location3==2)<=sqrt(2) & bwdist_old(location3==2)>0;
   location3(near)=location3(near)+2;
   location3=bwmorph(location3==3,'skel',inf);
   conn=bwconncomp(location3); label=labelmatrix(conn);
   for k=1:max(max(label))
      location4=label==k & ~isnan(location2);
      [yy xx]=find(bwmorph(location4,'endpoints')==1);
      if isempty(yy) || size(yy,1)==1
         continue
      end
      zzz=bwtraceboundary(location4, [yy(1) xx(1)], 'W',8);
      coor=find(zzz(:,1)==yy(2) & zzz(:,2)==xx(2));
      zzz(coor+1:end,:)=[]; y=zzz(:,1); x=zzz(:,2);
      gb_orien=zeros(length(y),1);
      for m=1:length(y)
         gb_orien(m)=location2(y(m),x(m));
      end
      gb_orien1=zeros(size(gb_orien));
      gb_orien1(2:end,1)=diff(gb_orien);
      [z]=find(abs(gb_orien1) >= 60);
      zz=ones(length(z)+2,1); zz(end)=length(y); zz(2:end-1)=z;
      remove=[];
      for m=2:length(zz)-1
         if abs(zz(m)-zz(m-1)) <= 15 || abs(zz(m)-zz(m+1)) <= 15
            remove=cat(1,remove,m);
         end
      end
      zz(remove)=[]; zz(zz==1)=[]; zz(zz==length(y))=[];
      z=zz; clear('zz')
      if isempty(z)
         gb_orien2=median(gb_orien);
         near1= bwdist_old(location4==1)<=100 & bwdist_old(location4==1)>0;
         orien_1=median(location5(location1==i & near1==1));
         orien_2=median(location5(location1==grain_near_number{i}(j) & near1==1));
```

```
        if (gb_orien2-orien_1)*(gb_orien2-orien_2) >= 0
            tilt=abs(orien_1-orien_2);
        elseif (gb_orien2-orien_1)*(gb_orien2-orien_2) < 0
            tilt=180-abs(orien_1-orien_2);
        end
        if abs(gb_orien2-orien_1) < 10 && abs(gb_orien2-orien_2) > 80 &&...
                abs(gb_orien2-orien_2) <100
            symmetry=2;
        elseif abs(gb_orien2-orien_2) < 10 && abs(gb_orien2-orien_1) > 80 &&...
                abs(gb_orien2-orien_1) <100
            symmetry=2;
        else
            symmetry=1;
        end
        for p=1:length(y)
            B_tilt(y(p),x(p))=tilt;
            B_symm(y(p),x(p))=symmetry;
        end
    else
        for m=1:length(z)+1
            if m==1
                range=(1:z(m));
            elseif m==length(z)+1
                range=(z(m-1)+1:length(y));
            else
                range=(z(m-1)+1:z(m));
            end
            location6=zeros(size(location4));
            for p=1:length(range)
                location6(y(range(p)),x(range(p)))=1;
            end
            near1= bwdist_old(location6==1)<=100 & bwdist_old(location6==1)>0;
            orien_1=median(location5(location1==i & near1==1));
            orien_2=median(location5(location1==grain_near_number{i}(j) & near1==1));
            gb_orien2=median(gb_orien(range));
            if (gb_orien2-orien_1)*(gb_orien2-orien_2) >= 0
                tilt=abs(orien_1-orien_2);
            elseif (gb_orien2-orien_1)*(gb_orien2-orien_2) < 0
                tilt=180-abs(orien_1-orien_2);
            end
            if abs(gb_orien2-orien_1) < 10 && abs(gb_orien2-orien_2) > 80 &&...
                    abs(gb_orien2-orien_2) <100
                symmetry=2;
            elseif abs(gb_orien2-orien_2) < 10 && abs(gb_orien2-orien_1) > 80 &&...
                    abs(gb_orien2-orien_1) <100
                symmetry=2;
            else
                symmetry=1;
            end
            for p=1:length(range)
                B_tilt(y(range(p)),x(range(p)))=tilt;
                B_symm(y(range(p)),x(range(p)))=symmetry;
            end
        end
    end
end
```

```
        BB=zeros(size(A));
        BB(y_min:y_max, x_min:x_max)=B_tilt;
        A_tilt(BB~=0)=BB(BB~=0);
        CC=zeros(size(A));
        CC(y_min:y_max, x_min:x_max)=B_symm;
        A_symm(CC~=0)=CC(CC~=0);
    end
    waitbar(i/max(max(A)));
end

close(h);

X=A_tilt;

XX=A_symm;

end
```

aspect_ratio.m

```
function [X Y]=aspect_ratio(XX)


Anisotropic=zeros(max(max(XX)),1);

for i=1:max(max(XX))
    [y_coor x_coor]=find(XX==i);
    y_max=min(max(y_coor)+11,size(XX,1)); y_min=max(min(y_coor)-11,1);
    x_max=min(max(x_coor)+11,size(XX,2)); x_min=max(min(x_coor)-11,1);
    B=XX(y_min:y_max, x_min:x_max);
    BB=B==i;
    A=regionprops(BB,'MajorAxisLength');
    A=A.MajorAxisLength;
    AA=regionprops(BB,'MinorAxisLength');
    AA=AA.MinorAxisLength;
    Anisotropic(i)=A/AA;
end

Anisotropic_avg=median(Anisotropic);

X=Anisotropic;
Y=Anisotropic_avg;

end
```

triple.m

```
function [X Y]=triple(A,B)
% A = grain_map
% B = Grain boundary tilt matrix
gb_dilated=zeros(size(A));
se=strel('disk',1);
```

```
for i=1:max(max(A))
   AA=A==i;
   AA=imdilate(AA,se);
   gb_dilated=gb_dilated+AA;
end
clear('se','AA')

conn=bwconncomp(gb_dilated==3); label=labelmatrix(conn);
triple_dist=zeros(max(max(label)),6);
h=waitbar(0,'Please be patient...');
for i=1:max(max(label))
   [y_coor x_coor]=find(label==i);
   y_coor=round(mean(y_coor)); x_coor=round(mean(x_coor));
   y_max=min(max(y_coor)+11,size(A,1)); y_min=max(min(y_coor)-11,1);
   x_max=min(max(x_coor)+11,size(A,2)); x_min=max(min(x_coor)-11,1);
   BB=B(y_min:y_max, x_min:x_max);
   BBB=unique(BB(10:14,10:14)); BBB(BBB==0)=[];
   if size(find(BBB < 15),1) >= 1
      continue
   end
   max_lab=double(0); B2=zeros(size(BB));
   center=zeros(size(B2)); center(10:14,10:14)=1;
   near=bwdist_old(center) <= sqrt(2) & bwdist_old(center)>0;
   if length(BBB)==3
      for j=1:length(BBB)
         B1=BB==BBB(j); B1=bwareaopen(B1,2); B5=double(B1);
         B5(B5==1 & center==1)=3; [y x]=find(B5==3);
         B1=bwselect(B1==1,x,y);
         conn=bwconncomp(B1);
         label1=labelmatrix(conn); lab=double(label1);
         lab(lab~=0)=lab(lab~=0)+max_lab;
         B2=B2+lab; max_lab=max_lab+double(max(max(label1)));
      end
   else
      for j=1:length(BBB)
         B1=BB==BBB(j); B1(center==1)=0; B1=bwareaopen(B1,2);
         conn=bwconncomp(B1);
         label1=labelmatrix(conn); lab=double(label1);
         lab(lab~=0)=lab(lab~=0)+max_lab;
         B2=B2+lab; max_lab=max_lab+double(max(max(label1)));
      end
   end
   if max(max(B2))~=3
      continue
   end
   vectors=zeros(3,2);
   for j=1:3
      B4=B2==j; B4=bwmorph(B4,'endpoints');
      B4(center==1)=0;
      [yy xx]=find(B4==1);
      if isempty(yy)
         B4=B2==j; B4=bwmorph(B4,'endpoints');
         [yy xx]=find(B4==1);
      end
      yy=round(mean(yy))-12; xx=round(mean(xx))-12;
      degree=real(rad2deg(atan(yy/xx)));
```

```
        %
        B5=B2==j; B5=double(B5);
        B5(B5==1 & near==1)=3;
        if size(find(B5==3),1)==1
            [y x]=find(B5==3); x=x-12; y=y-12;
        elseif size(find(B5==3),1) > 1
            [y x]=find(B5==3);
            sort_1=zeros(length(y),3);
            for m=1:length(y)
                sort_1(m,1)=sqrt((x(m)-12)^2+(y(m)-12)^2);
                sort_1(m,2)=x(m); sort_1(m,3)=y(m);
            end
            sort_1=sortrows(sort_1);
            x=sort_1(1,2); y=sort_1(1,3);
            x=x-12; y=y-12;
        elseif size(find(B5==3),1)==0
            [y x]=find(B5==1);
            sort_1=zeros(length(y),3);
            for m=1:length(y)
                sort_1(m,1)=sqrt((x(m)-12)^2+(y(m)-12)^2);
                sort_1(m,2)=x(m); sort_1(m,3)=y(m);
            end
            sort_1=sortrows(sort_1,-1);
            x=sort_1(1,2); y=sort_1(1,3);
            x=x-12; y=y-12;
        end
        if y > 0 && x < 0
            degree=180-abs(degree);
        elseif y < 0 && x < 0
            degree=180+abs(degree);
        elseif y < 0 && x > 0
            degree=360-abs(degree);
        elseif x==0 && y > 0
            degree=90;
        elseif x==0 && y < 0
            degree=270;
        elseif y==0 && x < 0
            degree=180;
        elseif y==0 && x > 0
            degree=0;
        end
        vectors(j,1)=cos(deg2rad(degree));
        vectors(j,2)=sin(deg2rad(degree));
    end
    for j=1:3
        vector=vectors; vector(j,:)=[];
        vector1=[vector(1,1) vector(1,2)];
        vector2=[vector(2,1) vector(2,2)];
        triple_dist(i,j)=real(rad2deg(acos(dot(vector1,vector2)/norm(vector1) / norm(vector2))));
        triple_dist(i,j+3)=mode(BB(B2==j));
    end
    waitbar(i/max(max(label)));
end
close(h);
remove=[];
for i=1:length(triple_dist)
```

```
   if unique(triple_dist(i,:))==0
     remove=cat(1,remove,i);
   end
end
triple_dist(remove,:)=[];

dihedral_tilt=zeros(length(triple_dist)*3,2);
for i=1:length(triple_dist)
   dihedral_tilt((i-1)*3+1,1)=triple_dist(i,1);
   dihedral_tilt((i-1)*3+1,2)=triple_dist(i,4);
   dihedral_tilt((i-1)*3+2,1)=triple_dist(i,2);
   dihedral_tilt((i-1)*3+2,2)=triple_dist(i,5);
   dihedral_tilt((i-1)*3+3,1)=triple_dist(i,3);
   dihedral_tilt((i-1)*3+3,2)=triple_dist(i,6);
end
remove=[];
for i=1:length(dihedral_tilt)
   if dihedral_tilt(i,2) < 15
   remove=cat(1,remove,i);
   end
end

dihedral_tilt(remove,:)=[];

X=triple_dist;
Y=dihedral_tilt;
end
```

gbenergy.m

```
function X=gbenergy(A,B)

angle=A(:,2);

min_angle=min(angle);
max_angle=max(angle);

num=ceil((max_angle-min_angle)/B);

BB=zeros(length(A),2);
BB(:,1)=A(:,2); BB(:,2)=A(:,1);
BB=sortrows(BB);

bin=[15:B:15+num*B];

AAA=zeros(length(bin)-1,3);
remove=[];
for i=1:length(bin)-1
   BBB=BB;
   coor= BBB(:,1) < bin(i) | BBB(:,1) >= bin(i+1);
   BBB(coor,:)=[];
   if size(BBB,1) <= 5
```

```
        remove=cat(1,remove,i);
    end
    AAA(i,1)=mean(BBB(:,1));
    AAA(i,2)=mean(BBB(:,2));
end
AAA(remove,:)=[];

N=length(AAA);
A1=zeros(N*(N-1)/2,N);

L=0;
for j=1:N
    for i=1:N-j
        A1(i+L,j)=sin(deg2rad(AAA(i+j,2)));
        A1(i+L,i+j)=-sin(deg2rad(AAA(j,2)));
    end
    L=L+i;
end

A2=null(A1,'r');

for i=1:N
    AAA(i,3)=A2(i);
end

X=AAA;
end
```